ABSTRACT

Title of Document: MECHANICAL, STRUCTURAL AND BIOLOGICAL PROPERTIES OF BIOPOLYMER-BASED HYDROGELS

Laura Lynn Hyland, Ph.D., 2012

Directed By: Professor Y. Bruce Yu, Department of Bioengineering

The aim of this dissertation was to begin to understand how biopolymer interactions affect mechanical and structural properties of biomaterials, and how those properties affect stem cell behavior. Polysaccharide, oligopeptide and oligopeptide-polysaccharide composite materials were made and then characterized using a range of techniques. It was found that chondroitin addition to chitosan-alginate networks improved both tensile and compressive strength. Increasing polysaccharide concentration also improved mechanical properties. Also, polysaccharide incorporation into peptide hydrogels increased biomaterial resistance to strain break. Structural analysis supported mechanical data, showing that incorporation of the peptides dramatically changed the morphology of the polysaccharide networks. Biopolymer chirality was also explored in this work. By incorporating polysaccharides and oligosaccharides into both *L*- and *D*-forms of peptide hydrogels, we observed differences in mechanical properties not seen in *L*- and *D*-oligopeptide

hydrogels alone. Greater interactions between *L*-oligopeptides and *D*-saccharides lead to stronger materials with distinctively different structural characteristics from hydrogels made from *D*-oligopeptides and *D*-saccharides. This phenomenon, known as chiral selectivity, has previously only been seen at the molecular level. Here, we showed that chiral selectivity is another unique property of biopolymers that can be exploited to tune mechanical and structural properties of materials. Chiral selectivity was also observed in terms of stem cell behavior in this work. However another property, hydrogel charge, was used to diminish the effects of chiral selectivity in order to enhance the biocompatibility of *D*-oligopeptide hydrogels. It was found that negative charges significantly improved human mesenchymal stem cell attachment and proliferation in *D*-oligopeptide gels but had little effect on their interactions with *L*-oligopeptide gels. These results suggest that it is possible to use charge and other properties of biopolymers to engineer biomaterials whose chirality is distinct from that of natural biomaterials but whose performance is close to that of natural biomaterials. These oligopeptide-based biomaterials also offer new tools to investigate biohomochirality, an important and unresolved question in biology.

MECHANICAL, STRUCTURAL AND BIOLOGICAL PROPERTIES OF BIOPOLYMER-BASED HYDROGELS

By

Laura Lynn Hyland

Dissertation submitted to the Faculty of the Graduate School of the
University of Maryland, College Park, in partial fulfillment
of the requirements for the degree of
Doctor of Philosophy
2012

Advisory Committee:
Professor Y. Bruce Yu, Chair
Professor Boualem Hammouda
Professor Gregory Payne
Professor Srinivasa Raghavan
Professor Joonil Seog

Acknowledgements

First I would like to express my gratitude to my advisor Dr. Yihua Bruce Yu for his guidance, advice, patience and encouragement during my time at the University of Maryland. His attention to detail has made me a better and more scrupulous scientist. I am also grateful to my committee members for their helpful discussions and advice.

A lot of thanks go to my friends for their company, positive words and advice. Thanks especially to Jules for collaborating with me and teaching me how to work with her cells. I am grateful to the lunch crew for the sometimes long-running lunches which could always turn a bad day into a good one. Thanks to Robyn, for her encouragement and for allowing me to run pilot cell experiments in her lab. Special thanks to Marc for his guidance and zest for research. He has inspired me to become a more open-minded researcher. Thanks to Kat for making my Ph.D. experience more fun and for her always excellent advice. Also, thanks to Yue for his help with many of my experiments, from NMR training to loaning peptides.

It is impossible to find words to express my appreciation for my husband, Zachary for his extraordinary understanding and patience with me. His positive outlook on every situation has helped me gain perspective. I would also like to express my heartfelt thanks to my family in Missouri, Ohio and Wisconsin for their continuous and unfailing support of all my endeavors.

Table of Contents

List of Tables

List of Tables

List of Figures

List of Abbreviations

ANOVA……..Analysis of variance
B…….. Mass fractal prefactor
BMP…….Bone morphogenic protein
C_i…….. concentration of scattering component
Ca^{2+}…….Calcium
$CaCl_2$……...Calcium chloride
D……...pore diameter
d……mass fractal dimension
d_{max} .....Maximum Linear Dimension of the Particle
DAPI……4',6-diamidino-2-phenylindole
DMEM……Dulbecco's Modified Eagle Medium
ECM .....Extra Cellular Matrix
ESI-MS……...Electrospray Ionization Mass Spectrometry
FGF-2…….Fibroblast Growth Factor-2
Fmoc……...Fluorenyl Methoxy Carbonyl
G' ..... Elastic Modulus or Storage Modulus
G" ..... Loss Modulus or Viscous Modulus
GAGs……Glycosaminoglycans
HBTU……O-Benzotriazole-tetramethyl-uronium-hexafluoro-phosphate
HCl……..Hydrochloric Acid
hMSC……...Human Mesenchymal Stem Cell
HOBt……Hydroxybenzotriazole
HPC……..Hydroxypropyl Cellulose
HPLC ..... High Perfomlance Liquid Chromatography
I(Q) ..... Intensity of the Scatterer
L_c……..Correlation length
L_p.....Persistence length
M_i……..Average molecular weight of scattering component
NH_4HCO_3……Ammonium Bicarbonate
NH_4OH……Ammonium Hydroxide
NMR ..... Nuclear Magnetic Resonance
Pcr ..... Pair-wise Scattering Vector Length Distribution Function
Q ..... Magnitude of Scattering Vector
Rc ..... Radius of Gyration of Cross-section
SAS……. Small Angle Scattering
SANS…….. Small Angle Neutron Scattering
SAXS ..... Small Angle X-ray Scattering
SEM……. Scanning electron microscopy or standard error of the mean
TCPS……Tissue Culture Polystyrene
TSP……...Trimethylsilyl propanoic acid
USANS…… Ultra Small Angle Neutron Scattering
WAS……Wide Angle Scattering
WST-1……. Formazan-based proliferation assay
w/w…….. Mass fraction

Chapter 1: Introduction

1.1 Biopolymers in Biomaterials Research

The new emphasis in the field of tissue engineering has been on the design and engineering of degradable materials that aid in the regeneration of tissues (*1*). One of the most prevalent approaches involves employing biopolymer-based biomaterials as a support system for the delivery of cells and/or growth factors to damaged tissues (*2,3*). This undertaking requires that the biomaterial provides sufficient mechanical support during tissue rebuilding.

In addition to providing mechanical support, it is important for the biomaterial to support and sustain an environment that enables appropriate cellular growth, adhesion and differentiation. An appropriate cell environment is the key to eliciting new tissue development (*4*). As supports for cell growth, synthetic biodegradable polymers have been widely used (*5*). However, in order to stimulate or modulate new tissue development, synthetic materials must be supplemented with bioactive molecules like BMP (bone morphogenetic protein) and FGF-2 (fibroblast growth factor 2) to name a few (*6*). In contrast, naturally derived polymers have a built-in ability to stimulate tissue growth. Several of these biopolymers (e.g. chondroitin sulfate, heparan sulfate, collagen, etc.) are components of or mimic the extracellular matrix (ECM), thus they ordinarily interact with cells. For example, since the ECM is important in regulating elements of cell adhesion, division and differentiation, biopolymers are a good starting point for trying to reproduce native properties of tissues.

Compared with synthetic polymers, biopolymers offer much more diverse chemistries. For example, in protein and peptide engineering there are 20 different natural amino acids and other unnatural amino acids to choose from. Precise chain-length control of biopolymers is another advantage over synthetic polymers.

In this dissertation work, combinations of different types of biopolymers were investigated in order to create materials with the desired structural and mechanical properties in an effort to mimic natural vertebrate extracellular matrix. The types investigated include natural polysaccharides and engineered oligopeptides. Interest in polysaccharides as biomaterials stems from their structural and biochemical similarities to glycosaminoglycans (GAGs). GAGs are long, unbranched polysaccharides and are an important component of the connective tissue. They attract water molecules, which is what provides tissue resistance to pressure. Peptides are another family of biopolymers that have attracted interest as tissue scaffold materials. Peptides have the ability to self-assemble into interwoven fibers which confer mechanical rigidity to materials. Described here in more detail are the biopolymers utilized in this work.

1.1.1 Polysaccharides

Alginate is one of the most commonly used biopolymers. It is used in a variety of medical applications including cell encapsulation and delivery because it is commercially available, gels under mild conditions and has relatively low cytotoxicity. Alginates are naturally derived polysaccharide block copolymers composed of regions of β-*D*-mannuronic acid monomers (M-blocks), regions of α-*L*-guluronic acid (G-blocks) (*7*). The percentage and distribution of each M or G

monomer depends on the species of seaweed used for alginate isolation (*8*). Alginate gels are formed when divalent cations such as calcium and magnesium interact with negatively charged G-blocks to form ionic bridges between different polymer chains. As a result, the mechanical properties and pore size of alginate gels can be easily controlled by varying the M to G ratio, the molecular weight of the alginate and the type of divalent cation selected for cross-linking (*9*). The molecular weight of alginate used in this work ranges from 350 to 450 kDa.

Cellulose is an inexpensive, readily available biopolymer in part because it is the most abundant organic polymer in the world (*10*). Cellulose can be easily modified with acetate, methyl or hydroxypropyl groups to name a few, which makes it desirable as a biomaterial (*11*). It is a linear polysaccharide composed of *D*-glucose units linked by glycosidic bonds where every other glucose residue is rotated about 180° (*12,13*). One such modified cellulose, hydroxypropylcellulose (HPC), is a neutral and water-soluble cellulose ether with a unique combination of properties including thermoplasticity, water solubility and surface activity (*14*). The advantages of cellulose ethers are that they are biocompatible and hence can be used for many pharmaceutical purposes (*15*). The molecular weight of HPC is ~80 kDa.

Chitosan has been investigated for many different tissue engineering applications because it is structurally similar to GAGs found in the extracellular matrix. Chitosan can also be degraded by enzymes, giving it desirable biodegradable properties (*16*). It is a linear polysaccharide made of *D*-glucosamine and N-acetyl-*D*-glucosamine derived from chitin. Chitin is a natural polysaccharide found particularly in the exoskeleton of crustaceans and insects (*17*). The degree of N-deacetylation

usually varies from 75% to 90% and the molecular weight ranges from 100 to 1000 kDa (*8*). Positively charged chitosan is soluble in dilute acids which protonate the free amino groups.

Chondroitin sulfate is one of the most abundant GAGs, found in cartilage, synovial fluid, bone, and heart valves (*18*). Chondroitin sulfate is a component of proteoglycans, covalently linked to a protein core (*19*). It is made of repeating disaccharide units of *D*-glucuronic acid and N-acetyl galatosamine, which are sulfated at either 4- or 6-positions (*20*). Chondroitin sulfate is a negatively charged polysaccharide, with a molecular weight of ~20 kDa. The benefit of using GAGs as biomaterials is having a material that can bind to and modulate growth factors and cytokines and is also involved in cell adhesion, proliferation and differentiation (*21*). Moreover, GAGs degrade to non-toxic oligosaccharides. These characteristics together with their defined physical and chemical characteristics make them very interesting biopolymers.

Also known as animal starch, glycogen is a neutral biopolymer made exclusively of *D*-glucose units. As a biodegradable material, glycogen is excellent since it degrades to simple glucose monomers. Glycogen is a polymer of α(1→4) glycosidic bonds, linked with α(1→6)-linked branches (*22*). Glycogen is a neutral polysaccharide with a molecular weight ranging from 400 kDa to millions of kDa, depending on the amount of branching and polymerization (*23*). In the body, glycogen is polymerized by the protein glycogenin.

1.1.2 Oligopeptides

Oligopeptide biopolymers are attracting interest as biomaterials due to their biodegradable, programmable and bioresorbable nature. Unlike synthetic polymers, oligopeptides can be made with precise control over sequence, chain length and stereochemistry. Oligopeptide-based networks with viscoelastic properties have been designed for various biomedical applications (*24*). Oligopeptide hydrogels have often been used to promote growth and proliferation of a variety of cell types, including chondrocytes, hepatocytes, endothelial cells, osteoblasts, neuronal cells and stem cells (*25*). Additionally, oligopeptides can be designed with sequences that promote cell activities such as attachment and proliferation. Commercially available *L*-protein (e.g., MatriGel^{TM}) and *L*-oligopeptide (e.g., PuraMatrix^{TM}) hydrogels have been used to mimic the ECM for cell culture applications.

1.1.3 Oligopeptide-Polysaccharide Composite Materials

Since the ECM contains both proteins and polysaccharides, groups have developed composite materials from peptides and polysaccharides in an effort to make better ECM mimetics. For Yamada et al., addition of a laminin active peptide into agarose gels resulted in a matrix that could support both the 2D and 3D culture of a variety of cells (*26*). This group also observed improvements in cell behavior when peptides were incorporated in chitosan and alginate gels (*27*). Conjugation of heparin, a linear glycosaminoglycan, to peptides such as collagen, gelatin and fibrin has been highly attractive since these conjugations sequester growth factors and prevent their bulk release (*28-32*). In chapter 3, composite oligopeptide-polysaccharide hydrogels

were created with interesting mechanical properties. Future cell studies may show whether these composite materials can improve cell behavior and growth as well.

1.2 Mechanical Testing in Biomaterials Research

1.2.1 Compression-Tensile Testing

The measurement of the mechanical behavior of a sample under compression and tension can be performed to provide basic biomaterial mechanical data that is critical for material design and performance assessment. The requirements for compression and tensile strength values and the methods for testing these properties are specified in various standards (i.e., ASTM) for a wide variety of biomaterials.

The compression test is a method for determining the behavior of biomaterials under a compressive load. Compression tests are performed by loading the sample between two plates, and then applying a force to the sample by moving the plates together. During the test, the sample is compressed and deformation versus the applied load is recorded. The compression test is used to determine yield point, yield strength, and compressive strength.

The tensile test is a method for determining behavior of biomaterials under tensile loading. The tests are conducted by fixing the sample into the test instrument and then applying a force to the sample by separating the testing machine crossheads. The crosshead speed can be varied to control the rate of strain in the test sample. Data from the tests are used to determine yield strength and elastic modulus. Measurement of the sample dimensions after testing also provides elongation values to characterize material ductility.

1.2.2 Oscillatory Rheometry

An oscillatory rheometer is a device that can be used to measure the viscoelastic properties of soft biomaterials. The basic principle of an oscillatory rheometer is to make cyclic shear deformations in the sample and then measure the resulting stress responses. The tests are conducted by placing the sample between two plates. While the bottom plate remains stationary, a motor rotates the top plate, which imposes a time dependent strain on the sample. Simultaneously, the time dependent stress is quantified by measuring the force that the sample imposes on the top plate. Common measurements include time-sweep, which measures time-dependent linear viscoelastic moduli, G'(ω) (elastic modulus) and G"(ω) (viscous modulus), frequency-sweep, which shows material dependence on angular frequency and strain-sweep, which measures biomaterial strain yield values (γ_{yield}).

1.2.3 Compression-Tensile testing vs. Oscillatory Rheometry

Both compression-tensile testers and rheometers are excellent choices for biomaterial mechanical testing. Rheometers are a better choice for testing very soft materials since these materials can be difficult to work with in a compression-tensile tester. Rheometry also allows one to monitor material stiffness changes over time, which could not be as easily done using a compression-tensile tester. However, when working with stronger materials, compression-tensile testers provide a wider range of mechanical tests. Because rheometers measure shear moduli and compression-tensile testers measure Young's moduli, these two instruments can also complement each other, giving a better overall picture of biomaterial properties.

1.3 Small-Angle Scattering in Biomaterials Research

Small-angle scattering (SAS, angle ~0-2˚) has become a powerful tool for elucidating the structure of biomaterials. SAS is a scattering method based on the small deflection of collimated radiation away from the straight path after it interacts with structures that are larger than the wavelength of the radiation (*33*). The "angle" in SAS refers to the angle of radiation deflection. SAS techniques can give information about the shape and size of structures in a sample. SAS is used more often in biomaterials research than techniques like wide-angle scattering (WAS, angle ~2-90˚) because WAS tells about the amount of crystallinity within a sample. Often, biomaterials are fairly amorphous so this technique is not very informative. Small-angle X-ray scattering (SAXS) and small-angle neutron scattering (SANS) are two SAS techniques, each with their own advantages and disadvantages. Both techniques have been used extensively to characterize biomaterials and are described in more detail below.

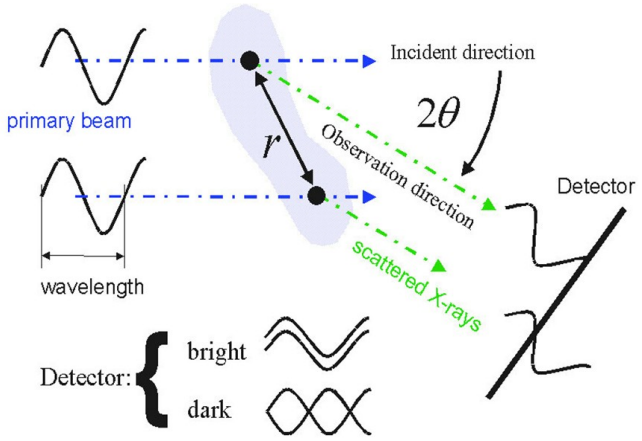

Figure 1.1: Small-angle scattering pictorial representation of how x-rays are scattered and detected in the presence of a sample. This image is taken from H. Schnablegger and Y. Singh's "A practical guide to SAXS", published by Anton Paar.

1.3.1 Small-Angle X-ray Scattering (SAXS)

SAXS is a widely used technique in the biomaterials community. It is especially used to determine basic structural characteristics such as material correlation length and fiber mass fractal dimension. Gamani et al. used SAXS to characterize crosslinked hylaronan. Using an *I(q)* vs. *q* plot, they determined the polymer junction zone for each gel type (*34*). SAXS was also used to study how the chemical compositions and concentrations of calcium-alginate gels affected their structures. It was found that lateral association of chain segments, which dictates junction zone lengths, depends on a number of material factors elucidated by SAXS (*35*). Shinohara et al. used SAXS to investigate the structure of slide-ring gels in various solvent types. They were able to see a "pulley effect", a unique property of their gels, by simply examining the shape of the raw scattering data (*36*). Tada et al. used SAXS to study the change in structure of curdlan gels over time (*37*). SAXS was also used to examine changes to hydroxyapatite size in bone after extreme heating (*38*).

1.3.2 Small-Angle Neutron Scattering (SANS)

SANS is another scattering technique used in biomaterials characterization. Since there is a large difference between neutron scattering lengths of hydrogen and deuterium, contrast variation is often used in SANS studies for selective labeling.

Markarian et al. used SANS contrast matching to study single chain dimensions of novel materials made from sulfonated poly(styrenesulfonate) and poly(diallyldimethylammonium chloride) at different ionic strengths (*39*). Others use SANS to examine molecular distribution and conformation. Wilson et al. used both

SANS and ultra small-angle neutron scattering (USANS) to measure silica nanoparticle dispersion in dental nanocomposites (*40*). Luk et al. characterized the distribution of water in semicrystalline and amorphous polymers (*41*). Feuz et al. determined the conformations of poly(L-lysine)-graft-poly(ethylene glycol) molecular brushes (*42*). Still others used SANS in conjunction with rheometry to measure the structural response of fibrin gel to shear deformation (*43*).

1.3.3 SAXS vs. SANS

The setup of the SAXS instrument we used at Argonne National Lab allowed us to take measurements of samples very quickly (0.2 s), which made time-dependent structural studies possible. These studies were not possible with SANS. Smaller sample size and sample preparation in H_2O are other practical advantages of SAXS. SANS samples must be prepared in D_2O. In addition to SAXS, we also used SANS to elucidate structural features of our hydrogels. The advantage of the SANS instrument we used at the National Institute of Standards and Technology (NIST) compared with the SAXS instrument was its much larger maximum resolution. The maximum resolved size for the SAXS instrument was ~500 Å, while the maximum resolved size for SANS was ~2000 Å, which allowed us to explore structural features at a larger scale.

1.4 Manipulating Chirality in Biomaterials Research

The term chirality is used to describe the structural property of an object that is non-superimposable on its mirror image. Interestingly, biomacromolecules are homochiral, where proteins contain exclusively *L*-amino acids and most

polysaccharides and nucleic acids contain exclusively *D*-sugars. As a result, biochemical interactions within the body are chirality-dependent (*44*).

Some researchers have taken advantage of these chirality-dependent interactions by creating oligopeptide-based hydrogels that contain *D*-amino acids. Luo et al. found that oligopeptides made of *D*-amino acids could tolerate high temperatures (*45*) and were resistant to protease digestion (*46*). Nagy et al. found that heterochiral hydrogels containing some *D*-oligopeptides have higher elastic moduli than the parent homochiral hydrogels (*47*). Dzwolak et al. found that poly(*D*-lysine) + poly(*L*-lysine) form amyloid-like fibrils while each individual enantiomer remains a clear solution (*48*). We found that homochiral (*D* or *L*) hydrogels confer a mechanical advantage while heterochiral hydrogels confer a kinetic advantage (*49*).

In this dissertation work, biomaterial chirality was exploited in two different ways. First, molecular chiral selectivity was used to create novel oligopeptide-polysaccharide hybrid materials with different mechanical properties. Because polysaccharides are made of *D*-sugars, which are known to have a stronger affinity for *L*-amino acids compared with *D*-amino acids, we hypothesized that materials made of *D*-sugars and *L*-amino acids would have different properties than materials made of *D*-sugars and *D*-amino acids. Indeed, hybrid materials composed of *D*-polysaccharides and *L*-oligopeptides were found to be mechanically stronger than materials composed of *D*-polysaccharides and *D*-oligopeptides. This phenomenon helps to explain, from a mechanical viewpoint, why sugars and amino acids in biomacromolecules have opposite chiralities in nature.

Second, material chirality was manipulated in conjunction with material charge to create new hydrogels that could support mesenchymal stem cell attachment and growth. It has been suggested that oligopeptides made of *D*-amino acids are more resistant to enzyme degradation and therefore could theoretically prolong hydrogel residence time in the body (*46*). The problem with this approach is that cells also have more difficulty recognizing, attaching to and proliferating on *D*-synthetic polymeric materials compared with *L*-synthetic polymeric materials (*50,51*). Since many cellular activities are also governed by charge, we hypothesized that charge could improve cell recognition and behavior on *D*-oligopeptide-based hydrogels. In fact, negative charge does improve mesenchymal stem cell attachment and proliferation on *D*-oligopeptide-based hydrogels. This means that material chirality, in conjunction with charge, can be manipulated to create oligopeptide-based materials that are more enzyme resistant, yet still supportive of mesenchymal stem cell attachment and proliferation.

1.5 Dissertation Overview

This work is a combination of projects that helps to elucidate the mechanical and structural properties of novel biopolymer-based hydrogels and how some of these biopolymer properties affect mesenchymal stem cell behavior. In Chapter 2, we examined how interactions between charged polysaccharides create networks with different mechanical and structural properties. In Chapter 3, we studied how interactions between charged oligopeptides and charged polysaccharides create hydrogels with different mechanical and structural properties. In Chapter 4, we observed how oligopeptide chirality affected interactions with polysaccharides by

measuring the mechanical and structural properties of the resulting oligopeptide-polysaccharide hydrogels. In Chapter 5, we looked at how human mesenchymal stem cell behavior was affected by oligopeptide hydrogel chirality and charge.

Chapter 2: Mutually Reinforced Multi-Component Polysaccharide Networks

2.1 Abstract

Networks made from chitosan and alginate have been utilized as prospective tissue engineering scaffolds due to material biocompatibility and degradability. Calcium (Ca^{2+}) is often added to these networks as a modifier for mechanical strength enhancement. In this work, we examined changes in the bulk material properties of different concentrations of chitosan/alginate mixtures (2, 3, or 5% w/w) upon adding another modifier, chondroitin. We further examined how material properties depend on the order the modifiers, Ca^{2+} and chondroitin, were added. It was found that the addition of chondroitin significantly increased the mechanical strength of chitosan/alginate networks. Highest elastic moduli were obtained from samples made with mass fractions of 5% chitosan and alginate, modified by chondroitin first and then Ca^{2+}. The elastic moduli in dry and hydrated states were (4.41 6 0.52) MPa and (0.11 6 0.01) MPa, respectively (Figure 2.3, Appendix Table A1). Network porosity and density were slightly dependent on total polysaccharide concentration. Average pore size was slightly larger in samples modified by Ca^{2+} first and then chondroitin and in samples made with 3% starting mass fractions. Here, small-angle neutron scattering (SANS) was utilized to examine mesh size of the fibrous networks, mass-fractal parameters and average dimensions of the fiber crosssections prior to freeze-drying. These studies revealed that addition of Ca^{2+} and chondroitin modifiers

increased fiber compactness and thickness, respectively. Together these findings are consistent with improved network mechanical properties of the freeze-dried materials.

2.2 Introduction

Chitosan has become one of the most commonly utilized biopolymers in biomaterials research. This cationic polysaccharide has many attractive qualities and is abundantly found in nature (*52*). Chitosan has been widely studied for tissue engineering applications because of its biocompatibility and biodegradability. Its degradation products are glucosamine and N-acetyl glucosamine, amino sugars naturally found in the human body. The hydrophilic surface of chitosan has been shown to promote cell adhesion, proliferation, and differentiation (*53-55*). Chitosan is also versatile; it is easily moldable and has many functional groups that can be modified to tune material properties (*56*). However, by itself chitosan is mechanically weak and swells to disassembly in aqueous environments (*57*).

Alginate is an anionic polysaccharide that can electrostatically interact with cationic chitosan (*58*). Upon interaction, alginate and chitosan form fibers which create a gel-like, solid material. This material can be freeze-dried and mechanically tested. Like chitosan, alginate is a widely used biocompatible polymer, which is known to support the proliferation of cells both *in vitro* and *in vivo* (*59, 60*). However, on its own alginate is a viscous, weak material. When used as a component in scaffolds, alginate is often modified with divalent cations like Ca^{2+} to create a strong gel with a characteristic egg box structure (*61*).

A number of networks have been made using combinations of chitosan and alginate with Ca^{2+} as a modifier. These materials were made by combining and

freeze-drying the mixtures to create novel biomaterials. Uses for these networks include bone replacements (*62*), liver replacements (*63*) and medicated wound dressings (*64*). These studies have examined chitosan-alginate networks at low polysaccharide mass fractions (0.05% to 2.4%), but give valuable insight about network characteristics such as tunability and cell compatibility. The strongest chitosan-alginate networks to date were made with a mass fraction of 2.4% chitosan and a mass fraction of 2.4% alginate and had a dry compressive elastic modulus of (2.56 ± 0.41) MPa (*62*). These networks could support osteoblast attachment, proliferation and also calcium deposition. Here, the potential of the chitosan-alginate networks as load-bearing biomaterials was demonstrated. However, these data lacked the important mechanical characteristics in the biologically relevant hydrated state. Therefore, more studies are necessary.

In addition to alginate, chitosan can interact with glycosaminoglycans (GAGs) which are also anionic polysaccharides. GAGs are valuable because they can facilitate the migration and proliferation of progenitor cells promoting tissue regeneration (*65, 66*). Chondroitin sulfate is one kind of commercially available GAG. We found that this anionic polysaccharide creates fibrous, elastic networks with the cationic chitosan upon mixing. Chitosan-chondroitin networks have been used for the controlled release of platelet-derived growth factor for bone regeneration. *In vitro* drug release could be controlled by adjusting the ratio of chitosan to chondroitin (*67*).

To improve the mechanical properties of the scaffolds, we hypothesize that the incorporation of chondroitin as a second modifier into the chitosan-alginate-Ca^{2+}

network could increase electrostatic interactions and improve its overall strength and flexibility. Further, we examined the effect of the order of adding each of the two modifiers, Ca^{2+} and chondroitin, on the mechanical strength of the network. To this end, three types of networks were prepared: type **A**, which are chitosan/alginate networks with Ca^{2+} as the sole modifier; type **B**, which are chitosan/alginate networks with Ca^{2+} added as the 1st modifier and chondroitin added as the 2nd modifier; type **C**, which are chitosan/alginate networks with chondroitin added as the 1st modifier and Ca^{2+} added as the 2nd modifier. The resulting freeze-dried networks were tested for their compression and tensile strengths.

To promote cell proliferation and migration *in vivo*, networks should have high porosity, suitable and non-uniform pore size, and highly interconnected pore structure in addition to biocompatibility and biodegradability (*68-70*). Therefore, network porosity, density and pore size of the freeze-dried materials were examined to determine the effect of the polysaccharide content, the addition of a 2nd modifier, as well as the addition order of the two modifiers, on these properties.

It would be reasonable to suggest that mechanical strength of the freeze-dried polysaccharide scaffolds would depend on the structural characteristics of the polysaccharide networks formed in solution when mixing the components prior to freeze-drying. Therefore, to aid our understanding of the interactions between the modifiers and the chitosan/alginate scaffold, small-angle neutron scattering (SANS) in solution was used to investigate the impact of the addition of modifiers Ca^{2+} and chondroitin individually on the structural features of the chitosan/alginate network. This approach has allowed us to trace how the structural features at the level of

individual fiber and the polysaccharide network as a whole are translated into the bulk material properties upon freeze-drying.

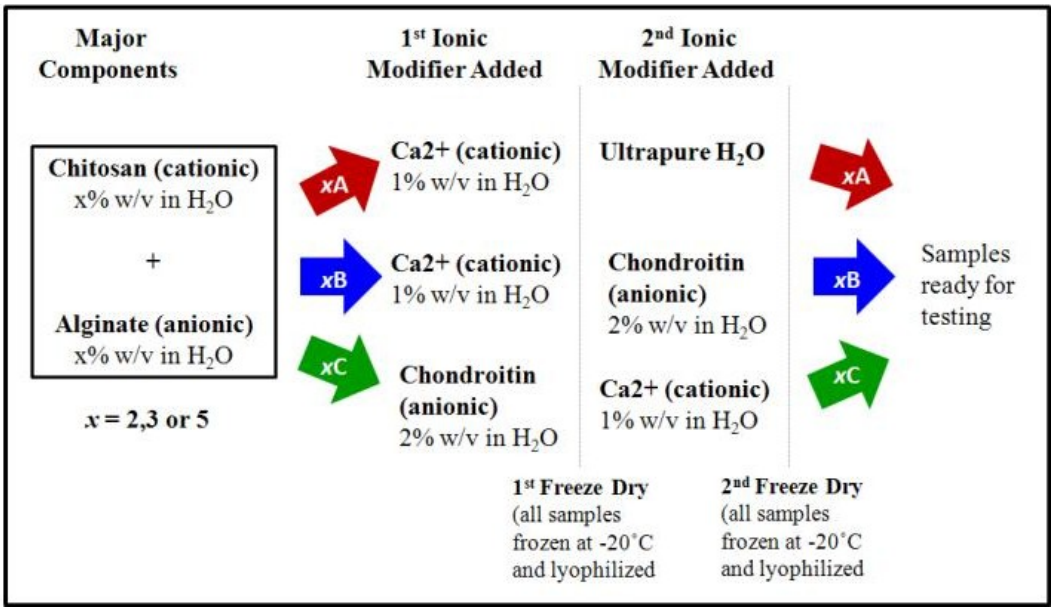

Figure 2.1: Procedures for making the three types of networks, **A**, **B** and **C**. Each network underwent lyophilization twice. *x*% chitosan was mixed with *x*% alginate in a 1:1 volume ratio. Type **A** & **B** samples were made by adding Ca^{2+} to the chitosan-alginate mixture at a volume ratio of 10:1 chitosan-alginate:$CaCl_2$. Type **A** & **B** samples were lyophilized and then soaked in ultrapure H_2O and a mass fraction of 2% chondroitin respectively. Type **C** samples were made by adding chondroitin to the chitosan-alginate mixture at a volume ratio of 6:1 chitosan-alginate:chondroitin. Type **C** samples were lyophilized and soaked in a mass fraction of 1% $CaCl_2$.

2.3 Materials and Methods

2.3.1 Materials

Low molecular weight chitosan (50 to 190 kDa, Sigma-Aldrich), alginic acid sodium salt (350 to 450 kDa, Acros Organics), bovine chondroitin sulfate sodium salt (~20 kDa, Pfaltz & Bauer), hydrochloric acid (HCl, VWR), ammonium hydroxide (NH_4OH, Mallinckrodt Baker), ethanol (EMD) and calcium chloride dihydrate ($CaCl_2 \cdot 2H_2O$, Mallinckrodt Baker) were used as purchased.

2.3.2 Preparation of Networks for Mechanical and Imaging Studies

Solutions of mass fractions 2%, 3% and 5% chitosan were prepared in a mass fraction of 2% HCl in ultrapure water (18.2 MOhm, 2 μm cellulose filter) while solutions of mass fractions 2%, 3% and 5% alginate were prepared in a mass fraction of 2% NH_4OH. Mass fractions of 1% $CaCl_2$ and 2% chondroitin solutions were prepared in ultrapure water (18.2 MOhm, 2 μm cellulose filter). To prepare sample type **A** (Figure 2.1), alginate and chitosan were mixed together at equal concentrations and equal volumes. Type **A** samples were made at three polysaccharide concentrations by mixing mass fractions of 2% chitosan with mass fractions of 2% alginate, mass fractions of 3% chitosan with mass fractions of 3% alginate and mass fractions of 5% chitosan with mass fractions of 5% alginate, with the resulting samples labeled as **2A**, **3A** and **5A**, respectively. The electrostatic interactions between chitosan and alginate upon mixing resulted in fibrous, gel-like materials. After chitosan and alginate mixing, the 1st modifier, 1% mass fraction $CaCl_2$ solution, was added at a volume ratio of 10:1 chitosan-alginate:$CaCl_2$ for all type **A** samples. The samples were then placed in a -20°C freezer overnight and then lyophilized. After lyophilization, dried type **A** samples were soaked in ultrapure water at room temperature for 30 minutes. Samples were frozen at -20°C and lyophilized again. At this point, they were ready for testing. Type **B** samples (Figure 2.1) were also made using the same chitosan and alginate mixing concentrations. Again, the first modifier $CaCl_2$ was added. Dried type **B** samples were then soaked in the 2nd modifier 2% mass fraction chondroitin at room temperature for 30 minutes. The soaked samples were frozen at -20°C and lyophilized once again. Type **C** samples (Figure 2.1) were made by adding 2% mass fraction

chondroitin as the first modifier at a volume ratio of 6:1 chitosan-alginate:chondroitin and 1% mass fraction $CaCl_2$ as the 2nd modifier. For compressive testing, the dried samples were sliced into 12 mm thick dry cylinders. The diameter for each dry cylinder was approximately 20 mm. For tensile testing, the same sample-making procedure was used except samples were sliced into rectangular plates, 10 mm wide and 40 mm long and 2 to 3 mm thick. Finished samples were completely dry, solid materials. Figure 2.2 shows a representative image of the cylinder-shaped version of these freeze-dried samples.

Figure 2.2: A representative image of the cylinder-shaped version of the freeze-dried samples.

2.3.3 Mechanical Testing

Mechanical strength of the freeze-dried networks was assessed using a Tensilon tensile-compressive tester (RTF-1310, Orientec, Japan) with a 50 N load cell. For compressive testing, the guidelines for mechanical testing from ASTM D5024-95a were used as described (*62, 71*). Briefly, the freeze-dried samples were hydrated to saturation and compressed to 30% of their original thicknesses with a constant crosshead speed of 0.4 mm/min. For tensile testing, rectangular freeze-dried networks were hydrated to saturation and elongated until rupture at a crosshead speed of 6.0 mm/min (*72*). Elastic moduli from compressive tests were calculated using the

slopes of their respective stress-strain curves. In order to obtain the most realistic mechanical values, samples were tested in a hydrated state. However, the strongest sample (**5C**) was compressed in a dry state in order to compare with other reported chitosan-alginate strength values (*62*). The ultimate tensile strength was calculated by dividing the maximum load value by the material cross-section. The strongest sample (5C) was also put under tension in a dry state to determine the difference between dry and hydrated states. Five samples were used for each mechanical test. Mechanical testing results are presented as the average of five sample tests with the standard deviation reported as the error.

2.3.4 Scanning Electron Microscopy

10 × 10 mm pieces of each dried sample were examined using Scanning Electron Microscopy (SEM, Hitachi SU-70). Samples were placed on an SEM sample holder and coated with a thin layer of gold (≈30 nm) using a Sputter Coater (Anatech Hummer X). Average pore diameters of the networks were determined using the NIH image analysis program, ImageJ (*73*). Six images from each sample were taken for analysis of the entire sample surface. Every pore was measured in all images.

2.3.5 Material Porosity and Density

A liquid displacement method described by Zhang et al. was modified and used to determine the polysaccharide network porosity and density (*71*). Dried samples of dimensions 7 mm × 7 mm × 7 mm were weighed (W) and then placed in a known volume of liquid (V_1). Air was evacuated from the samples followed by re-pressurization to insure maximum liquid saturation. The residual pressure here was

close to 20 Torr. Air evacuation was done using a modified graduated cylinder, fitted with an attachment for vacuum pumping. The volume of the liquid including the saturated network (V_2) was measured. The saturated network was then removed and the remaining liquid volume (V_3) was measured. The original method used ethanol to determine porosity because it does not cause network swelling. However, we found ethanol evaporation to be a problem during air evacuation. Instead, heptane was used as the displacement liquid. Heptane did not have noticeable evaporation during air evacuation and did not affect network swelling. The density (ρ) and porosity (ε) of the networks were then calculated using the following equations.

$$\rho = \frac{\text{weight of dry network}}{\text{volume of solvated network}} = \frac{W}{V_2 - V_3} \qquad (2.1)$$

$$\varepsilon = \frac{\text{volume of liquid in solvated network}}{\text{volume of solvated network}} = \frac{V_1 - V_3}{V_2 - V_3} \qquad (2.2)$$

2.3.6 Preparation of Networks for SANS Study

Chitosan, alginate, chondroitin and calcium chloride solutions were prepared in D_2O to enable adequate contrast between the hydrogen-rich networks and the solvent. Solutions of mass fraction 2% chitosan were made in D_2O containing a mass fraction of 2% HCl and solutions of mass fraction 2% alginate were made in D_2O containing a mass fraction of 2% NH_4OH. Solutions of a mass fraction of 1% chondroitin and 0.5% $CaCl_2$ were each made in D_2O. Five samples were prepared for measurement (Table 2.1). The calcium containing sample was made by mixing a mass fraction of 2% chitosan with a mass fraction of 2% alginate in equal volumes and then calcium was added at a volume ratio of 10:1 chitosan-alginate:$CaCl_2$. The

chondroitin containing sample was made using the same chitosan and alginate mixture and chondroitin was added at a volume ratio of 6:1 chitosan-alginate:chondroitin. Mixtures were prepared within titanium sample cells with 30 mm diameter quartz windows and a 2 mm path length. Samples were prepared within 12 hours of measurements. Of note, the samples for SANS experiments were not

Table 2.1: Structural data from SANS analysis. Correlation length (l_c), mass-fractal (d), mass-fractal prefactor (B) and radius of gyration of the cross-section (R_c), were analyzed for chitosan/alginate samples. Each mixture was made with equal volumes of a mass fraction of 2% chitosan and a mass fraction of 2% alginate. The calcium-containing sample was made by adding Ca^{2+} to the chitosan/alginate mixture at a volume ratio of 10:1 chitosan-alginate:$CaCl_2$ (0.25% $CaCl_2$). The chondroitin-containing sample was made by adding chondroitin to the chitosan/alginate mixture at a volume ratio of 6:1 chitosan/alginate/chondroitin (0.5% chondroitin). The B for chitosan and alginate could not be calculated due to low scattering values.

Samples	l_c (Å)	d	B	R_c (Å)
2% chitosan	147 ± 8	3.0 ± 0.3	-	83
2% alginate	245 ± 9	2.6 ± 0.3	-	88
2% chitosan+ 2% alginate	134 ± 5	2.9 ± 0.2	4.6×10^{-4}	109
2% chitosan + 2% alginate + 0.25% Ca^{2+}	120 ± 5	2.8 ± 0.2	1.0×10^{-4}	92
2% chitosan + 2% alginate + 0.5% Chd	149 ± 8	3.0 ± 0.2	3.9×10^{-4}	126

freeze-dried as opposed to the samples used for SEM, and mechanical, porosity and density studies. We have performed SANS experiments with polysaccharide networks in solution *before* they were freeze-dried in an attempt to get an insight on how the structural characteristics of the polysaccharide networks at the nanoscale level (or the level of individual fiber) are further translated into the bulk material properties. Due to dimensional hindrances of 1-mm quartz-titanium sample cell used in SANS studies, freeze-dried samples could not be loaded. We were also limited to lower concentrations of polysaccharides which contained only one modifier for each. High viscosity of concentrated solutions as well as the diffusion limitations for

modifiers in the restricted environment of the sample cell hampered the extension of our experiments to wider concentration ranges and the addition of a second modifier. However, despite the above limitations, we strongly believe that SANS studies provide solid support for the results of bulk material testing and in some sense could serve as a basis for explanation of the observed material properties.

2.3.7 SANS Structural Analysis

Structures of the networks listed in Table 2.1 were investigated using the 30 m SANS instrument (NG-3) at the National Institute of Standards and Technology (NIST) (*74*). Monochromatic neutrons at $\lambda = 6$ Å with a wavelength spread ($\Delta\lambda/\lambda$) of 0.14 were detected on a 64 cm × 64 cm two-dimensional detector. Data on SANS intensity were collected with a Q-range from 0.001 $Å^{-1}$ to 0.4 $Å^{-1}$ at 25°C. Q is the scattering vector and is related to the wavelength λ and the scattering angle θ by

$$Q = \frac{4\pi}{\lambda}\sin(\frac{\theta}{2}) \qquad (2.3)$$

The instrument has pinhole geometry. Scattering intensities were normalized using direct beam transmission measurements and were reduced according to published protocols (*75, 76*). Processing of the data was performed using IGOR 6.2/IRENA software (*77*) to obtain characteristics at the levels of fiber building and packing. To estimate the density of the cross-linking networks in the samples, the Debye-Bueche model (*78*) was used in the following form

$$I(Q) \propto \frac{L_c^3}{(1+ \quad ^2 L_c^2)^2} \qquad (2.4)$$

where L_c is the correlation length. The correlation length of a network is a measure of

the spatial extent of the cross-linking regions and reflects the average mesh size. A larger correlation length value correlates with a larger average mesh size (*79*).

Mass-fractal dimensions were estimated using the fractal model (Dr. A. Allen, NIST) implemented in IRENA and described in detail within the program. Fractal analysis is often used to analyze materials that have a repetitive unit, an elementary "building brick" which is appropriate for our oligopeptide/polysaccharide systems. Fractal analysis is done in the high-Q region of the $I(Q)$ *vs*. Q plot. This region corresponds to a range of distances smaller than the size of the scattering objects so that the scattered neutrons are probing the local structure of the hydrogel network. The fractal dimension (d) in mass-fractal analysis is a number ranging from 1 to 3, and defines the structural characteristics of the "building brick." For instance, d is 1 in the case of stiff rod-like repetitive units; d is 2 for the Gaussian-coil-shaped structures, and d is 5/3 for the swollen Gaussian-coils in a good solvent, whereas a value of 2 or greater corresponds to a degree of branching (*80*). Scattering from a mass-fractal is given as

$$I(Q) \propto BQ^{-d} \qquad (2.5)$$

where d is the slope of the Log$I(Q)$ vs. Log$Q$ plot (in the Appendix, Figures A2-A6) and B is the prefactor indicative of dimensional characteristics of a repetitive unit reflecting its degree of swollenness.

The networks under study are formed of fibers with one dimension (length) much longer than the other two (cross-sectional dimensions), and the length of the fibers exceeded the resolution limit (Q_{min}) of the scattering data (in our case $Q_{min} \sim 0.001$ Å^{-1} which means that the maximum length we can reliably characterize is ~

2000 Å). Therefore, we analyzed the scattering data in terms of the cross-sectional dimensions of the scattering particles using standard approach of multiplication of $I(Q)$ by Q, thereby essentially removing the information about the length of the scattering particles (*81*).

Characteristics of individual fibers were acquired with the ATSAS software (*82*). The radius of gyration of the cross-section (R_c) was determined by calculating the pair distance distribution function of the fiber cross-section ($P_c(r)$) using indirect Fourier transform methods in GNOM. The radius of gyration of the cross-section describes the average distance of all area elements of the cross-section from the center of scattering density. The r value at $P_c(r) = 0$ gives the maximum linear dimension for the cross-section of the scattering particle, d_{max}. The radius of gyration of the cross-section of the scattering particle, R_c, is derived from the second moment of $P_c(r)$.

$$P_c(r) = \frac{1}{2\pi^2} \int QI(Q) \cdot r \sin(Q \cdot r) dQ \qquad (2.6)$$

$$R_c^2 = \frac{\int_0^{d_{max}} P_c(r) r^2 dr}{2 \int_0^{d_{max}} P_c(r) dr} \qquad (2.7)$$

Since the scattering intensity is directly proportional to the concentration (in mg/mL) and the molecular weight (in Da) of the constitutive molecules, to normalize pair-wise distribution functions of the cross-section, $P_c(r)$, data for each polymer sample were divided by the sum:

$$\sum_i C_i \overline{M}_i \qquad (2.8)$$

where i is the number of polysaccharide components C_i is the concentration of corresponding component (in mg/mL) and $\overline{M}_i$ is the average molecular weight of the i-th polysaccharide (in Da).

2.3.8 Statistical Analysis

Five experiments were performed per sample for each mechanical, porosity and density test. Six SEM images from each sample were taken for analysis of the average pore size over the entire sample surface. The Tukey-Kramer method was used to determine significant differences between the average pore sizes of different sample sets. One set of SANS data was obtained for structural analysis. SANS analysis was performed on single samples. A Student's unpaired t test or analysis of variance (ANOVA) was carried out to determine the statistical significance ($p < 0.05$) of differences in material mechanical properties, porosity and density.

2.4 Results

2.4.1 Mechanical Testing: Compressive Testing

Shown in Figure 2.3, the elastic moduli for hydrated samples increased with increasing polysaccharide concentration. There was a statistically significant ($p < 0.01$) difference between type **C** elastic moduli at 5% concentrations compared with type **C** at 2 and 3% concentrations, demonstrating network stiffness is affected by polysaccharide concentration for type **C** networks. Type **A** and **B** networks also demonstrate a trend of elastic modulus increase with polysaccharide concentration increase. All type **A** moduli had statistically lower values than comparative type **B** and **C** samples ($p < 0.01$). The presence of chondroitin seemed to improve material

stiffness since the type **A** samples did not contain chondroitin. Additionally, samples **3C** and **5C** had statistically higher elastic moduli ($p < 0.01$) compared with samples **3B** and **5B**. It appears the order of component addition only significantly affects the elastic moduli for the two higher concentration samples. This result may be due to incomplete penetration of chondroitin into the polymer network at higher polysaccharide concentrations if chondroitin is added as the 2nd modifier. The inability of chondroitin to diffuse freely may limit electrostatically-driven chondroitin-chitosan interactions, which could affect mechanical strength of the networks. Unlike chondroitin, Ca^{2+} may be able to overcome steric hindrance because of its much smaller size. Furthermore, it was reported that Ca^{2+} diffusion in higher concentrations of alginate likely increases the number of cross-linking events which improved mechanical strength of alginate hydrogels (*83*). For comparison with reported values, dry **5C** samples were compressed as well, with an elastic modulus of 4.4 ± 0.52 MPa (Appendix, Table A1), giving a significantly larger modulus than the largest previously obtained result (2.56 ± 0.41 MPa) (*62*).

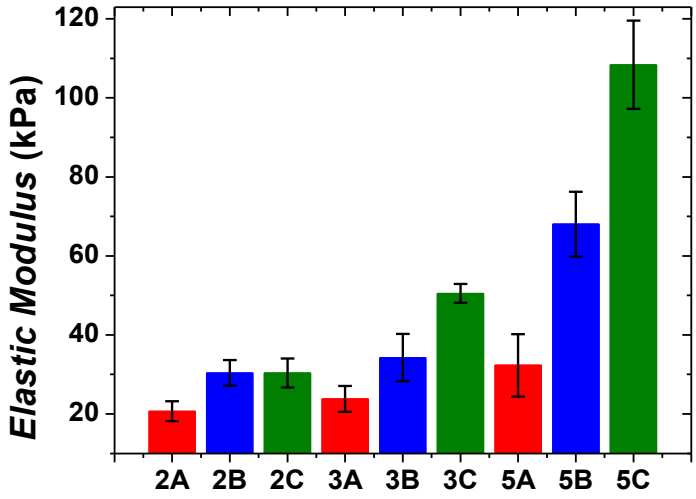

Figure 2.3: Elastic modulus of each hydrated sample type. As total polysaccharide concentration increased, elastic modulus also increased. Samples are identified by mixing order (**A**, **B** or **C**) and by initial mass fractions of chitosan and alginate used (2%, 3% or 5%). Mechanical testing results are presented as the average of five sample tests with the standard deviation reported as the error. The error bars correspond to one standard deviation. Such applies to Figures 2.3, 2.6 and 2.7 as well.

2.4.2 Mechanical Testing: Tensile Testing

As polysaccharide concentration of hydrated samples increased, network tensile strength increased in general (Figure 2.4). Type **C** samples had the greatest ultimate tensile strengths, ranging from 1.8 kPa to 3.2 kPa while type **A** and **B** samples were significantly less ($p < 0.01$). Type **B** samples were either statistically similar or slightly stronger than type **A** samples in terms of tensile strength. Therefore, the addition order of the 2 modifiers is just as important for tensile strength as it is for the compressive strength of the networks. The ultimate tensile strength for dry **5C** samples was 71.2 ± 4.6 kPa which is about 22 times larger than the hydrated tensile strength for **5C** (Appendix Table A1, Figure 2.4).

In summary, mechanical testing shows that, as a modifier, chondoritin can indeed significantly strengthen chitosan/alginate networks, provided chondroitin is added before Ca^{2+}, the other modifier.

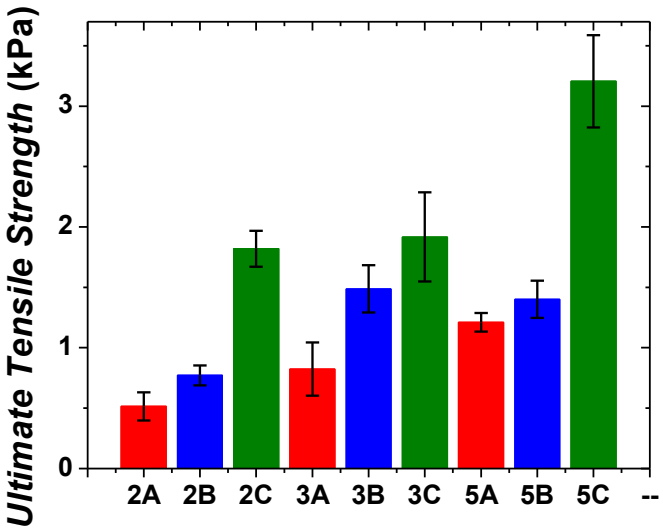

Figure 2.4: Ultimate tensile strength of each hydrated sample type. Type C samples had statistically larger tensile strength values than type B samples possibly due to lack of chondroitin diffusion in type B samples.

2.4.3 Material Pore Size, Porosity and Density

Highly porous and interconnected pore structures are needed to ensure an environment conducive to cell proliferation and attachment in addition to allowing the free flow of nutrients. SEM images (Figure 2.5) suggest material pore sizes are generally very heterogeneous. In Figure 2.6, the histograms also show pore size heterogeneity. To determine whether the average pore sizes for each sample type (**A**, **B**, **C**, **2**, **3** and **5**) were statistically significant from each other, the Tukey-Kramer method was used. At 95% simultaneous confidence levels, average pore size for sample type **B** was greater than **A** and **C**, and sample types **A** and **C** were statistically equivalent. Lack of chondroitin penetration may have induced the fusion of pores during the second freezing event, creating slightly larger pores in type **B** samples. At 95% simultaneous confidence levels, average pore size of sample type **3** was greater than **2** and **5**, and sample types **2** and **5** were statistically equivalent.

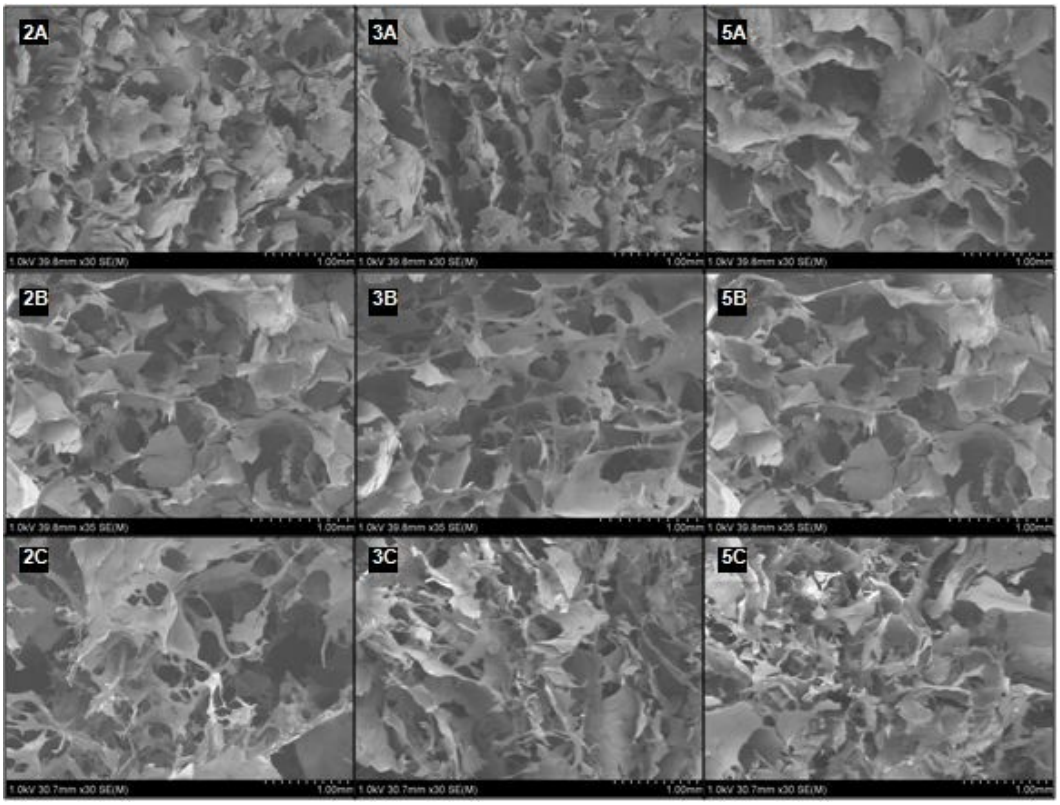

Figure 2.5: SEM images of the nine sample types. Accelerating potential 1.0 kV, 30.7 mm × 30 mm. Sample images depict the heterogeneous nature of the pores. Images are identified by mixing order (**A**, **B** or **C**) and by initial mass fractions of chitosan and alginate used (2%, 3% or 5%) for the purpose of this work.

Larger pores in type **3** samples may have been due to the diffusion of polysaccharides prior to the first freezing. Type **5** samples contained more total polysaccharide content and diffusion may have been slow, resulting in slightly smaller pores. Conversely, type **2** sample polysaccharides could interact freely and form more complex networks consisting of slightly smaller pores. Chung et al. observed a similar heterogeneous pore population for chitosan-alginate networks frozen at -20°C (*63*). Regardless of the mechanism, the data show that there is an optimal polysaccharide concentration in terms of pore size.

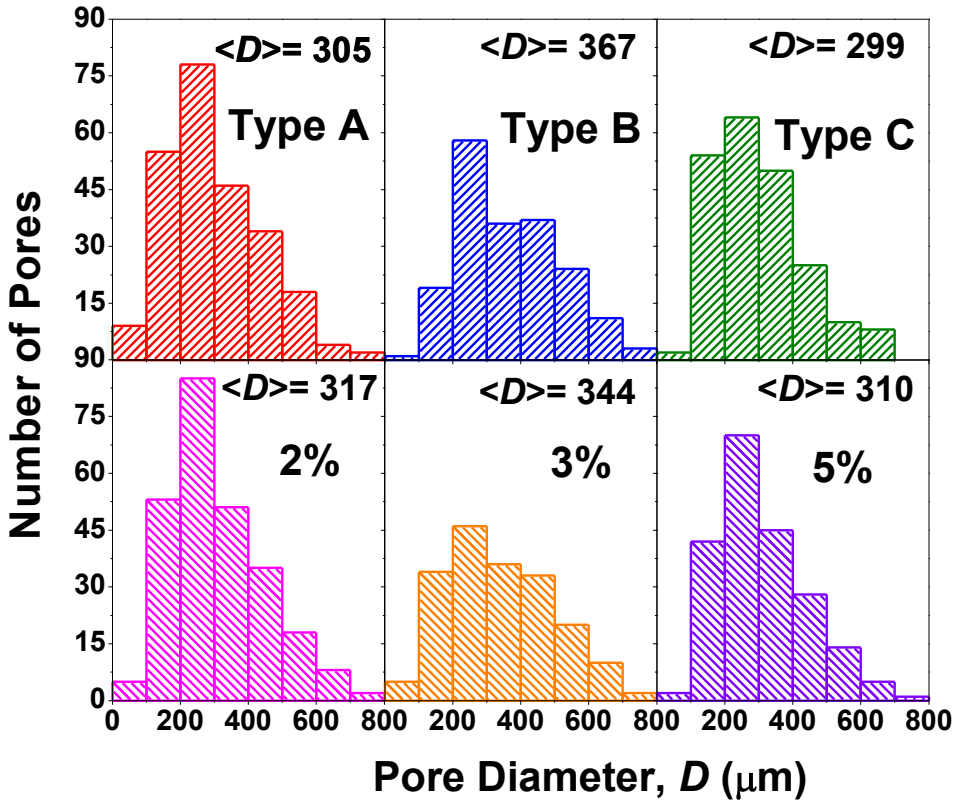

Figure 2.6: Pore size distributions for each sample. Average pore diameter <*D*> is reported for each distribution.

In general, increased material porosity (Figure 2.7) correlates with smaller starting concentrations of polysaccharide. Samples that were made with 2% polysaccharide have an average porosity about 15% higher than samples made with 5% polysaccharide. As for adding chondroitin as an additional modifier, the general trend is that it leads to a decrease in porosity as type **B** and type **C** samples are slightly less porous than type **A** samples. Type **C** samples were also slightly less porous than type **B** samples. More complete chondroitin incorporation in type **B** samples may be the reason for this effect. Porosities and pore sizes of these networks are similar to other chitosan-alginate networks (*61, 62, 71, 84*).

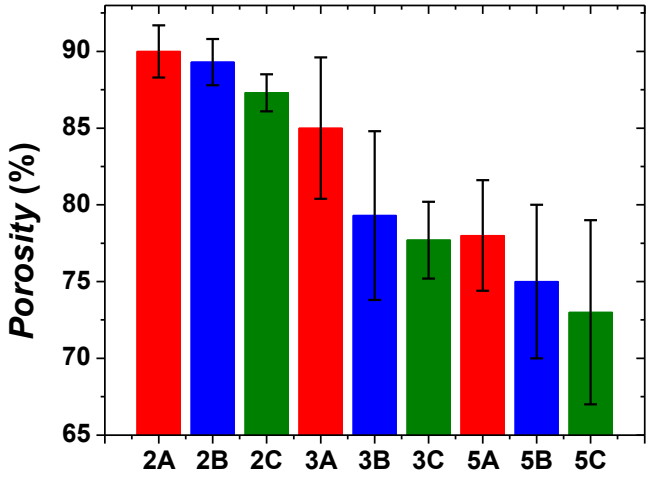

Figure 2.7: Average porosity of each sample. Decreased material porosity correlates with increased polysaccharide concentrations.

As expected, density shows the opposite trend of porosity as higher density correlates with larger starting concentrations of polysaccharide (Figure 2.8); samples that were made with 5% polysaccharide have an average density over two times larger than samples made with 2% polysaccharide. As for adding chondroitin as an additional modifier, the general trend is that it leads to an increase in density as type **B** and type **C** samples have higher densities than type **A** samples. However, the order of chondroitin addition does not seem to affect material density as type **B** and type **C** samples have statistically equivalent densities.

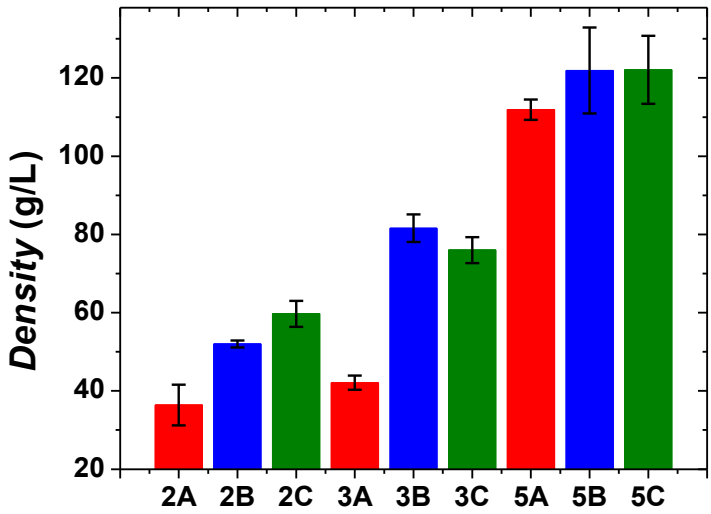

Figure 2.8: Average density of each sample. Increased material density correlates with larger starting concentrations of polysaccharide.

To recapitulate, it seems that when chondroitin is added before Ca^{2+}, it increases the mechanical strength and reduces the average pore size and porosity, in comparison to when Ca^{2+} is added before chondroitin. However, the addition order has no statistically significant effect on the density of the material.

2.4.4 SANS Structural Analysis

Analysis of the SANS data was performed in an effort to understand how the structural differences between polysaccharide networks in solution at the nanoscale level and at the level of individual fibers translate into the bulk material properties after freeze-drying. Different SANS parameters characterize different individual properties of the fibers or the networks, however, taken together they might form a consistent picture of structure-property relationships.

As a rule, the scattering intensity profile $I(Q)$ *vs.* Q characterizes the mass and/or volume of the scattering particle. The larger the mass and/or volume, the

greater the intensity $I(Q)$. In general, one might expect that networks comprised of higher scattering particles, upon freeze-drying, will produce mechanically stronger materials. Another dimensional parameter which describes the fiber cross-section is the radius of gyration of the cross-section R_c, which is obtained from pair-wise distance distribution function of the fiber cross-section $P_c(r)$. A larger R_c characterizes a greater cross-section of the polysaccharide fiber, and thicker fibers are capable of forming stronger materials when freeze-dried.

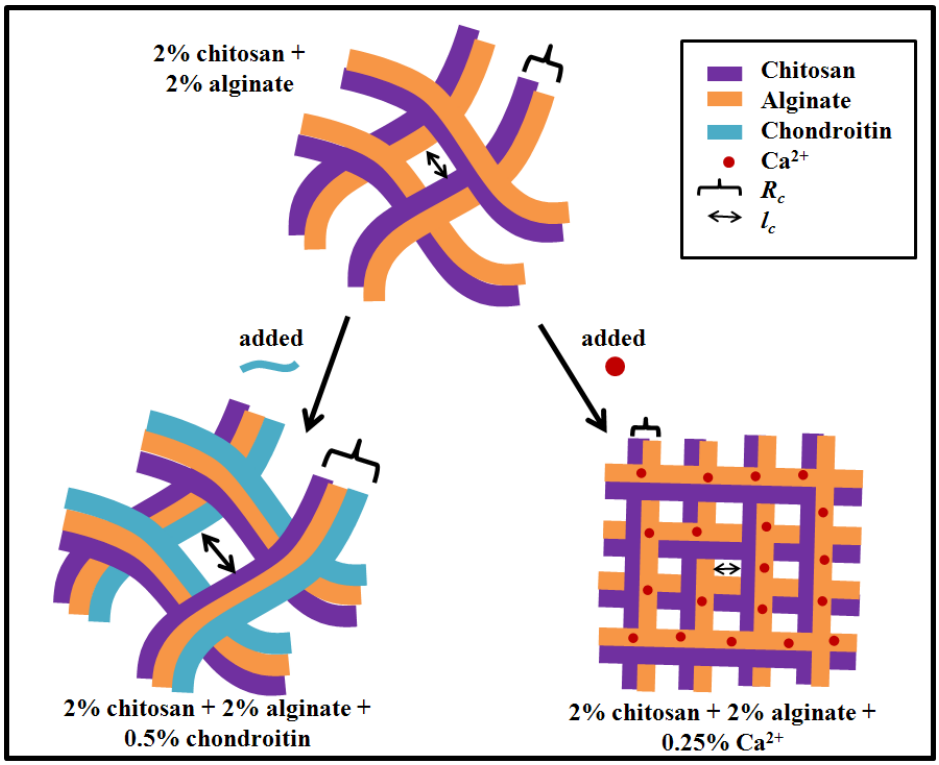

Figure 2.9: A physical depiction illustrating the network parameters obtained from SANS analysis.

One of the important characteristics of the individual fiber is the mass-fractal dimension d which defines the structure of the repetitive unit (building "brick") of the fiber. The packing and compactness of this repetitive unit is characterized by mass-fractal prefactor B, which reflects the degree of swollenness of the unit. Greater B

values correspond to greater swollenness of the polysaccharide fiber building unit, and greater swollenness results in a weaker material after freeze-drying. Correlation length or mesh size l_c defines the properties of the polysaccharide network, and smaller values of l_c are usually attributable to stronger networks. An illustrative summary which compares the parameters examined in these networks can be seen in Figure 2.9. Also, a pictorial explanation of SANS parameters for the polysaccharide networks studied in this chapter has been provided (Figure 2.10).

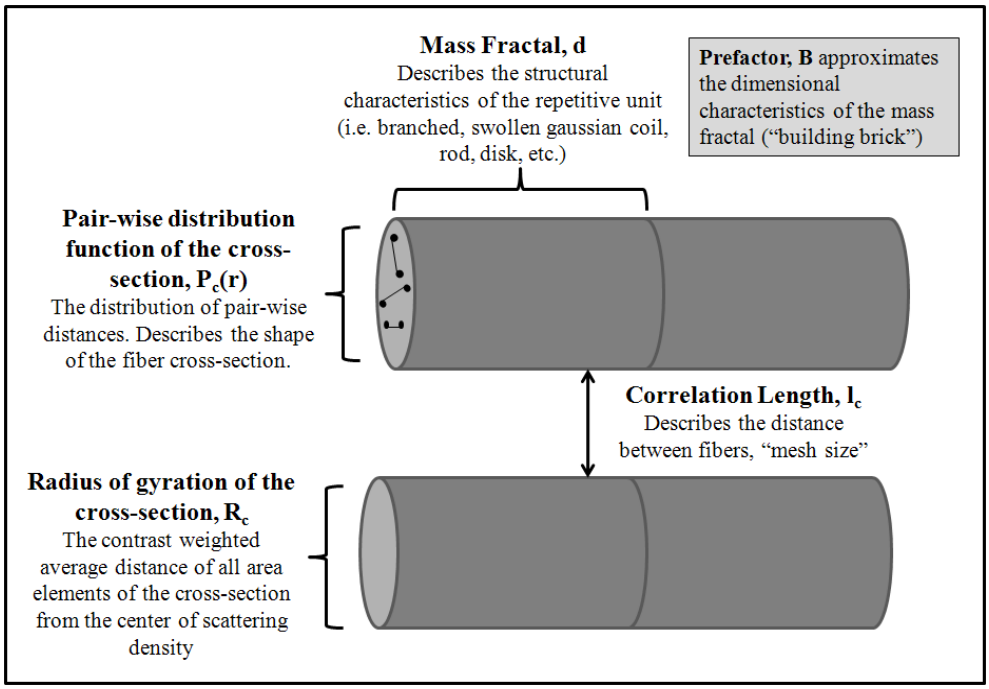

Figure 2.10: Pictorial explanation of SANS parameters.

The measured scattering intensity (Figure 2.11) for each of the networks indicates greater scattering from mixed networks compared with pure alginate and pure chitosan samples. Increased scattering intensity describes the formation of aggregates and is consistent with the development of fibril networks, evidence that chitosan and alginate interactions have occurred. Of the three mixtures, the scattering

intensity for the chitosan/alginate/Ca^{2+} mixture was the smallest and the chitosan/alginate/chondroitin mixture was the largest. This is consistent with the formation of much larger, stronger scattering assemblies in the presence of chondroitin which are capable to reinforce the resulting material after freeze-drying. Indeed, when freeze-dried, the scaffolds containing chondroitin demonstrate the greatest mechanical strength (Figures 2.3 & 2.4).

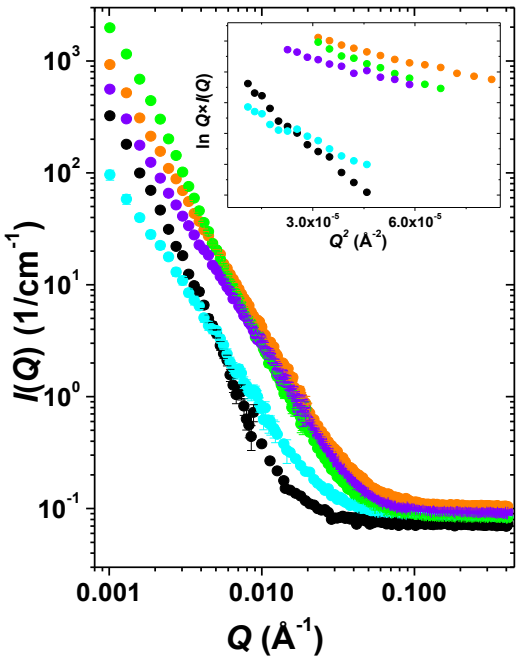

Figure 2.11: *I(Q)* vs. *Q* SANS profiles for multi-component biopolymer networks: chitosan, cyan; alginate, black; chitosan + alginate, orange; chitosan + alginate + $CaCl_2$, violet; chitosan + alginate + chondroitin, light green. Greater *I*(*Q*) values correspond to larger scattering particles, *e.g.*, chitosan + alginate + chondroitin mixture forms the biggest assemblies. Inset plot shows Guinier plots for rod-like particles, *lnQ*I(Q)* vs. Q^2, and the linearity in this region confirms the formation of elongated fibers in all systems. Color code on inset corresponds to main figure. Statistical error bars correspond to one standard deviation and represent error in the scattering intensity estimation. Error bars are large at the instrument configuration overlap region but are smaller than the plotting symbols at low *Q*.

The correlation lengths (l_c, Table 2.1) for the five samples showed that prior to mixing, the average mesh size for alginate was much larger; its correlation length was

larger than the correlation lengths of chitosan and the three mixtures. The correlation lengths for chitosan and the chitosan-alginate mixture are quite similar. The average mesh size of alginate thus decreases during the mixing process which suggests the presence of chitosan-alginate interactions. Interestingly, the correlation length of the Ca^{2+}-containing mixture was smaller than the other two mixtures. These results may occur due to alginate stiffening upon Ca^{2+} addition, which was known to shorten alginate chains. Stokke et al. also observed a similar shortening evident from the relationship between scattering intensity and Ca^{2+} concentration in pure alginate gels using small angle X-ray scattering (SAXS) (*35*). Thus, due to such contraction of the alginate polymer, the addition of Ca^{2+} created a more densely-packed system (smaller correlation length). Smaller mesh-sized networks, in general, should be expected to produce stronger bulk materials after freeze-drying. Therefore, freeze-dried polysaccharide scaffolds modified with Ca^{2+} may demonstrate greater mechanical strength. The correlation length or average mesh size for the chondroitin-containing mixture was the greatest among the three mixtures. A larger correlation length for the chondroitin-containing mixture indicated that addition of chondroitin increased the average mesh size of the polysaccharide network. Mesh size increase may be due to increased fiber thickness upon chondroitin interaction with chitosan-alginate fibers as well as electrostatic repulsion of the negatively charged components. In a system where both these modifiers are added, one might expect chondroitin to increase the fiber thickness and Ca^{2+} to condense and stiffen those fibers into a stronger, compact system. When freeze-dried, this polysaccharide scaffold with two modifiers shows the highest mechanical strength (Figures 2.3 & 2.4).

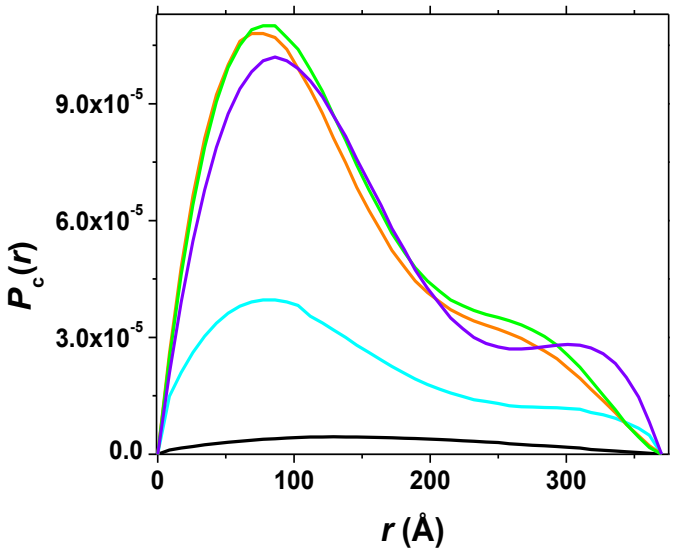

Figure 2.12: Pair-wise distance distribution functions, $P_c(r)$, for the cross-section of the rod-like fibers of multi-component networks: chitosan, cyan; alginate, black; chitosan + alginate, orange; chitosan + alginate + $CaCl_2$, violet; chitosan + alginate + chondroitin, light green. Functions with two maxima are characteristic for the dumbbell shape of the cross-section. Value of r in Å where $P_c(r)$ goes to zero defines the maximum dimension of the cross-section which for all fibers is around 375 Å.

Mass-fractal dimensions, *d*, which define the structure of the repetitive unit of the fiber for all five samples (Table 2.1) point to the formation of randomly-branched swollen polymers (*d* values from 2.6 to 3.0) (*80*). Additionally, the power-law prefactor (*B*) from mass-fractal analysis reflects the dimensions and/or the degree of swollenness of the repetitive unit and is the smallest for the Ca^{2+}-containing samples (Table 2.1). Contraction of alginate upon Ca^{2+} addition decreased the swollenness (*B*) and after freeze-drying this sample may demonstrate greater mechanical strength. The addition of chondroitin also reduced the *B* value slightly compared with the chitosan-alginate mixture. The decreased degree of swollenness is also in agreement with the results showing chondroitin addition directly translates to the strengthening of bulk mechanical properties on freeze-drying.

The radius of gyration of the cross-section (R_c), derived from the analysis of pair-wise distance distribution function of the cross-section ($P_c(r)$), can also be found in Table 2.1. Here, R_c is the contrast weighted average distance of all area elements of the cross-section from the center of scattering density and, in general, it characterizes maximum dimensions of the fiber cross-section. The R_c value for the chitosan-alginate network is larger than the R_c values of separate chitosan and alginate fibers suggesting that upon mixing, chitosan and alginate interact to form a thicker fiber, with a larger cross-section than either chitosan or alginate alone. After Ca^{2+} addition, the R_c value of the chitosan-alginate network becomes smaller, due to the contraction of alginate upon interaction with Ca^{2+}. As mentioned above, such contraction simultaneously leads to a more compact and more dense network as evidenced by the decrease in mesh size l_c and prefactor B (Table 2.1), thus suggesting a stronger bulk material upon freeze-drying. In contrast, after chondroitin addition, the R_c value for the chitosan-alginate network becomes larger due to the incorporation of chondroitin into the chitosan-alginate network and the thicker fiber that results. In Figure 2.12, the pair-wise distance distribution functions of the cross-section $P_c(r)$ are plotted together. These functions reflect the probabilities of finding different distances between two arbitrary points within the cross-section, and the area under the curve characterizes the mass per unit length of the fiber. The pattern of $P_c(r)$ for all three mixtures corresponds to an asymmetrical dumbbell shape of the cross-section, yet the shape is more pronounced in the Ca^{2+}-containing mixture. Fiber contraction upon Ca^{2+} addition may be the reason for this change in shape. Once again, we see that addition of Ca^{2+} causes fiber contraction while chondroitin addition increases fiber

thickness. Together, these modifiers can increase the fiber density and therefore increase the network bulk mechanical properties after freeze-drying.

To summarize, increased scattering intensity describes the formation of aggregates and is consistent with the development of fibril networks, evidence that chitosan and alginate interactions have occurred. Additions of both modifiers individually change the structure of chitosan-alginate networks in different ways. Addition of Ca^{2+} causes the contraction of the network due to Ca^{2+}-alginate interactions. This contraction increased the stiffness of the fibers. Addition of chondroitin causes an increase in fiber thickness due to chondroitin-chitosan-alginate interactions. Increased fiber thickness results in greater material density which in turn may increase material stiffness and strength.

2.5 Conclusions

Tissues such as cartilage, tendons or ligaments exist in mechanically demanding environments. In order to repair or replace these materials, it is desirable to mimic their mechanical strengths in engineered soft biomaterials. Creating the strongest materials possible requires an understanding of how individual network components and various conditions affect bulk material properties. In the present work, we examined how the addition of chondroitin affected the properties of chitosan-alginate networks. Samples containing chondroitin were stiffer and had greater tensile strengths than samples without chondroitin. However, the effectiveness of chondroitin addition was dependent on the order in which it was added. When added after the first lyophilization (type **B** samples), chondroitin could not diffuse into the networks. Therefore, type **B** samples were mechanically weaker than samples

where chondroitin was added prior to the first lyophilization (type **C** samples). Effects of total polysaccharide concentration were also studied. Higher concentrations were associated with greater mechanical strengths. Porosity and density were notably concentration dependent. Pore size was affected by both concentration and order of chondroitin addition. Structural analysis of the networks complemented the findings in this chapter. Correlation length, dimensional characteristics of the repetitive unit and radius of gyration of the cross-section illustrated that chondroitin addition increased fiber thickness while Ca^{2+} addition caused fiber contraction thereby increasing fiber stiffness. Together, the two modifiers improved network density, resulting in greater stiffness and tensile strength. This effort demonstrates the mechanical tunability and enhancement of these materials for various tissue engineering applications.

Chapter 3: Viscoelastic Properties and Nano-scale Structures of Composite Oligopeptide-Polysaccharide Hydrogels

3.1 Abstract

Biocompatible and biodegradable peptide hydrogels are drawing increasing attention as prospective materials for human soft tissue repair and replacement. To improve the rather unfavorable mechanical properties of our pure peptide hydrogels, in this work we examined the possibility of creating a double hydrogel network. This network was created by means of the coassembly of mutually attractive, but self-repulsive oligopeptides within an already-existing fibrous network formed by the charged, biocompatible polysaccharides chitosan, alginate, and chondroitin. Using dynamic oscillatory rheology experiments, it was found that the coassembly of the peptides within the existing polysaccharide network resulted in a less stiff material as compared to the pure peptide networks (the elastic modulus G' decreased from 90 to 10 kPa). However, these composite oligopeptide-polysaccharide hydrogels were characterized by a greater resistance to deformation (the yield strain γ grew from 4 to 100%). Small-angle neutron scattering (SANS) was used to study the 2D cross-sectional shapes of the fibers, their dimensional characteristics, and the mesh sizes of the fibrous networks. Differences in material structures found with SANS experiments confirmed rheology data, showing that incorporation of the peptides dramatically changed the morphology of the polysaccharide network. The resulting fibers were structurally very similar to those forming the pure peptide networks, but

formed less stiff gels because of their markedly greater mesh sizes. Together, these findings suggest an approach for the development of highly deformation-resistant biomaterials.

3.2 Introduction

Self-assembling oligopeptide hydrogels have become increasingly popular materials for tissue engineering (*85, 86*), drug delivery (*87, 88*) and cell culture applications (*89*). Flexibility of oligopeptide sequence design and relative ease of synthesis make oligopeptide hydrogels highly tunable, both chemically and mechanically. Tunability of the oligopeptide building blocks allows for substantial manipulation of bulk material properties. Despite the versatility of oligopeptide hydrogels, these materials remain mechanically weak. Promising methods involving cross-linking by enzymatic oxidation (*90*), electrostatic interactions (*91*), interplay between hydrophilic and hydrophobic interactions (*92*), and disulfide bonds (*93*) have been used to significantly increase elastic moduli.

In this chapter we draw upon another approach commonly used in materials research in order to modify the material properties of oligopeptide hydrogels, by incorporating the fibers of other biopolymers into the oligopeptide fiber network. By designing this composite network, we hoped to create a material with new and/or possibly improved visoelastic properties. Recently, Hosseinkhani et al. created a scaffold combining a oligopeptide amphiphile with a collagen sponge in order to examine the release of growth factor and the formation of bone in the oligopeptide-collagen scaffolds *in vitro* and *in vivo* (*94*). Increased strength and sustained release of growth factor, over a period of several weeks, demonstrates some of the promise of

hybrid biomimetic scaffolds for drug delivery as well as for tissue engineering purposes.

In this section, we designed novel biomaterials assembled based upon our earlier approach which involves electrostatic interactions, described in chapter two (*95*). The polysaccharide portion of the material was assembled from chitosan, alginate and chondroitin. Previously, we found that the combination of these three polysaccharides resulted in a strong, flexible network formed through the electrostatic interactions of positively charged chitosan with negatively charged alginate and/or chondroitin (*95*). The oligopeptide hydrogel portion of the material was comprised of one positively charged oligopeptide and one negatively charged oligopeptide. Based on the discovery that oligopeptides with alternating charged/neutral sequence patterns could self-assemble into hydrogels (*96*), we previously developed a modular approach to the engineering of oligopeptide-based hydrogels (*97-99*). Our general design separates positively and negatively charged amino acids into different oligopeptide chains. As a result of the electrostatic repulsions inherent within each oligopeptide module, spontaneous hydrogelation due to slight pH, temperature and ionic strength changes are avoided. When mixed, the two oppositely charged oligopeptides co-assemble into a hydrodel in phosphate buffered saline (PBS). The polysaccharide networks were premade and then mixed with the oligopeptide pair in solution so that the polysaccharide fibers could interact and form a network with the oligopeptide pair. Properties of the polysaccharide and oligopeptide fibrous networks were examined as separate materials and mixed together. We hypothesized that since every component in this material is charged, interaction between polysaccharides and

oligopeptides is highly likely, thereby increasing the total number of electrostatic interactions in this system and creating a material with new viscoelastic properties.

This study is focused on correlating the structures of separate oligopeptide and polysaccharide networks as well as composite oligopeptide-polysaccharide networks at the nanoscale level to their bulk viscoelastic properties. To this end, dynamic oscillatory rheology experiments probing the mechanical strength, dynamic network characteristics as well as the brittleness of each material were performed. These experiments were followed by the analysis of structural characteristics of the fibrous networks under study as well as the individual fiber dimensional characteristics using small angle neutron scattering (SANS).

3.3 Materials and Methods

3.3.1 Materials

Low molecular weight chitosan (50 to 190 kDa, Sigma-Aldrich), alginic acid sodium salt (350 to 450 kDa, Acros Organics), bovine chondroitin sulfate sodium salt (~20 kDa, Pfaltz & Bauer), hydrochloric acid (HCl, VWR) and ammonium hydroxide (NH_4OH, Mallinckrodt Baker) were used as purchased.

3.3.2 Oligopeptide Design and Synthesis

Oppositely charged peptide modules have been designed in accordance with an earlier approach (*97*) whereby these co-assemble into a hydrogel when mixed due to electrostatic attractions. Both sequences are palindromic, and the *N*-, *C*- termini of each peptide module are acetylated (*Acetyl*-) and amidated (-*amide*), respectively, to block terminal charges. The positive sequence contains alternating positively charged

(lysine, K) and neutral (tryptophan, W; and alanine, A) amino acids, while the negative sequence contains alternating negatively charged (glutamate, E) and neutral (tryptophan, W; and alanine, A):

Positive sequence: ***Acetyl*-K-W-K-A-K-A-K-A-K-W-K-*amide*** **(KWK)**

Negative sequence: ***Acetyl*-E-W-E-A-E-A-E-A-E-W-E-*amide*** **(EWE)**

Oligopeptides were synthesized on Rink-amide MBHA resin by means of a CEM microwave synthesizer using Fmoc solid-phase peptide synthesis (*100*). All amino acids and reagents were dissolved in 100 % dimethylformamide (DMF). The crude peptides were cleaved by a TFA/TIS/H_2O (95/2.5/2.5) cocktail for 2 × 2 hours and the side chain protecting groups were removed at the same time. TFA was removed by rotary evaporation under reduced pressure, and then the crude peptides were precipitated and washed twice by cold ethyl ether.

The crude peptides were dissolved in water and lyophilized before purification. Preparative reverse-phase HPLC method was used to purify the crude peptides. In the purification of **KWK**, solvent A was 0.1 % mass fraction HCl in water and solvent B was 0.1 % mass fraction HCl in MeOH; in the **EWE** purification, solvent A was 20 mmol/L NH_4HCO_3 in water (pH 7.0), solvent B was 20 mmol/L NH_4HCO_3 (pH 7.0) in MeOH/water (8:2). Chromatographic method of peptide purification: 0-40 % B in 0-60 min, 40-100 % B in 60-90 min with linear gradient for each segment was performed. The purity of **KWK** and **EWE** was verified by reverse-phase HPLC analysis (see Appendix figure A8). The solvents used were the same as for the preparative HPLC run. Molecular weights of **KWK** and **EWE** were verified by ESI-MS in positive and negative modes, respectively (see Appendix figure A7).

Purified peptides were dissolved in phosphate-buffered saline at pH 7.4. Concentrations of the individual peptide solutions (16 mmol/L or 32 mmol/L) were determined on the basis of the molar absorptivity of tryptophan at 280 nm (ε_{280} = 5690 M^{-1} cm^{-1}) (*101*). All hydrogel measurements were conducted at a final concentration of 8 mmol/L of each peptide.

3.3.3 Dynamic Rheometry Sample Preparation

Five different samples were prepared and were labeled by their components (**C** = chitosan, **A** = alginate, **D** = chondroitin, **P** = peptides): chitosan+alginate hydrogel (**CA**), chitosan + alginate + chondroitin hydrogel (**CAD**), peptide hydrogel (**P**), chitosan + alginate + peptide hydrogel (**CAP**), and chitosan + alginate + chondroitin + peptide hydrogel (**CADP**). Stock solutions of chitosan, alginate and chondroitin were made in phosphate buffered saline (PBS) at 1.5 % mass fraction. Chitosan solution also required the addition of 1 % mass fraction HCl in H_2O to dissolve. Stock solutions of both peptides were made in PBS at pH 7.4 at 4.54 % mass fraction (32 mmol/L). All sample preparation procedures and measurements were performed at 25 °C and the final pH for all samples was 7.4.

To prepare the **CA** network, stock solutions of chitosan and alginate were diluted to 0.5 % mass fraction by PBS, and equal volumes (1:1), 200 μL of each diluted solution were mixed together by simultaneous pipetting through a Y-shaped connector into the sealed cell of the rheometer. The measurements of gelation kinetics started immediately after mixing.

To prepare the **CAD** network, stock solutions of chitosan and alginate were diluted to 0.7 % mass fraction by PBS, and after mixing of 143 μL 0.7 % mass

fraction chitosan with 143 μL 0.7 % mass fraction alginate in the rheometer cell through Y-shaped connector, the mixture was allowed to equilibrate for 2 hours (time necessary to build up of **CA** network estimated from the rheology experiments for **CA** network). Then 114 μL of chondroitin solution diluted to 0.28 % mass fraction (to get 7:1 chitosan/alginate to chondroitin weight ratio) was added to the mixture, immediately followed by rheological monitoring of the incorporation of chondroitin into the **CA** network resulting in the formation of **CAD** network.

To prepare the **P** network, stock solutions of individual **KWK** and **EWE** peptides were diluted to 2.27 % mass fraction (16 mmol/L) with PBS buffer at pH 7.4. Diluted solutions of the peptide modules were centrifuged separately for 10 min at 8,000 rpm, and 200 μL of each **KWK** and **EWE** peptides were mixed through Y-shaped connector in the sealed cell of rheometer, immediately followed by monitoring of the gelation process resulting in the **P** network.

The procedure for **CAP** network preparation was similar to the steps used for **CAD** networks described above. Stock solutions of chitosan and alginate were diluted to 1 % mass fraction, and 100 μL of each solution were mixed together in the sealed cell of the rheometer using a Y-shaped connector. After 2 hrs of equilibration (necessary to mature the **CA** network**)**, pH of the network was measured and adjusted to 7.4 by addition of very small volumes (several μL) of concentrated NH_4OH solution. Then, 100 μL of each 4.54 % mass fraction (32 mmol/L) **KWK** and **EWE** peptides solution were mixed with the matured chitosan/alginate network. Rheological measurements of gelation kinetics were started immediately.

To prepare the **CADP** network, stock solutions of chitosan and alginate were

diluted to 1.33 % mass fraction by PBS and 75 μL of each solution were mixed in the sealed cell of the rheometer using a Y-shaped connector. The resulting mixture was equilibrated for 2 hrs (to get mature **CA** network), then 50 μL of chondroitin solution diluted to 0.64 % mass fraction by PBS was added, and the sample was equilibrated for another 10-12 hrs (time necessary for maturation of **CAD** network estimated from the rheology experiments for **CAD** network). Then, 100 μL of each 4.54 % mass fraction (32 mmol/L) **KWK** and **EWE** peptides solution were mixed with the matured chitosan+alginate+chondroitin network. Rheological measurements of gelation kinetics were started immediately.

In all samples final concentrations for components in each sample were (in % mass fraction): chitosan (0.25 %), alginate (0.25 %), chondroitin (0.076 %), two peptide modules together (2.25 % or 16 mmol/L). During the equilibration procedures, mixtures in the sealed cell were covered with parafilm to prevent sample drying.

3.3.4 Dynamic Rheometry Measurements

Dynamic rheological measurements were performed using a NOVA Rheometer (REOLOGICA Instruments, Inc., Sweden) featuring a null balance system which allows for nano-torque and nano-strain measurement control and analysis. The instrument is also equipped with a sealed-cell geometry which prevents dehydration of the water-based samples during prolonged measurements. In addition, to exclude possible dehydration of the sample at 25 °C, a simple in-house designed system was used to humidify the incoming air used for the sealed-cell. Rheological

characterizations of the samples were performed using a 25 mm diameter cone-and-plate steel geometry.

Time-sweep measurements were conducted at 0.2 % strain amplitude and 1 rad/s angular frequency. The data points were taken once every 180 s after two integrations with 5 s delay time, between the start of application of the respective stress and the start of data acquisition for calculations. This delay is necessary for equilibration of the plate before the torque measurement.

After the time-sweep measurements, frequency-sweep measurements were conducted at the respective temperatures with 0.2 % strain amplitude, while the frequency was varied from 0.01 to 100 rad/s in a log mode with 18 data points per frequency decade. In the frequency-sweep experiment, the number of integration cycles, N_c, was varied from 1 to 500. The greater number of integration cycles corresponds to higher frequency values. $N_c \approx 1 + 500 \times (\omega_i/\omega_{max})$, where ω_i is the angular frequency of the i-th measurement, ω_{max} is the maximum angular frequency, and here ω_{max} = 100 rad/s. The delay time between the start of application of the respective frequency and stress and the start of data acquisition for calculations was varied from 65 s to 5 s, in reciprocal proportion to the frequency.

After the frequency-sweep measurements and before the strain-sweep measurements, a time-sweep of 3 hr was performed on the gel at 0.2 % strain amplitude, 1 rad/s frequency to confirm that the gel remains undisturbed by the frequency-sweep (see Appendix figures A13-A17). Strain-sweep measurements were then performed with a single integration cycle at 1 rad/s frequency, within the range

of strain amplitudes from 0.1 % to 100 % in a log mode with 23 data points per decade.

3.3.5 SANS Sample Preparation

The conditions and procedures for the preparation of the networks for SANS studies were described in the details above for the dynamic rheology. All samples were made inside titanium cells with 1-mm path lengths and quartz windows 30 mm in diameter, which are routinely used for SANS measurements at the National Institute of Standards and Technology (NIST) Center for Neutron Research (NCNR). For the mixed oligopeptide-polysaccharide networks, the preparation steps and time for equilibration of the intermediate mixtures before the addition of the 3^{rd} and/or 4^{th} component were exactly the same as described above for rheological experiments. Since no kinetic measurements were performed using SANS, all samples were prepared at least 72 hrs before the measurements (time necessary to make **CAP** and/or **CADP** networks was estimated from the rheology experiments).

3.3.6 SANS Structural Analysis

Sample structures were elucidated using the same SANS instrument as described in chapter 2 of this dissertation. Also, the correlation length and fractal analysis were performed using the same techniques described in chapter 2.

In addition to previously described techniques, we used a simulated annealing algorithm which follows the common approach used for 3D dummy atom shape restoration of the scattering particle (*102*). However, we implemented the algorithm in a purpose-written program that is described elsewhere (*103*), to model the 2D

average cross-sectional shape of the fibers under study. In all these calculations, the dummy atoms were arranged on a flat grid of 50 × 100 close-packed dummy atoms. The size of each atom was 5 Å. The program calculated the pair distance or vector length distribution function, $P_c(r)$, for the model cross-section composed of the dummy atoms. P_c(r) is the distribution of distances between area elements in the cross section, weighted by the scattering density at each radial value, *r*. The Fourier transformation of $P_c(r)$ yields the model scattering profile for cross-section $QI_{mod}(Q)$. In the optimization procedure, the program minimized the discrepancy between the model scattering data $I_{mod}(Q)$ and the experimental scattering data $I_{exp}(Q)$ (*53*). After optimization, values for zero-angle scattering intensity $I_c(0)$, the area of the cross-section S_c, maximum cross-sectional dimension D_{max}, and the radius of gyration of the cross-section R_c, were determined from $P_c(r)$; D_{max} was the *r* value at which $P_c(r)$ goes to 0. The zeroth and the second moments of $P_c(r)$ yield $I_c(0)$ and R_c values, respectively. The radius of gyration of the cross-section R_c was the contrast-weighted mean distance of all area elements from the center of scattering density. The program also outputs the model cross-sections as atomic coordinate files in the Protein Data Bank format which allowed their pictorial presentation. These cross-sections are representative of average cross-sections within each sample type. The solutions are unique and characterized by low Chi-squared values ($\chi^2 \sim 1.0 - 1.1$). χ^2 values less than 2 give acceptable fitting for this model, where χ^2 calculations were described in detail (*103*). Corrections for scaling and incoherent background were applied to the model scattering profile so it could be compared directly with experimental scattering data (*103*).

We have also explored the three-dimensional morphology of mixed oligopeptide-polysaccharide hydrogels using the program SAXSMorph (*104*). 2D slices of the hydrogel bulks created by SAXSMorph were then analyzed using the NIH image analysis program ImageJ (see Appendix figure A18) (*105*).

3.4 Results

3.4.1 Mechanical Properties of Oligopeptide-Polysaccharide Hydrogels

Time-sweep rheological monitoring of the gelation kinetics of **CA** (Figure 3.1(A)) showed that pairing of positively charged chitosan and negatively charged alginate resulted in a very weak material with an elastic modulus G' value of only ~ 100 Pa. While the viscous modulus G'' was lower than G', the value of the phase angle δ was still only around 30°, which is indicative of a weak hydrogel network. The frequency spectrum (Figure 3.1(B)) suggests that the **CA** hydrogel is rather mobile showing strong growth in G' at higher frequencies due to relaxation, with an evident maximum of G'' at frequencies around 20 rad/sec. At the same time, the fibrous network formed by the **CA** did not show the signs of break, up to 100 % strain (γ) (Figure 3.1(C)). Addition of chrondroitin to **CA** resulted in the incorporation of chondroitin into the already formed **CA** network.

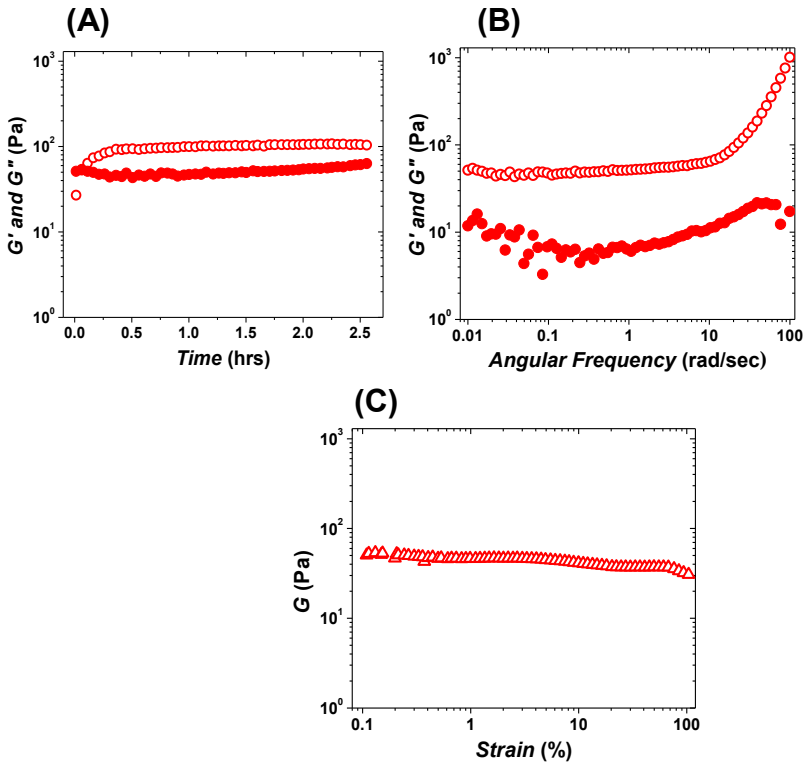

Figure 3.1: Dynamic oscillatory rheological characterization of **CA**. (A) Time-sweep monitoring of gelation kinetics; plateau G' ~ 100 Pa; final $\delta \sim 30°$. (B) Frequency-sweep after viscoelastic modulus reached plateau, max G'' at $\omega \sim 20$ rad/sec. (C) Strain-sweep performed after frequency-sweep; Elastic modulus G' (open circles); viscous modulus G'' (solid circles); shear modulus G (triangles).

This is evident from further slow growth in the G' value, which within ~8–10 hours plateaued at ~ 400 Pa (Figure 3.2(A)). The resulting **CAD** hydrogel was characterized by a smaller phase angle as compared to **CA** ($\delta \sim 9°$). However, the frequency spectrum of **CAD** was very similar to that of **CA** and is also characteristic of a mobile gel where G' is growing at higher frequencies due to relaxation, and a maximum G'' observed around 90 rad/sec (Figure 3.2(B)). Unlike **CA**, in strain-sweep experiments **CAD** demonstrated apparent shear-thinning properties (cf. Figure

3.1(C) and Figure 3.2(C)). Yet, **CAD** was very elastic and retained a low phase angle value ($\delta \sim 12°$) up to $\gamma \sim 100$ % (Figure 3.2(C)).

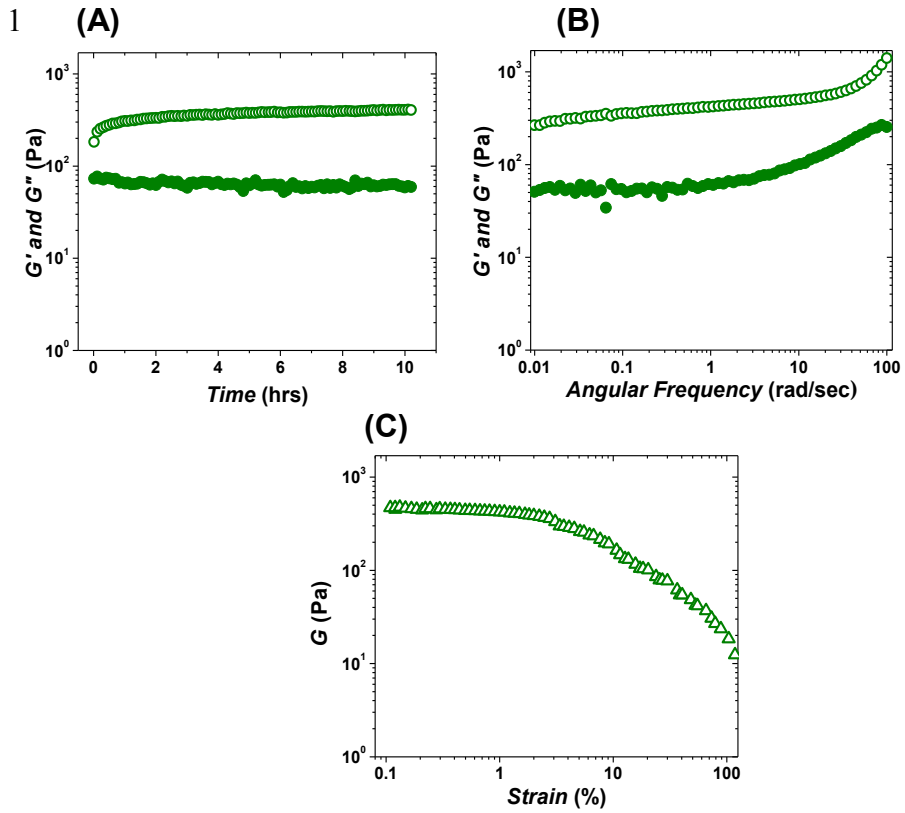

Figure 3.2: Dynamic oscillatory rheological characterization of **CAD.** (A) Time-sweep monitoring of gelation kinetics after addition of chondroitin to **CAD** network; plateau $G' \sim 400$ Pa; final $\delta \sim 9°$. (B) Frequency-sweep after viscoelastic modulus reached plateau, max G'' at $\omega \sim 90$ rad/sec. (C) Strain-sweep performed after frequency-sweep; Elastic modulus G' (open circles); viscous modulus G'' (solid circles); shear modulus G (triangles).

Gelation of the peptide pair **KWK+EWE** continued for ~ 48 hours after mixing and resulted in a fairly stiff hydrogel **P** with a plateau $G' \sim 90$ kPa (Figure 3.3(A)). As opposed to both polysaccharide networks **CA** and **CAD**, peptide hydrogel **P** formed a very stable, solid-like material. The observed log $G'(\omega)$ and $G''(\omega)$ profiles showed a small dependence on the frequency within the studied range from 0.01 rad/sec to 100 rad/sec. This result confirms the formation of

a solid-like hydrogel network with little or no mobility at time scales up to $t = 2\pi/\omega \sim$ 600 sec, *i.e.*, up to the longest measurement duration (Figure 3.3(B)). Also unlike **CA** and **CAD**, **P** was more brittle (yields at $\gamma \sim$3-4 %) and completely broke into a very inhomogeneous mass above $\gamma \sim$ 6 % (Figure 3.3(C)).

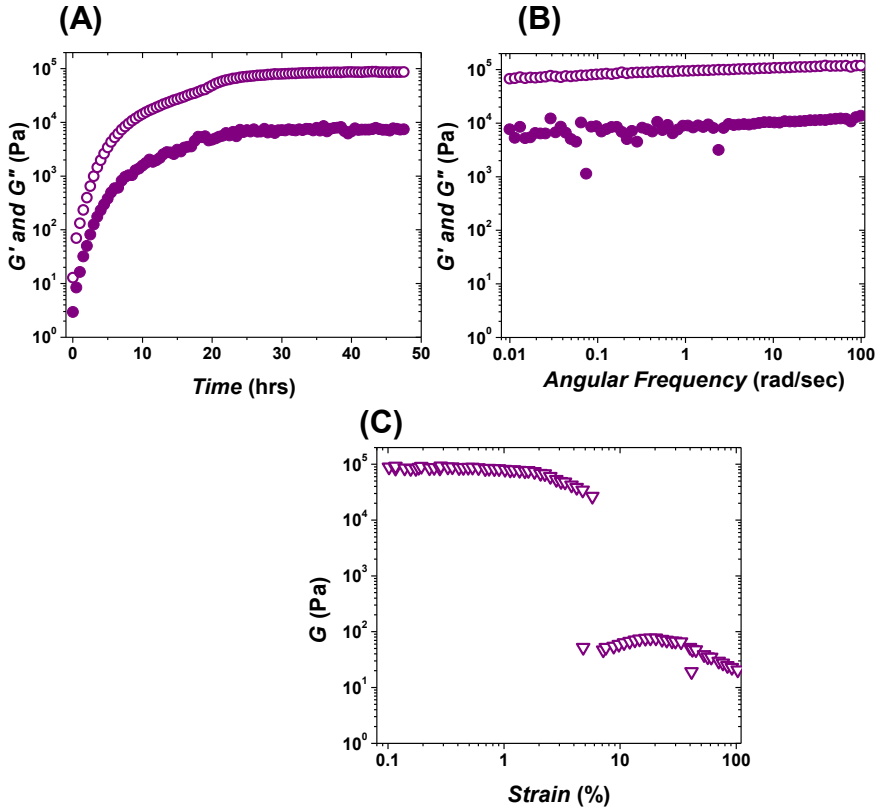

Figure 3.3: Dynamic oscillatory rheological characterization of **P**. (A) Time-sweep monitoring of gelation kinetics; plateau $G' \sim 90$ kPa. (B) Frequency-sweep after viscoelastic modulus reached plateau. (C) Strain-sweep performed after frequency-sweep; yield strain value $\gamma \sim$ 3-4 %; complete break of hydrogel at $\gamma \sim$ 6 %. Elastic modulus G' (open circles); viscous modulus G'' (solid circles); shear modulus G (triangles).

In order to incorporate the oligopeptide fibers into the polysaccharide networks, we conducted the gelation process by mixing individual peptide modules **KWK** and **EWE** with an already existing **CA** network. Interaction of charged peptides with the **CA** network is evident from the observed growth in the viscoelastic

moduli, which in 72 hrs after adding of **KWK** and **EWE** results in a plateau $G' \sim 10$ kPa (Figure 3.4(A)). The resulting composite **CAP** gel was significantly less stiff as compared to the pure peptide network **P** (cf. Figure 3.3(A)), and showed a slightly high phase angle, $\delta \sim 17°$. However, mutually attractive **KWK** and **EWE** incorporated into the **CA** gel markedly stabilized the assembled **CAP** network. The frequency sweep (Figure 3.4(B)) was characteristic of a stable, solid-like material. Similarly to the **P** gel (cf. Figure 3.3(B)), **CAP** showed little mobility up to 600 sec. Unlike the **P** gel, the presence of **CA** fibers within the peptide hydrogel network improved the strain resistance of **CAP** (Figure 3.4(C)) and made it virtually unbreakable. Even at the highest strain value ($\gamma \sim 100$ %), δ still remained around 25-30° (< 45°).

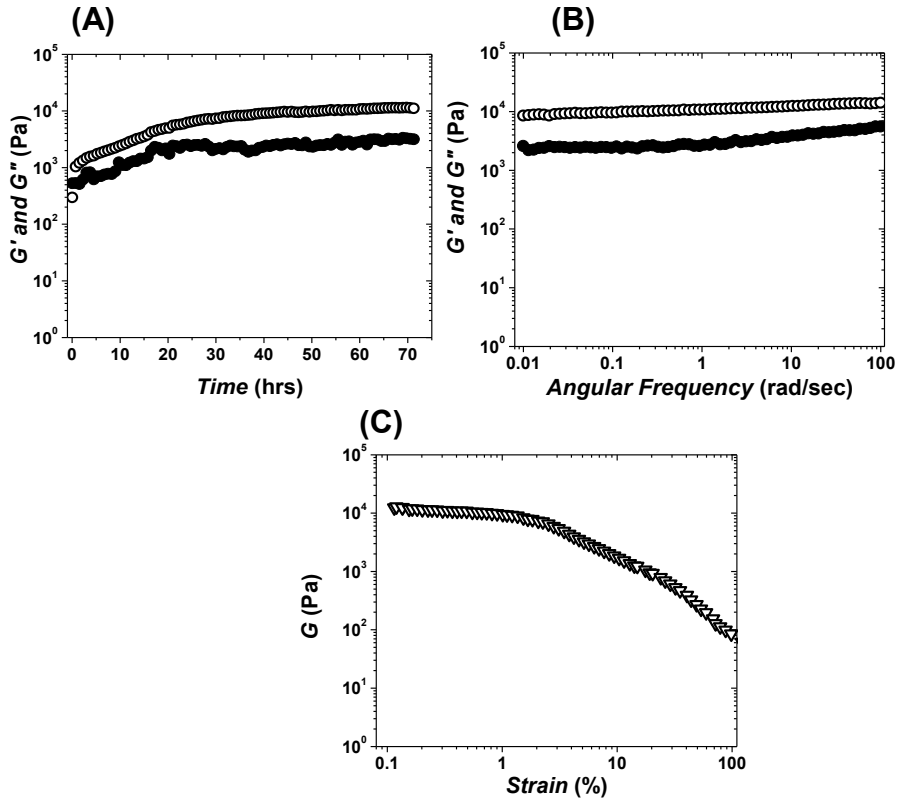

Figure 3.4: Dynamic oscillatory rheological characterization of **CAP.** (A) Time-sweep monitoring of gelation kinetics; plateau $G' \sim 10$ kPa; final $\delta \sim 17°$. (B) Frequency-sweep after viscoelastic modulus reached plateau. (C) Strain-sweep

performed after frequency-sweep; retaining $\delta \sim$ 25-30° even at strain values $\gamma \sim$ 100 %. Elastic modulus G' (open circles); viscous modulus G'' (solid circles); shear modulus G (triangles).

The elastic behavior in the composite oligopeptide-polysaccharide hydrogels became even more evident when oppositely charged **KWK** and **EWE** peptides co-assembled within the already matured **CAD** network. After 72 hrs of gelation, the resulting **CADP** hydrogel reached the same plateau value of elastic modulus ($G' \sim$ 10 kPa) as was observed in the case of **CAP** hydrogel (cf. Figure 3.5(A) and Figure 3.4(A)). However, unlike **CAP**, **CADP** demonstrated more profound solid-like behavior characterized by a rather low phase angle, $\delta \sim$ 5°. The frequency sweep for **CADP** was similar to that of **P** and **CAP** (cf. Figure 3.5(B), Figure 3.3(B), and Figure 3.4(B)) and points to the formation of a very stable, immobile hydrogel. Also, the presence of polysaccharides in **CADP** hydrogel improved the resistance of **CADP** to deformation. The strain sweep (similar to **P**) became non-linear at $\gamma \sim$3-4 %, however, **CADP** was much less brittle and broke only around $\gamma \sim$20 % (cf. Figure 3.5(C) and Figure 3.4(C)). At the same time, **CADP** showed somewhat greater brittleness as compared to **CAP**.

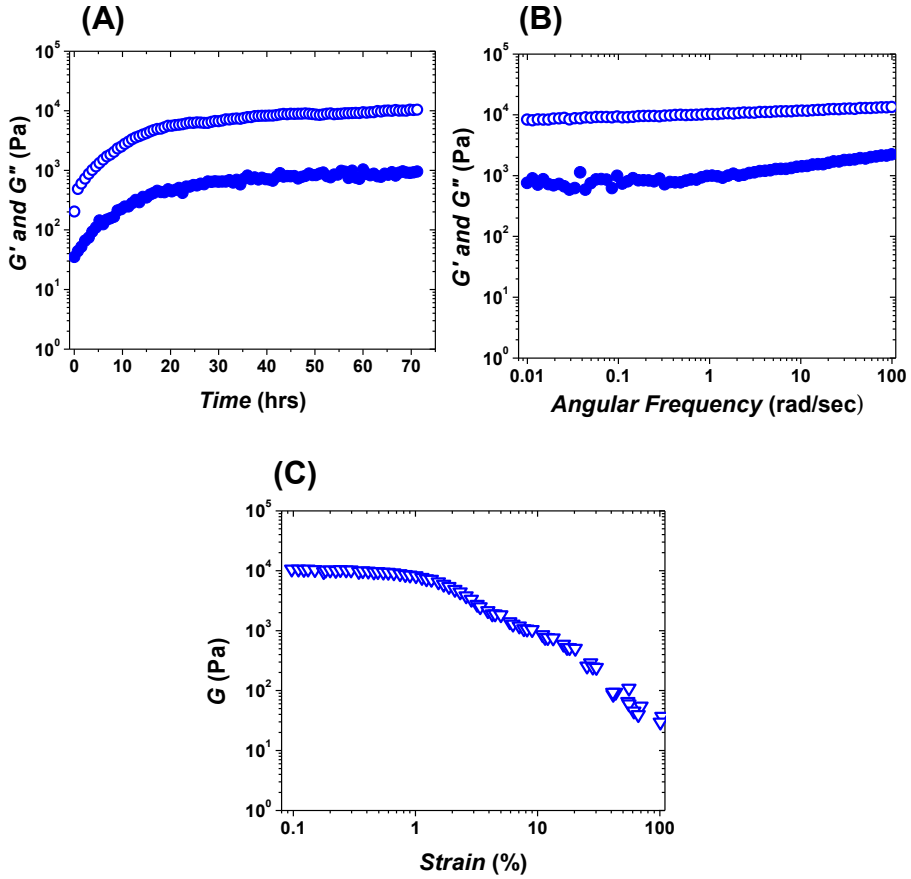

Figure 3.5: Dynamic oscillatory rheological characterization of **CADP.** (A) Time-sweep monitoring of gelation kinetics; plateau G' ~ 10 kPa; final δ ~ 17°. (B) Frequency-sweep after viscoelastic modulus reached plateau. (C) Strain-sweep performed after frequency-sweep and 3 hrs of equilibrating time-sweep (see, Materials and Methods); yield value γ~ 3-4 %; complete break of hydrogel at γ~ 6 %. Elastic modulus G' (open circles); viscous modulus G'' (solid circles); shear modulus G (triangles).

In summary, the above observations show that incorporation of peptides into the already existing fibrous networks of polysaccharides results in less stiff hydrogels (characterized by lower elastic moduli) as compared to the pure peptide network. On the other hand, the oligopeptide-polysaccharide composite hydrogels **CAP** and **CADP** exhibit much greater resistance to deformation. **CAP** hydrogels are virtually

unbreakable up to ~ 100 % strain and are far less brittle as compared to the stiffer peptide hydrogel **P**. The difference in mechanical properties detected for the oligopeptide-polysaccharide composite hydrogels **CAP** and **CADP** as compared to the peptide hydrogel **P** could be explained by the interactions of oligopeptides with polysaccharides. Indeed, it has been shown that oligopeptides are capable of forming complexes with polysaccharides. Such complexation with polysaccharides could efficiently interfere with the attraction of oppositely charged **KWK** and **EWE** and hinder their co-assembly and packing into the fibers. This interference could lead to much less stiff **CAP** and **CADP** hydrogels as compared to **P**.

3.4.2 Structural Analysis of Oligopeptide-Polysaccharide Hydrogels Using SANS

The analysis of structural characteristics of the hydrogels using SANS was employed to explore the relationships between the structural characteristics of the fibrous networks at the nanoscale level and the mechanical properties of bulk material formed by such networks.

In the SANS experiments, all five hydrogel networks, **CA**, **CAD**, **P**, **CAP** and **CADP**, showed an increased scattering intensity consistent with the formation of large assemblies (Figure 3.6). It can be seen in Figure 3.6 that the composite oligopeptide-polysaccharide hydrogels **CAP** and **CADP** (as well as the pure peptide hydrogel **P**) show much greater scattering intensities as compared to pure polysaccharide networks **CA** and **CAD**.

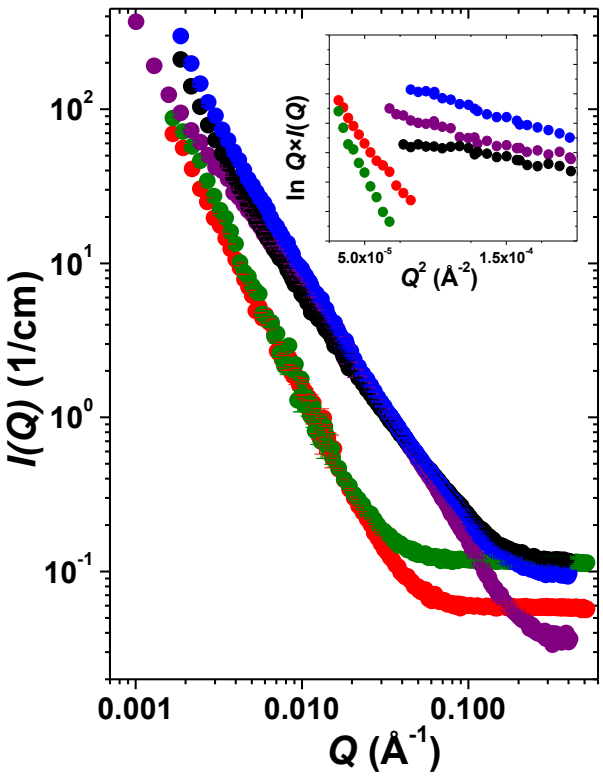

Figure 3.6: SANS scattering profiles *I(Q)* vs. *Q* for polysaccharide and mixed oligopeptide-polysaccharide networks: CA (chitosan + alginate), red; CAD (CA + chondroitin), green; P (KWK + EWE), purple; CAP (CA + P), black; CADP (CAD + P), blue. Guinier plots for rod-like particles, *lnQ*I(Q)* vs. Q^2, are shown in the inset, and the linearity in this region indicates the formation of elongated fibers in all systems. Color code on inset corresponds to the main figure. Statistical error bars correspond to one standard deviation and represent error in the scattering intensity estimation. Error bars are large at the instrument configuration overlap region but are smaller than the plotting symbols at low *Q*.

Since the scattering intensity profile *I*(*Q*) *vs. Q* reflects the mass and/or volume of the scattering assemblies, this points to the formation of denser, higher scattering aggregates for **P**, **CAP**, and **CADP** consistent with greater stiffness of these hydrogels observed in dynamic rheology experiments (see, Table 3.1, and also cf. Figure 3.1–Figure 3.5). One might expect that in addition to the density of the fibrous network, the morphology of the individual fiber and its cross-section also influences the material characteristics of bulk networks. Therefore, using a 2D dummy atom

modeling routine (*103*), we have restored the cross-sectional shapes of the fibers constituting the networks under study with the best fit of scattering data ($\chi^2 < 1.5$). The cross-sectional shapes represent average cross-sections within each sample type. We have also derived the associated pair-wise distance distribution functions of the cross-sections, $P_c(r)$. From the $P_c(r)$ function, the important dimensional parameters of the fiber cross-section were derived such as the maximum cross-sectional dimensions of the fiber, D_{max}, and the radius of gyration of the cross-section, R_c (Table 3.1).

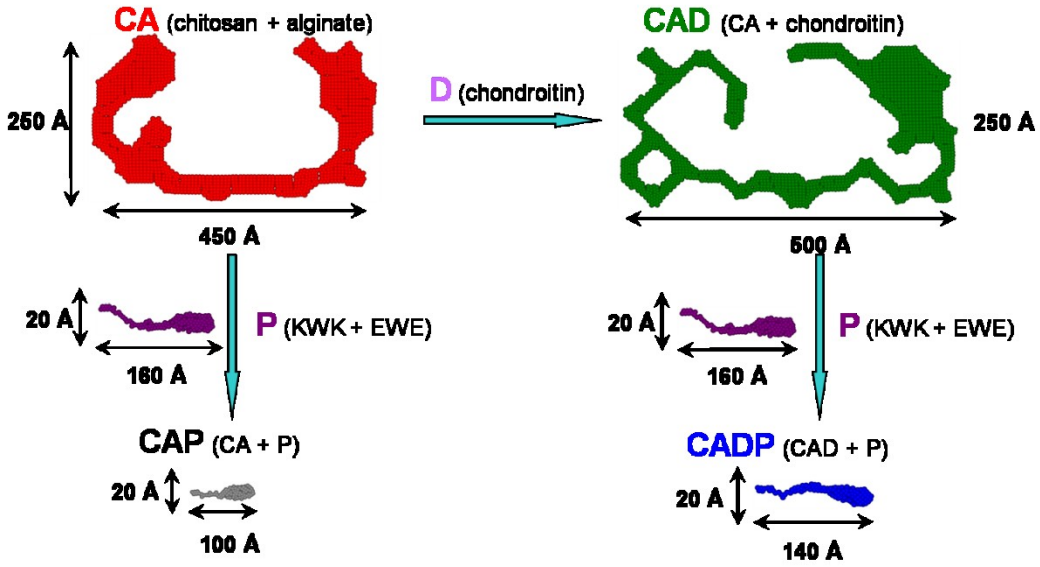

Figure 3.7: Pictorial description of the 2D shapes of a fiber cross-section in polysaccharide and composite oligopeptide-polysaccharide networks. The addition of chondroitin **D** to **CA** (chitosan + alginate, red) leads to much bigger and thicker fiber **CAD** (**CA** + chondroitin, green); while the addition of the peptides **P** (**KWK** + **EWE**, purple) to the above polysaccharide networks with the formation of **CAP** (**CA** + **P**, black) or **CADP** (**CAD** + **P**, blue) completely disrupts the structures of polysaccharides and results in the fibers with the cross-section very similar to the pure peptide network **P**.

It can be seen from the fiber cross-sections in Figure 3.7 that the addition of chondroitin (**D**) to the polysaccharide **CA** network leads to the incorporation of **D**

into the fiber structure. As a result, the average cross-section of the resulting fiber of **CAD** is bigger and thicker. As compared to **CA**, the maximum dimension of **CAD**, D_{max}, increased from 445 Å to 495 Å, and the radius of gyration of the cross-section R_c grew from ~153 Å to ~170Å (Table 3.1). Incorporation of **D** into the **CA** fiber structure is also evident from the changes observed in the $P_c(r)$ function of the cross-section (Figure 3.8(A)). Here, the addition of **D** results in a significant increase in contributions from the higher vector lengths scales ~400 Å. This is consistent with the formation of bigger and thicker fibers evident from the growth in D_{max} and R_c when **CA** is transformed to **CAD**. One might suggest that this increase in thickness is translated into the greater stiffness of the **CAD** network as compared to the **CA** network (G′ of **CAD** is 4-fold larger than G′ of **CA**; see Table 3.1, also cf. Figure 3.1 and Figure 3.2).

The individual fiber of the pure peptide hydrogel **P**, co-assembled from **KWK** and **EWE** peptide modules, has a much smaller average cross-section (Figure 3.7) with a $P_c(r)$ pattern characteristic of highly asymmetrical flattened shapes (Figure 3.8(B)). Accordingly, the D_{max} and R_c values of the **P** hydrogel are significantly lower as compared to **CA** and/or **CAD** networks (Table 3.1). However, despite smaller dimensional characteristics, the stiffness of the pure peptide hydrogel **P** is more than ~200-fold greater as compared to pure polysaccharide networks **CA** and **CAD** (Table 3.1, cf. Figure 3.1–Figure 3.3).

In this context, the cross-section dimensional parameters of the individual fiber are by no means the only determinants of the mechanical properties for the bulk fibrous networks. A definitive role is also played by the parameters characterizing

the network density, packing and compactness of the fiber, which reflects its rigidity. SANS analysis allows us to reliably determine the correlation length of the network L_c or its mesh size, which is an extremely sensitive measure of the network density and, thus, of its strength. Even a moderate difference in

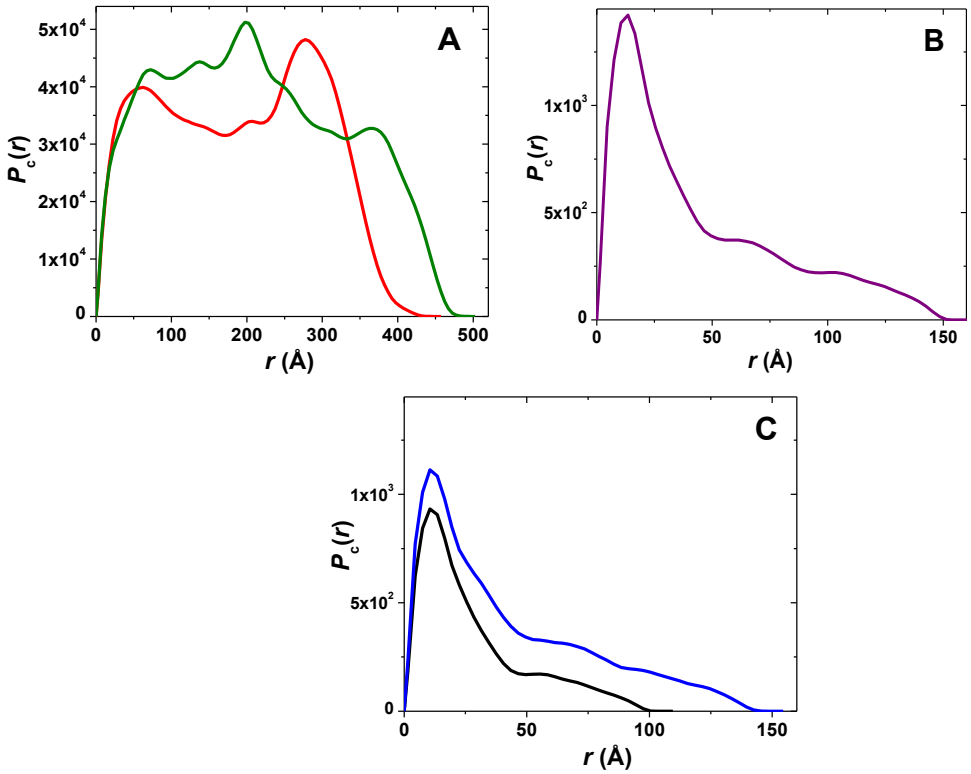

Figure 3.8: Changes in the pair-wise distance distribution functions $P_c(r)$ of the fiber cross-section observed during the formation of polysaccharide and composite oligopeptide-polysaccharide networks. (A) Transformation of the $P_c(r)$ for the CA (chitosan + alginate, red) network after the addition of chondroitin D resulting in the formation of the intricate CAD (CA + chondroitin, green) network. (B) $P_c(r)$ as function of the pure peptide hydrogel P (purple) characterizing the flattened cross-section of the individual fiber. (C) Cross-section $P_c(r)$ of the fibers assembled in the mixed hydrogels CAP (CA + P, black) and CADP (CAD + P, blue) after disruption of the fibers of CA and CAD.

the correlation length might have significant repercussions on the bulk material properties. For the materials described here, **P** is characterized by a more than 2-fold smaller correlation length L_c as compared to **CA** and/or **CAD** (Table 3.1). This large

difference in L_c results in a much denser, solid network, which explains the profound strengthening in the elastic modulus G' of the **P** hydrogel (Table 3.1, cf. Figure 3.1–Figure 3.3). Another factor contributing to bulk material properties is the mass-fractal dimension d, which describes the structure of the repetitive unit ("building brick") of the fiber and the packing of such "building bricks" within the fiber. Mass-fractal analysis shows that the pure polysaccharide networks, **CA** and **CAD,** are assembled from randomly-branched building bricks (d values from 2.7 to 3.0, Table 3.1). These materials are characterized by a much greater degree of swollenness as opposed to the Gaussian-coil building bricks ($d \sim 1.6$, Table 3.1) characteristic for the pure peptide hydrogel **P**. Evidently, the fibers of **P** are assembled from more tightly packed repetitive units than the **CA** and/or **CAD**, which may be why they are characterized by much greater elastic modulus values (Table 3.1). Based on the above analysis, when comparing such structurally dissimilar networks—pure polysaccharides *vs.* pure peptides—the correlation lengths of the networks as well as the packing and compactness of the fibers define the mechanical strength of the bulk material to a far greater degree than the dimensional characteristics of the individual fiber.

In the same vein, one could analyze the formation of the composite oligopeptide-polysaccharide networks **CAP** and/or **CADP**. As seen from Figure 3.7 and Figure 3.8(C), addition of the peptide component **P** (**KWK** and **EWE** modules) to the matured polysaccharide networks, results in complete disruption of the intricate structural characteristics of **CA** and **CAD**. 2D shapes of the average cross-sections (Figure 3.7) and $P_c(r)$ functions of **CAP** and **CADP** (Figure 3.8(C)) have a distinctive asymmetrical, flattened shape and are very similar to those observed for the pure

peptide hydrogel **P**. This observation confirms the above conclusion made on the basis of dynamic rheology data that during the co-assembly, whereby the charged peptide modules interact with the **CA** and/or **CAD** networks. Despite evident structural similarity of the fiber cross-sections of the **P**, **CAP**, and **CADP** networks, the correlation length L_c of the composite oligopeptide-polysaccharide hydrogels is significantly greater than in the case of the pure peptide hydrogel **P** (Table 3.1). Therefore, the mechanical strength of the composite oligopeptide-polysaccharide hydrogels is significantly lower as compared to the pure peptide network **P** (Table 3.1, Figure 3.3–Figure 3.5).

Table 3.1: Dimensional characteristics of the hydrogel networks and structural data of the individual fibers from SANS data analysis, and their elastic moduli from dynamic rheometry experiments.

Hydrogels	D_{max} **(Å)**	R_c **(Å)**	L_c **(Å)**	***d***	***B***	***G'*** **(Pa)**
CA (chitosan + alginate)	445	152.7	150	3.0 ± 0.2	5.2×10^{-4}	100
CAD (**CA** + chondroitin)	495	170.2	155	2.7 ± 0.1	3.7×10^{-4}	400
P (*L*-KWK + *L*-EWE)	160	40.6	60	1.6 ± 0.2	4.1×10^{-3}	90,000
CAP (**CA** + **P**)	100	25.7	98	1.7 ± 0.2	4.4×10^{-3}	10,000
CADP (**CAD** + **P**)	145	39.0	104	1.9 ± 0.2	4.0×10^{-3}	10,000

D_{max} is the max dimension of the fiber cross-section in Å; R_c is the radius of gyration of the cross-section of the individual fiber in Å; L_c is the correlation length reflecting the mesh size of the network; *d* is the mass-fractal dimension defining the repetitive unit of the fiber (its "building brick"); *B* is the mass-fractal power-law prefactor describing the dimensional characteristics of the repetitive unit; and *G'* is the elastic modulus of the networks in Pa.

To summarize, the observed high scattering intensity is indicative of the interaction between polysaccharides and/or peptides, resulting in the formation of the fibrous networks. Addition of the oligopeptides to the polysaccharide hydrogels

induces complete disruption of the initial polysaccharide fibrous networks. New oligopeptide-polysaccharide hydrogels are assembled and at the level of the individual fiber, such composite networks are structurally similar to the pure peptide hydrogel. Significantly greater mesh sizes of these composite networks leads to much less stiff material as compared to the pure peptide hydrogel. SANS analysis corroborates the suggestion made above on the basis of the rheology data that the weaker fibrous network of the composite oligopeptide-polysaccharide hydrogel is formed due to the complexation between peptide modules and sugar moieties, thus precluding the assembly of stronger, mutually reinforcing networks.

3.5 Conclusions

It is quite reasonable to expect that attempts to create biomaterials needed for human tissue engineering would be based on similar chemical composition of, *e.g.*, cartilage, tendons, or ligaments which are formed from proteins and polysaccharides (glycosaminoglycans). In the present chapter, we aimed to prepare composite hydrogels in which the fibrous peptide networks were combined with the fibers assembled from long, charged polysaccharide structures. In this way, our materials would mimic the chemical and/or structural composition of protein/polysaccharide composite-based human soft tissues. The pure polysaccharide networks (**CA** and **CAD**) were very weak materials with low elastic moduli, however, with significant resistance to deformation. Incorporation of the polysaccharides into the oligopeptide hydrogel also resulted in materials (**CAP** and **CADP**) with very high resistance to deformation (strain values from 20 % to 100 %), far less brittle compared to the pure peptide hydrogel **P**. However, the propensity of the oligopeptides to form complexes

with the polysaccharides may be responsible for the significant loss of stiffness of the composite material as compared to the pure peptide hydrogel. 2D shapes of the individual fiber cross-sections, changes in the dimensional characteristics of the fiber, and the mesh size of the network illustrate the aforementioned interaction between the peptides and sugars. These results also explain the weakening of the composite oligopeptide-polysaccharide material. Our results suggest a novel approach for creating highly deformation-resistant biomaterials. Ways to increase material strength for the purpose of human tissue engineering will be a subject of our continued efforts.

Chapter 4: Handedness Matters: Chirality in Biopolymer-Based Material Design

4.1 Introduction

In the human body, interactions between proteins and polysaccharides are extremely important and common. Proteins and polysaccharides can interact to form complex structures with various mechanical and structural properties. The extracellular matrix, for example, is an interlocking mesh of proteins and glycosaminoglycans (GAGs). It is well known that these proteins and polysaccharides are made from chiral components. In fact, proteins and polysaccharides are made from components with opposite chirality; proteins are made only from *L*-amino acids and most polysaccharides are made from *D*-sugars.

Recently, the mechanical and structural properties of gels formed from pairs of oppositely charged, self-repulsive undecapeptides were characterized and both *L*- and *D*- forms of the peptides were made (*49*). Both the *L*-gel (made from two *L*-peptide modules) and the *D*-gel (made from two *D*-peptide modules) were mechanically and structurally identical, while mixed chirality peptide gels were much weaker. This result suggested that peptide homochirality had a mechanical advantage. It is known that the natural amino acid/sugar (*L*-amino acids/*D*-sugars) combination confers molecular advantages. For example, *L*-enzymes recognize *L*-peptides and *D*-nucleic acids but not *D*-peptides and *L*-nucleic acids (*107, 108*). This phenomenon is known as chiral selectivity. What remains unclear is whether the (*L*-amino acids, *D*-sugars) combination also confers material advantages, such as mechanical properties.

Based on these differences in molecular recognition, we hypothesized that the introduction of a polysaccharide would disrupt the structural and mechanical degeneracy of the mirror-image peptide hydrogels due to polysaccharide chiral selectivity.

In order to study the mechanical and structural implications of interactions between proteins and polysaccharides, we focused on five systems: peptide hydrogels (*D* or *L*) and the *D*-saccharides; β-cyclodextrin (βCD), chondroitin (Chd), glycogen (Glyn) and hydroxypropyl cellulose (HPC). The peptide hydrogels, synthesized using either *L*- or *D*-amino acids, act as model systems for proteins in the extracellular matrix, creating mechanically rigid and complex networks. Each peptide module contains two tryptophans (Trp), which have been shown to interact weakly with sugar molecules (*109-111*). It has been reported that βCD, a cyclic oligosaccharide, interacts more strongly with *L*-Trp than *D*-Trp (*112*). From a biomaterials standpoint, our interest was in whether this selectivity could be seen with *D*-βCD and other saccharides in the context of gelation properties like mechanical stiffness and gelation kinetics. Saccharides with a range of properties were chosen to represent the different types present in the body. βCD was chosen because of its demonstrated chiral selectivity with Trp in solution and well-defined structure. Chondroitin was chosen for its charge and natural prevalence in cartilage. Glycogen was chosen for its branched design and ubiquitous presence in muscle tissue. HPC was chosen because it was linear, neutral and water soluble. In this way, effects of saccharide properties on chiral selectivity could also be studied.

In this work, the effects of chiral selectivity on the bulk mechanical and structural properties of biopolymer based materials were described using rheology and small-angle x-ray scattering (SAXS) respectively. This approach can provide insight on using chirality as another tool for tuning the properties of biopolymer-based biomaterials. In addition, it may give insight from a mechanical standpoint for why proteins and saccharides have opposite chirality in nature.

4.2 Materials and Methods

4.2.1 Materials

β cyclodextrin (1.14 kDa, Sigma-Aldrich), glycogen (100-1000 kDa, Sigma-Aldrich), bovine chondroitin sulfate sodium salt (~20 kDa, Pfaltz & Bauer) and hydroxypropyl cellulose (~80 kDa, Sigma-Aldrich) were used as purchased.

4.2.2 Peptide Synthesis and Preparation

Four peptides were engineered using the approach described in chapter 3. L^+ (K-peptide) and L^- (E-peptide) were made with *L*-amino acids and D^+ (K-peptide) and D^- (E-peptide) were made with *D*-amino acids. The purity and the molecular weight of each purified peptide were verified by reverse-phase analytical HPLC and mass spectrometry, respectively (see Appendix Figures A19-A26). The sequences were:

Positive modules ($\boldsymbol{L}^+$ or $\boldsymbol{D}^+$): acetyl-**K**-W-**K**-A-**K**-A-**K**-A-**K**-W-**K**-amide

Negative modules ($\boldsymbol{L}^-$ or $\boldsymbol{D}^-$): acetyl-**E**-W-**E**-A-**E**-A-**E**-A-**E**-W-**E**-amide

Each purified peptide sample was dissolved in ultrapure water and dialyzed at room temperature against water for 24 hours using a dialysis membrane with a molecular weight cutoff of 100-500 Da. The concentration of each peptide sample was determined on the basis of the UV absorption of the Trp residues in each peptide, using an extinction coefficient of 5690 $M^{-1}cm^{-1}$ at 280 nm (*101*).

4.2.3 Dynamic Rheometry Sample Preparation and Characterization

For peptide+Chd sample solutions, peptide concentrations were adjusted to 32 mM and E-peptides were mixed 1:1 with 20 mg/mL chondroitin in PBS buffer while K-peptides were mixed 1:1 with PBS buffer, to avoid electrostatic interactions between K-peptides and chondroitin before peptide mixing. For 4 mM peptide+βCD sample solutions, both E- and K-peptide concentrations were adjusted to 16 mM and mixed 1:1 with 4 mM βCD in PBS buffer. For 8 mM peptide+βCD sample solutions, both E- and K-peptide concentrations were adjusted to 32 mM and mixed 1:1 with 8 mM βCD in PBS buffer. For peptide+Glyn sample solutions, both E- and K-peptide concentrations were adjusted to 32mM and were mixed 1:1 with 10 mg/mL glycogen in PBS buffer. For 2 mM peptide+HPC sample solutions, both E- and K-peptide concentrations were adjusted to 8 mM and were mixed 1:1 with 1.25 mg/mL HPC in PBS buffer. For 8 mM peptide+HPC sample solutions, both E- and K-peptide concentrations were adjusted to 32 mM and were mixed 1:1 with 1.25 mg/mL HPC in PBS buffer. The ionic strengths of the samples were tuned to the conductivity of PBS buffer using a conductivity meter. Sample preparation procedures and measurements were performed at 25°C and the final pH for all samples was 7.4.

To make each gel, solutions of two oppositely charged, same chirality peptide modules containing saccharides were centrifuged separately for 10 min at 8,000 rpm. 200 μL of each K- and E-peptides with saccharides were mixed through a Y-shaped connector in the sealed cell of the rheometer, immediately followed by monitoring of the gelation process.

Dynamic rheological measurements were made using a sealed-cell NOVA rheometer (ATS REOLOGICA Instruments Inc., Sweden) equipped with a temperature-control unit, a custom-made humidifier and a 25-mm diameter cone-and-plate stainless steel geometry (4˚ cone angle). All experiments were conducted at 25˚C. The detailed description of the sequential rheological experiments can be found in Chapter 3. Briefly, time-sweep measurements were conducted at 0.2% strain amplitude and 1 rad/s angular frequency. Time-sweep measurements were immediately followed by frequency-sweep measurements, which were performed at 0.2% strain amplitude from 0.01 to 100 rad/s. Strain-sweep measurements were then performed with one integration cycle at 1 rad/s frequency, with a strain amplitude range from 0.1 % to 100 %.

4.2.4 SAXS Sample Preparation and Data Collection

Glyn+peptide, HPC+peptide and βCD+peptide solutions were prepared for SAXS as described for dynamic rheometery experiments. Gels were prepared for SAXS experiments as described previously (*49*). Briefly, 10-15 μL equal volumes of each peptide (10-15 μL) were centrifuged (20 sec at 500 RPM) into a cylindrical glass capillary (Charles Supper Co.) with a diameter of 1.0 mm and a wall thickness of 0.01

mm. Scattering data were collected at 0.5, 1.5, 3, 5, 7, 24, 48, and 72 hrs after mixing for Glyn+peptide, HPC+peptide and βCD+peptide samples.

Structures of the gels were investigated using the SAXS beamline 12ID-B of the Advanced Photon Sources (APS) at the Argonne National Laboratory. For every measurement, the monochromic X-ray beam (λ = 0.689 Å) with a size of 0.07 mm × 0.20 mm was adjusted to pass through the centers of the capillaries. In order to avoid detector saturation and radiation damage to the samples, the exposure time for all samples was set to 0.5 sec. The 2D detector Pilatus 2M (DECTRIS Ltd) was used to collect X-ray scattering intensities.

4.2.5 SAXS Data Analysis

The 2D scattering images were converted into 1D scattering profiles of $I(Q)$ vs. Q in the Q-range from 0.007 $Å^{-1}$ to 0.6 $Å^{-1}$ by means of azimuthal averaging after solid angle correction. Using the software package at the beamline 12ID-B, the resulting 1D profiles were normalized over the intensity of the transmitted X-ray beam. $I(Q)$ is the scattering intensity of X-rays, and Q is the scattering vector amplitude which is related to the X-ray wavelength λ and the scattering angle θ by

$$Q = \frac{4\pi}{\lambda} \sin\left(\frac{\theta}{2}\right) \qquad (4.1)$$

Solvent scattering subtraction (PBS) involved normalization based on the ratio of incident and transmitted X-ray photon counts to account for the slight differences in the thickness of different capillaries. Also additional background scattering correction was performed in accordance with the generally accepted published procedure (*76*).

The length of the fibers exceeded the upper detection limits of SAXS (~ 500Å) so we analyzed their scattering data in terms of the cross-sectional dimensions of the scattering particles. This was done by multiplying *I(Q)* values by *Q*, which essentially removes information about the length of the scattering particles (*81*).

A simulated annealing algorithm was used to restore the 2D cross sections for the hydrogels. We modeled the 2D cross sections of the hydrogel fibers using the algorithm in a purpose-written program that is described elsewhere (*103*). A flat grid of 20 X 20 close-packed dummy atoms was arranged, each 3 Å in diameter. This technique allows one to model pictorial cross section slices of the hydrogels showing the fibers and how they are connected in the fibrous network. The program calculated the pair distance distribution function, $P_c(r)$, for the model cross-section made of the dummy atoms. $P_c(r)$ is the distribution of distances between area elements in the cross-section, weighted by the scattering density at each radial distance, *r*. The optimization procedure is in general described elsewhere (*103,113*).

After optimization, the radius of gyration of the cross-section R_c (Å), the cross-section area S_c (Å) and the zero-angle scattering intensity $I_c(0)$, which is proportional to the mass per unit length of the fiber (in arbitrary units per Å), were determined from $P_c(r)$. The zero-th and the second moments of $P_c(r)$ provide $I_c(0)$ and R_c values, respectively. R_c is the contrast-weighted mean distance of all area elements from the center of scattering density.

The annealing program also outputs the average model cross-sections as atomic coordinate files in Protein Data Bank format so they can become images. 2D fiber cross-section solutions are unique and characterized by low Chi-squared values

(χ^2 ~ 0.3-0.5). χ^2 values were much lower for SAXS data here than for SANS data in Chapter 3 because there was some overlap in data collection using SANS. 2D network cross-sections (Figure 4.3) are pictorial representations of the networks and are not unique solutions. Based on these coordinates and the grid dimensions, the area of the cross-section, S_c, was calculated. Corrections for scaling and incoherent background were applied to the model scattering profile so it could be compared directly with experimental scattering data (*103*).

Persistence length analysis was performed using the IGOR 6.2/NIST NCNR Analysis Package. Persistence length, l_p, is the length along the cylinder over which the flexible cylinder can be considered a rigid rod. Therefore, l_p tells us about the stiffness of individual fibers. The model used in this analysis is a parameterization of simulations for a discrete representation of the Kratky and Porod worm-like chain model, applied in the pseudo continuous limit (*114*). Persistence length values given here are somewhat different from traditional values for the persistence lengths of polymer chains (where the fiber cross section must be smaller than the fiber persistence length). This is because our biopolymer fibers are self assembled by non-covalent bonding, while polymer chains are covalently bound. Our biopolymer fibers are made from stacks of unit assemblies which, because they are non-covalently bound, can be shifted with respect to each other. As a result, the fiber cross-sections may be larger than fiber persistence length values.

4.3 Results and Discussion

L/L+Glyn and *D/D*+Glyn gels gave very conclusive, consistent results in both rheological and structural testing showing that *L/L*+Glyn was stronger than

D/D+Glyn. Time sweep results show that *L/L*+Glyn gelled faster and was stiffer than *D/D*+Glyn (Figure 4.1). Using SAXS to examine the underlying fiber structure of the two gels, we observed that *L/L*+Glyn fibers were significantly smaller in average cross-section as seen in both Figure 4.2 and the S_c values in Table 4.1(*L/L*+Glyn was 576 Å^2 and *D/D*+Glyn was 792 Å^2). The l_p for *L/L*+Glyn was also larger than *D/D*+Glyn, indicating the individual fibers in *L/L*+Glyn were stiffer than *D/D*+Glyn. Looking at an average cross-section of the fibrous network (slice of ~500 Å x 500 Å) within the gels, it was apparent that *L/L*+Glyn networks were more closely packed, evidenced by the significantly lower correlation length when compared with *D/D*+Glyn networks (Table 4.1). Visually, the difference can be seen in Figure 4.3, where the *L/L*+Glyn network is distinctly more complex than *D/D*+Glyn, which also helps to explain the lower correlation length and higher persistence length. Taken together, the mechanical and structural results point to a stronger interaction between *L*-oligopeptides and glycogen, compared with *D*-oligopeptides and glycogen.

Table 4.1: Structural data from SAXS analysis. The zero angle scattering intensity of the cross-section, proportional to mass per unit of fiber length ($I_c(0)$), radius of gyration of the cross-section (R_c), cross-section area (S_c), correlation length (l_c) and persistence length (l_p) were analyzed for oligopeptide+saccharide samples.

Samples	$I_c(0)$	R_c (Å)	S_c (Å^2)	l_c (Å)	l_p (Å)
8 mM *L/L*+Glyn	1.46E+05	12.41	576	39.5	26.0
8 mM *D/D*+Glyn	2.80E+05	14.72	792	42.1	13.5
2 mM *L/L*+HPC	6.19E+05	17.08	1170	72.4	11.9
2 mM *D/D*+HPC	5.53E+05	17.34	1107	79.8	13.4
4 mM *L/L*+HPC	5.35E+05	17.33	1089	71.0	14.9
4 mM *D/D*+HPC	5.44E+05	17.01	1098	68.5	12.9
8 mM *L/L*+HPC	3.56E+05	15.70	891	75.9	13.3
8 mM *D/D*+HPC	4.66E+05	16.69	1017	65.2	9.5
4 mM *L/L*+βCD	2.08E+05	16.96	684	58.7	7.6
4 mM *D/D*+βCD	2.19E+05	17.02	702	38.0	7.8

Perhaps because HPC (~80 kDa) is a much smaller polysaccharide than glycogen (~500 kDa), using the same weight by volume ratio of HPC did not significantly split the mechanical degeneracy of *LL* and *DD* (*L/L*+HPC: 100 kPa and *D/D*+HPC: 120 kPa, a difference of less than 10%). For this reason, we decreased the oligopeptide concentration (from 8 mM to 2 mM) in an effort to alter the ratio of HPC to peptide and possibly slow down gelation. At a 2 mM oligopeptide concentration, we did observe a difference, where *L/L*+HPC was significantly stiffer than *D/D*+HPC (*L/L*+HPC was 11.5 kPa and *D/D*+HPC was 8 kPa, Figure 4.1).

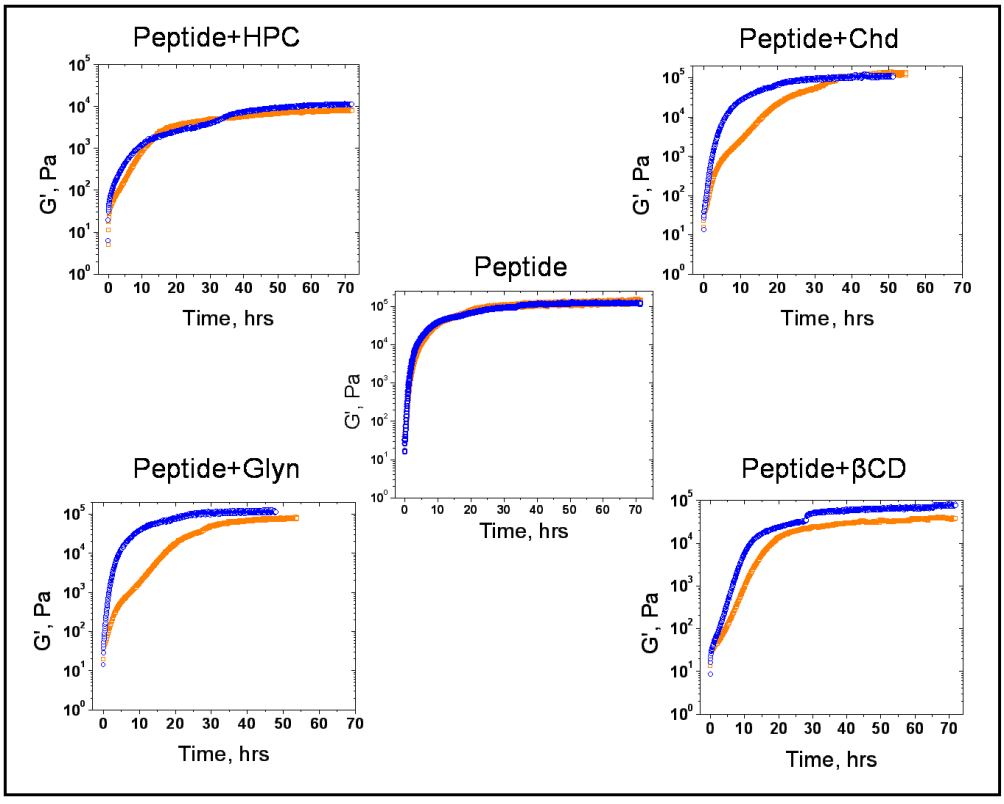

Figure 4.1: Rheological time sweep plots for each *L/L* and *D/D* pair: Peptide+HPC is 2 mM peptide + 0.125% w/v HPC; Peptide+Chd is 8 mM peptide + 1% w/v chondroitin; Peptide is 8 mM peptide; Peptide+Glyn is 8 mM peptide + 1% w/v glycogen; Peptide+βCD is 4 mM peptide + 4 mM βCD. Blue represents *L/L* samples and orange represents *D/D* samples.

To understand this result from a structural standpoint, we examined oligopeptide+HPC gels at three different concentrations (of each peptide): 8 mM, 4 mM and 2 mM, while keeping the HPC concentration the same (0.125% w/v). From the $P_c(r)$ plots (Figure 4.2), there was a decrease in the max $P_c(r)$ values for both *L/L*+HPC and *D/D*+HPC as the oligopeptide concentration increased, which may be due to the relative decrease in HPC concentration which has higher x-ray contrast. The decrease in area was much more significant for *L/L*+HPC as oligopeptide concentration increased, which likely indicates a greater incorporation of HPC into the *L/L* network, since free HPC scatters more than free peptides.

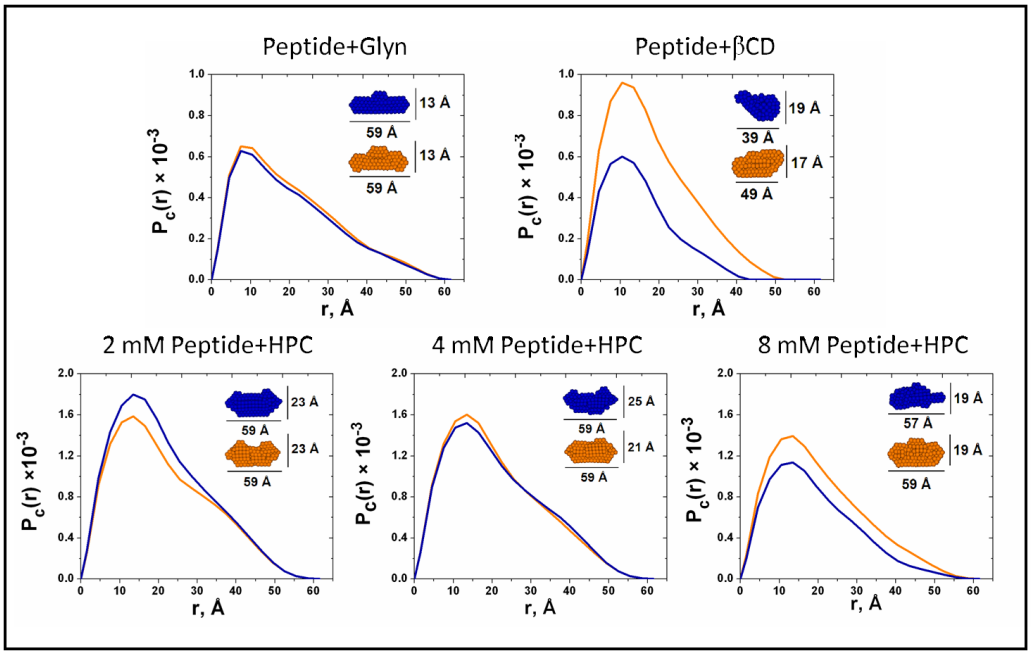

Figure 4.2: $P_c(r)$ plots with fiber cross-section images for each *L/L* and *D/D* pair. Blue represents *L/L* samples and orange represents *D/D* samples. HPC concentration for all peptide+HPC samples was 0.125% w/v.

At the 8 mM oligopeptide concentration, *L/L*+HPC fiber network had a larger correlation length than *D/D*+HPC, but *D/D*+HPC fiber cross-sections were much larger than *L/L*+HPC fiber cross-sections (Table 4.1). These properties seem to offset

each other, giving materials with very similar mechanical properties. What is apparent here from SAXS analysis is that HPC is being incorporated very differently by *L/L* and *D/D*, solidifying the idea that chiral selectivity does occur at the macromolecular level. At the 2 mM oligopeptide concentration, cross-section size and fiber stiffness were very similar in both *L/L*+HPC and *D/D*+HPC, but the *L/L*+HPC correlation length was smaller than the *D/D*+HPC correlation length. This means the fibers of *L/L*+HPC are more closely packed, which is why *L/L*+HPC is a stiffer material than *D/D*+HPC at 2 mM. Using two-phase analysis, we will to try to further understand these concentration dependent network properties. Two-phase analysis is a method which allows for each component to be visualized within the structure, meaning that saccharides and oligopeptides could be seen as separate components. This is possible because oligopeptides and saccharides have different x-ray contrasts.

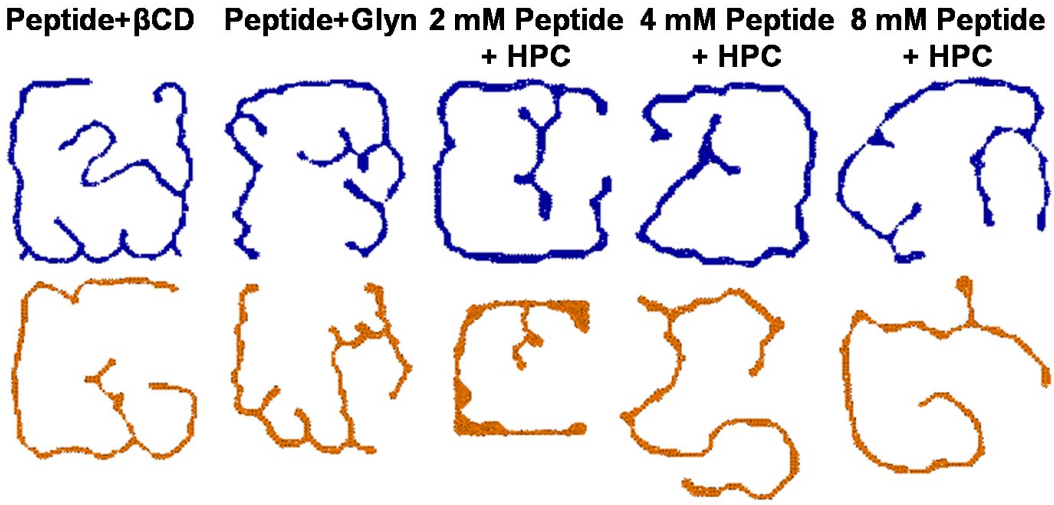

Figure 4.3: Cross-sections of the hydrogel fibrous networks (slices ~500 Å x 500 Å) for each *L/L* and *D/D* pair. Blue represents *L/L* samples and orange represents *D/D* samples.

Mechanical strength results for βCD were quite similar to those for HPC. At an 8 mM oligopeptide concentration, the gelation kinetics and plateau G' values for *L/L*+βCD and *D/D*+βCD were very similar. As a result, we decreased the concentration of oligopeptide to 4 mM and we observed that *L/L*+βCD gelled faster and was stiffer than *D/D*+βCD. Unfortunately, SAXS data was only collected for 8 mM oligopeptides with βCD. Structural data was in good agreement with mechanical results, mainly that both fiber and network structural properties were very similar. One exception was the difference between *L/L*+βCD and *D/D*+βCD correlation lengths, which was significant. This difference may have been due to differences in *L*-Trp interactions with βCD and *D*-Trp interactions with βCD, which have been seen by others on the molecular level (*112*). Though this difference is significant, it may not have affected mechanical properties because all other structural properties were similar. SAXS measurements of βCD with lower concentration oligopeptides, combined with two-phase analysis will likely elucidate this result.

For the final polysaccharide, chondroitin, only mechanical results have been collected. Much like glycogen, *L/L*+Chd and *D/D*+Chd had very different mechanical properties at an 8 mM oligopeptide concentration (Figure 4.1). Though the final stiffness of the two gels was similar, the gelation kinetics were significantly different. *L/L*+Chd gelation was much faster than *D/D*+Chd gelation. Since chondroitin is a charged polysaccharide, it adds another level of complexity (electrostatic interactions) to the oligopeptide-saccharide interactions because the oligopeptides are also charged. A separate in-depth study will be performed in a separate work to understand these interactions.

4.4 Conclusions

In this work, we studied the mechanical and structural properties of *L/L* and *D/D* oligopeptide hydrogels doped with four different *D*-saccharide types. Each polysaccharide type was able to split the mechanical degeneracy of *L/L* and *D/D* gels, though often not at all oligopeptide concentrations. In all cases where splitting occurred, *L/L* gels gelled faster and/or were stiffer than *D/D* gels. This provides a mechanical motivation for the biohomochirality combination to be (*L*-amino acids, *D*-sugars) instead of the alternate combination (*D*-amino acids, *D*-sugars). Clearly, stronger interactions occur between *L*-oligopeptides and *D*-saccharides, regardless of saccharide size, shape or charge. Structural analysis corroborated these findings using a combination of techniques to examine the gels at the level of the fiber and the level of the network. Further structural studies will help to further clarify some of the results. These results have implications for future composite oligopeptide-polysaccharide design considerations.

Chapter 5: Enhancing Biocompatibility in *D*-Oligopeptide Hydrogels by Negative Charges

5.1 Abstract

Oligopeptide hydrogels are emerging as useful matrices for cell culture with commercial products on the market, but *L*-oligopeptides are labile to proteases. An obvious solution is to create *D*-oligopeptide hydrogels, which lack enzymatic recognition. However, *D*-oligopeptide matrices do not support cell growth as well as *L*-oligopeptide matrices. In addition to chiral interactions, many cellular activities are strongly governed by charge-charge interactions. In this work the effects of chirality *and* charge on human mesenchymal stem cell (hMSC) behavior were studied using hydrogels assembled from oppositely charged oligopeptides. It was found that negative charges significantly improved hMSC attachment and proliferation in *D*-oligopeptide gels but had little effect on their interactions with *L*-oligopeptide gels. This result points to the possibility of using charge and other factors to engineer biomaterials whose chirality is distinct from that of natural biomaterials, but whose performance is close to that of natural biomaterials.

5.2 Introduction

Biohomochirality is recognized as a defining feature of life on earth. It is well known that biomacromolecules are homochiral, where proteins contain exclusively *L*-amino acids, and nucleic acids and most polysaccharides contain exclusively *D*-sugars. While the biochemical aspect of homochirality has been explored

extensively(*115-118*), its material aspect has been seldom explored. In a previous work, we investigated how chirality affects the mechanical and structural properties of oligopeptide hydrogels (*49*). In this work, we explored how chirality impacts hydrogel-cell interactions and how such interactions are modulated by the charge status of the hydrogel.

Hydrogels are viscoelastic materials with natural (e.g., the extracellular matrix) and manmade (e.g., contact lenses) examples. As a result of the homochirality of its constitutive biopolymers, natural hydrogels are also homochiral. For example, the extracellular matrix (ECM) is a chiral material made of homochiral *L*-proteins and homochiral *D*-polysaccharides. Both *L*-protein (e.g., MatriGel^{TM}) and *L*-oligopeptide (e.g., PuraMatrix^{TM}) hydrogels have been used to mimic the ECM for cell culture applications. Considering that the ECM has a profound impact on cell growth (*119*) and differentiation (*120*), the question of how ECM chirality affects cell behavior has significant implications for biology and bioengineering. In this work, oligopeptide hydrogels of different chirality makeups (homochiral, heterochiral and racemic) were used as ECM mimetics to grow cells. The impact of chirality on cell attachment and proliferation was investigated.

In addition to chiral interactions, many cellular activities are strongly governed by charge-charge interactions. Examples include cell communication and ion transport across the cell membrane. Regarding material-cell interactions, it has been found that both the type and the material charge density affect cell behaviors (*121-124*). Dadsetan et al. found that chondrocytes proliferated more on oligo(poly(ethylene glycol) fumarate) modified with negatively charged monomers

than positively charged monomers and that the percentage of monomer modification also affected cell behavior (*122*). In fact, material surface charge can be used to modify cell behavior (*125-127*). Keselowsky et al. found that on positively charged surfaces, osteoblasts up-regulated osteoblast-specific gene expression, alkaline phosphatase enzymatic activity, and matrix mineralization compared with negatively charged surfaces (*127*). Based on these previous studies, we hypothesized that it might be possible to exploit charge to modulate chiral effects in hydrogel-cell interactions. If proven true, then the combination of chirality and charge could be a powerful tool to guide cell behavior using oligopeptide hydrogels.

In contrast to other chirality studies in which thin films were used (*128,129*), we used soft hydrogels which more closely resemble the ECM. The hydrogels used in this study were assembled from self-repulsive but mutually attractive oligopeptide modules (*97*). Gelation requires at least two oppositely charged modules. This *co*-assembling approach allowed us to systematically explore various chirality-charge combinations, some of which are not available to hydrogels based on the *self*-assembly of a single oligopeptide.

In this study, human mesenchymal stem cells (hMSCs) were used because they are extremely attractive candidates for cellular therapy. MSCs have many attributes including ease of isolation, high expansion potential and genetic stability (*130*). Further, MSCs can be used allogeneically, an important clinical advantage (*131*). Understanding how hMSCs respond to different environments will facilitate the engineering of biomaterials with the appropriate properties for cell attachment and proliferation. hMSC attachment was investigated using a live/dead assay after one

day of cell incubation. hMSC proliferation was observed with a WST-1 assay 1, 3 and 7 days after cell seeding (*132*).

5.3 Materials and Methods

5.3.1 Chemicals

Fmoc-protected amino acids, N-Hydroxybenzotriazole (HOBt) and O-Benzotriazole-N,N,N',N'-tetramethyl-uronium-hexafluoro-phosphate (HBTU) were purchased from Aapptec and used as received. Rink amide MBHA resin was purchased from Chem Impex. Dimethylformamide (DMF) was purchased from Macron. Acetic anhydride and trifluoroacetic acid (TFA) were purchased from Alfa Aesar. Piperidine, N,N-Diisopropylethylamine (DIEA), MeOH, triisopropylsilane (TIPS), 3-(trimethylsilyl)propionic-*2*,*2*,*3*,*3*-d_4 acid, sodium salt (TSP) and diethyl ether were purchased from Sigma-Aldrich. WST-1 kit was purchased from Takara. Live/dead assay kit was purchased from Invitrogen. All components for hMSC basal growth media were also purchased from Invitrogen. hMSCs were purchased from Lonza.

5.3.2 Oligopeptide Design and Synthesis

Four oligopeptides were designed using the approach described in chapter 3, in which oppositely charged oligopeptide modules interact electrostatically, co-assemble and form a hydrogel. Detailed synthesis and purification procedures for these oligopeptides are described in Chapter 3 as well. Briefly, two positive sequences ($\boldsymbol{L}^+$ and $\boldsymbol{D}^+$) were made with alternating neutral (W and A) and positively charged (K) amino acids. The two oligopeptides were chiral opposites, made from

either all *L*-amino acids or all *D*-amino acids. The two negative sequences ($\boldsymbol{L}^-$ and $\boldsymbol{D}^-$) were made with alternating neutral (W and A) and negatively charged (E) amino acids. The oligopeptide sequences of these positively and negatively charged modules are given below:

Positive modules ($\boldsymbol{L}^+$ or $\boldsymbol{D}^+$): acetyl-K-W-K-A-K-A-K-A-K-W-K-amide

Negative modules ($\boldsymbol{L}^-$ or $\boldsymbol{D}^-$): acetyl-E-W-E-A-E-A-E-A-E-W-E-amide

Since these oligopeptide solutions were used for cell culture purposes, they were sterile filtered directly prior to gelation. The pH of each oligopeptide solution was 7.4.

5.3.3 Hydrogel Preparation

Our hydrogels are formed by mixing solutions of oppositely charged oligopeptide modules. In each hydrogel, the total oligopeptide concentration was 5 mM. All gels were made 24 hours before cell seeding. In total, 9 gel types were made under sterile conditions at 25°C (see Appendix, Figure A27).

To investigate chirality, neutral homochiral, heterochiral and racemic hydrogels were prepared. The neutral homochiral $(LL)^0$ gel was made by mixing equal volumes of 5 mM $\boldsymbol{L}^+$ with 5 mM $\boldsymbol{L}^-$. The neutral homochiral $(DD)^0$ gel was made by mixing equal volumes of 5 mM $\boldsymbol{D}^+$ with 5 mM $\boldsymbol{D}^-$. Neutral heterochiral $(LD)^0$ and $(DL)^0$ gels were made by 1:1 mixing of 5 mM $\boldsymbol{L}^+$ with 5 mM $\boldsymbol{D}^-$ and 1:1 mixing of 5 mM $\boldsymbol{D}^+$ with 5 mM $\boldsymbol{L}^-$, respectively. The neutral racemic hydrogel, $(LLDD)^0$, was made by mixing equal volumes of all 4 types of 5 mM oligopeptide

solutions ($\boldsymbol{L}^+$, $\boldsymbol{D}^+$, $\boldsymbol{L}^-$ and $\boldsymbol{D}^-$, each with a 1.25 mM final concentration in the hydrogel).

To investigate charge-chirality interplay, charged homochiral gels were prepared by varying the positive to negative oligopeptide ratio in the hydrogel while keeping the total oligopeptide concentration at 5 mM. Specifically, positively charged $(LL)^+$ and $(DD)^+$ gels were made by mixing equal volumes of 6 mM $\boldsymbol{L}^+$ or $\boldsymbol{D}^+$ with 4 mM $\boldsymbol{L}^-$ or $\boldsymbol{D}^-$, resulting in 1 mM of excess of positively charged oligopeptide in the hydrogel. Negatively charged $(LL)^-$ and $(DD)^-$ gels were made by mixing equal volumes of 4 mM $\boldsymbol{L}^+$ or $\boldsymbol{D}^+$ with 6 mM $\boldsymbol{L}^-$ or $\boldsymbol{D}^-$, resulting in 1 mM of excess of negatively charged oligopeptide in the hydrogel.

5.3.4 Nuclear Magnetic Resonance (NMR) Measurements

Individual oligopeptide solutions were pre-equilibrated at room temperature and diluted to appropriate concentrations in PBS, as described in the gel preparation section. $(LL)^+$, $(LL)^0$ and $(LL)^-$ gels were loaded into NMR tubes by quickly mixing equal volumes of each $\boldsymbol{L}^+$ and $\boldsymbol{L}^-$ solution together in a 1.5 mL plastic centrifuge tube and transferring the mixture to a 3-mm NMR tube using a long glass disposable pipette. Gels were allowed to mature for 24 hours at 25˚C and then both gels and solutions were contained in 3-mm NMR tubes (inner tubes). Each 3-mm inner tube was placed one at a time in the same 5-mm NMR outer tube containing 100% D_2O to provide the deuterium lock signal. With this setup, solutions and gels did not come in contact with D_2O.

NMR experiments were carried out on a Varian 400-MR spectrometer equipped with a triple resonance indirect detection probe. The temperature of the

NMR spectrometer probe was preset to 25˚C. ^{1}H spectra were used to examine the presence of free oligopeptide in each gel after 24 hours. Due to the very short transverse relaxation time (T_2) of gelled oligopeptides, only free oligopeptides can be detected by NMR spectroscopy (*133*). To compare the signal intensities from different 1D ^{1}H spectra, the same calibrated 90˚ pulse and the same receiver gain were used in all cases. All samples contained an external TSP standard in the outer D_2O tube in order to calibrate ^{1}H peak height and chemical shift. The number of averages for each ^{1}H spectrum was 16.

5.3.5 Cell Culture

hMSCs were cultured in high glucose Dulbecco's modified eagle medium (DMEM) supplemented with 10% FBS, 1% penicillin/streptomycin (100 U/mL), 1% nonessential amino acids (0.1 mM), 2% *L*-glutamine (4 mM) and incubated at 37°C, 5% CO_2. The medium was changed every two days. The cells were detached from flasks with PBS containing 0.25% w/v Trypsin-EDTA, were centrifuged and then resuspended in DMEM for re-plating on various hydrogels and tissue culture polystyrene (TCPS) plates.

5.3.6 Cell Attachment

hMSCs (passage 5 or 6) were seeded onto the surfaces of the hydrogels in a 96-well plate at a density of 1×10^{5} cells/mL in the culture medium and the cells were incubated for one day at 37˚C. To assess cell attachment one day after seeding, a live/dead assay was used. Cells were washed with PBS and incubated in PBS containing calcein acetoxymethyl ester (calcein-AM) and ethidium homodimer-1 for

30 minutes. Cells were washed again and incubated in PBS containing 4',6-diamidino-2-phenylindole (DAPI) for 10 minutes. hMSCs were then visualized by spinning disk microscope (SDM, Olympus IX81) at excitation wavelengths of 358 nm, 488 nm and 532 nm. DAPI was used to locate and focus on the cells within the gel, in an effort to minimize photobleaching of calcein-AM and ethidium homodimer-1. Cells cultured on a tissue culture polystyrene 96-well plate without hydrogel (TCPS) and the nine hydrogel types without cells were used as positive and negative controls respectively. Three wells were made per hydrogel type, six images were taken per well, and the assay was performed in triplicate, so a total of 54 images were taken per hydrogel type. Cells were counted using NIH ImageJ software (*73*). Relative attachment was calculated by normalizing the average number of experimental live cells per image to the average number of TCPS control live cells per image.

To study the effect of single oligopeptides on hMSC attachment, 50 μL of 2 mM oligopeptide in PBS was added to each well. Then, 50 μL of media containing 2×10^5 cells/mL was added to each well, making the final total concentration of oligopeptide 1 mM. The cells were then incubated for one day at 37˚C. A live/dead assay was also used to assess cell attachment. Cells grown in normal media on TCPS and 1 mM oligopeptide on TCPS without cells were used as positive and negative controls respectively.

5.3.7 Cell Proliferation

hMSCs (passage 5 or 6) were seeded onto the surface of the hydrogels in a 96-well plate at a density of 7×10^4 cells/mL. The medium was exchanged every two

days. Cells cultured on a 96-well plate without hydrogel (TCPS) and hydrogel without cells were used as positive and negative controls respectively. At different time points (day 1, day 3 and day 7), the proliferation of viable cells was assessed by the WST-1 assay. This assay is based on the cleavage of the tetrazolium salt WST-1 to formazan by cellular mitochondrial dehydrogenases present in viable cells.[20] Absorption by formazan at 450 nm was used to measure proliferation. Absorbance from negative controls at 450 nm was subtracted from all experimental results. The proliferation results were then expressed as a percentage of the absorbance of the positive control.

To study the effect of single oligopeptides on hMSC proliferation, 50 μL of 2 mM oligopeptide in PBS was added to each well. Then, 50 μL of media containing 2×10^5 cells/mL was added to each well, making the final concentration of the oligopeptide 1 mM. Medium containing 1 mM oligopeptide was changed every two days. Cell proliferation was still assessed using the WST-1 assay. Cells grown in normal media on TCPS and 1 mM oligopeptide on TCPS without cells were used as positive and negative controls respectively.

5.4 Results and Discussion

5.4.1 Experimental Design

To investigate how chirality and charge of hydrogels affect hMSC behavior, two mirror-image positively charged oligopeptide modules, $\boldsymbol{L}^+$ and $\boldsymbol{D}^+$, were made; also made were two mirror-image negatively charged oligopeptide modules, $\boldsymbol{L}^-$ and $\boldsymbol{D}^-$. Hydrogels were assembled by mixing oppositely charged oligopeptide modules

in PBS. Note that although all oligopeptide modules are homochiral and charged, different combinations of oppositely charged oligopeptides result in hydrogels of different chirality (homochiral, heterochiral or racemic) and charge (positive, neutral or negative) statuses. This is the advantage afforded by the co-assembly approach to hydrogelation.

To investigate the effect of hydrogel chirality on hMSC behavior, five neutral hydrogels, including homochiral, heterochiral and racemic types, were made. The two homochiral gels, $(LL)^0$ and $(DD)^0$, were mirror images of each other. So were the two heterochiral gels, $(LD)^0$ and $(DL)^0$. The racemic hydrogel, $(LLDD)^0$, was its own mirror image.

To investigate the interplay of charge and chirality on hMSC behavior, six homochiral gels of different charge statuses were made. The six hydrogels were comprised of three mirror-image pairs: $(LL)^+$ and $(DD)^+$, $(LL)^0$ and $(DD)^0$, and $(LL)^-$ and $(DD)^-$.

In total, 9 hydrogels of different chirality and charge statuses were assembled from 4 homochiral charged oligopeptides. Figure 5.1 lists all 4 parent oligopeptides, the resulting 9 hydrogels and their mirror image relationships.

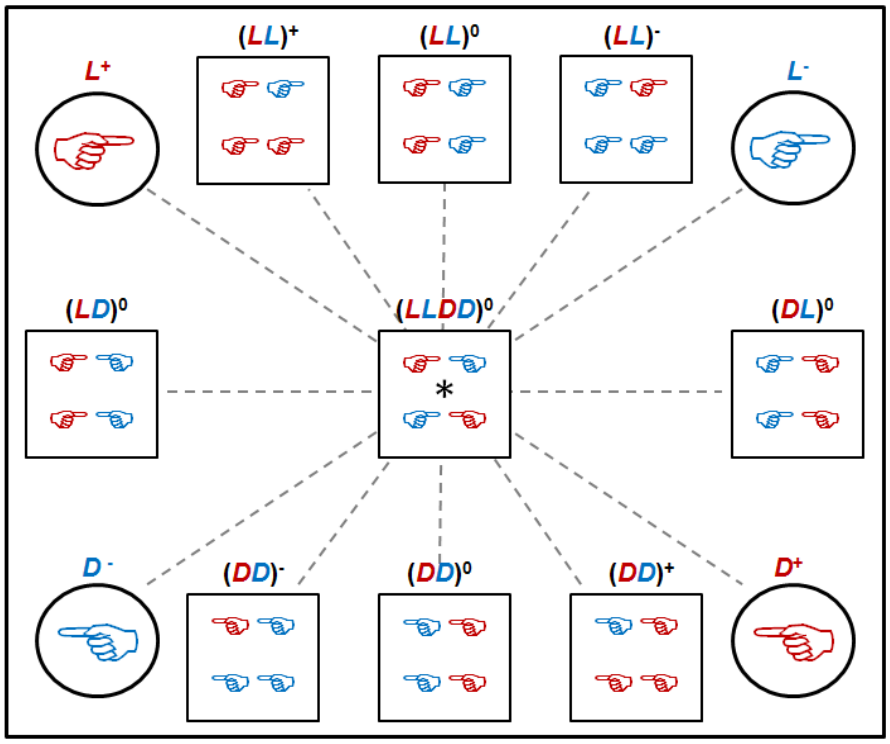

Figure 5.1. Pictorial description of the 4 parent oligopeptides and 9 hydrogels. The dashed lines connect mirror images which all run through $(LLDD)^0$, which is its own mirror image. Red hands represent positively charged oligopeptides and blue hands represent negatively charged oligopeptides. Circles represent parent oligopeptide solutions. Squares represent the hydrogels. The asterisk represents the center that all dashed mirror lines run through.

5.4.2 Effect of Oligopeptide Chirality and Charge on hMSC Attachment and Proliferation

It is important to separate the impact of a hydrogel from the impact of its constitutive oligopeptides. For this purpose, the impact of the four parent oligopeptides on hMSC behavior was assessed. The results are presented in Figure 5.2. All four oligopeptides had 5-10% lower cell attachment and 15-20% lower proliferation in comparison to the control (TCPS). However, there is no statistically significant difference among the four oligopeptides ($p > 0.01$, Appendix Table A2). Based on this result, any observed differences in hydrogel-cell interactions among the

nine hydrogels is caused by differences in hydrogels, not differences in constitutive peptides.

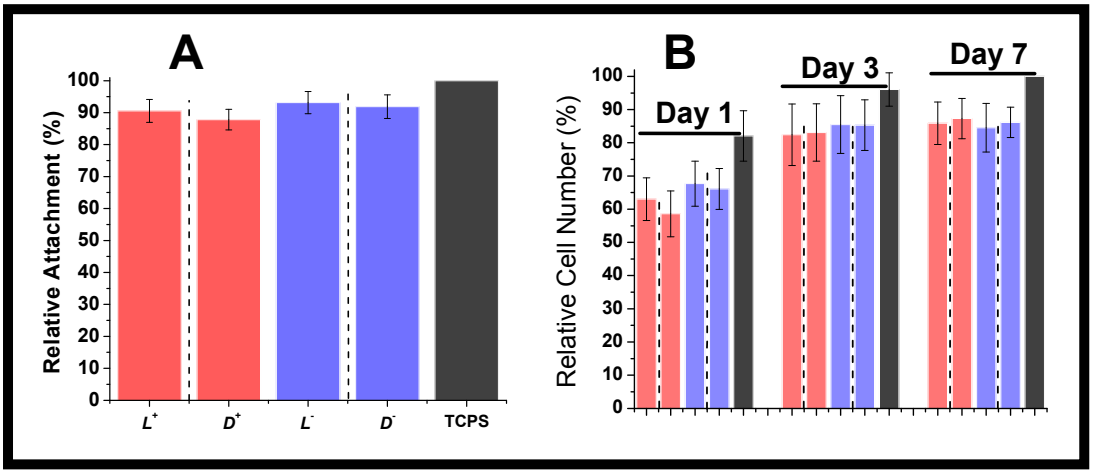

Figure 5.2. (A) Relative hMSC attachment to TCPS in the presence of single oligopeptides 1 day after cell seeding. (B) hMSC cell number percentage on TCPS in the presence of single oligopeptides at 1, 3 and 7 days after seeding. Bar order and colors in (B) correspond to the same order and colors in (A). Adjacent bars separated by dashed lines are a pair of mirror images. For (A), results were normalized to TCPS. For (B), results were normalized to TCPS day 7. For both graphs, errors are expressed as the standard error of the mean (SEM).

5.4.3 Chirality Effects on hMSC Attachment and Proliferation

Compared to TCPS, all five neutral gels had 70-80% lower hMSC attachment and 40-60% lower hMSC proliferation (Figure 5.3). Considering these oligopeptides do not contain any known cell adhesion motif, this result is not unexpected. Among the five neutral hydrogels, the homochiral $(LL)^0$ gel had the highest hMSC attachment while the racemic $(LLDD)^0$ gel had the lowest hMSC attachment. The other three gels, $(LD)^0$, $(DL)^0$ and $(DD)^0$ gel, showed no statistically significant difference in cell attachment.

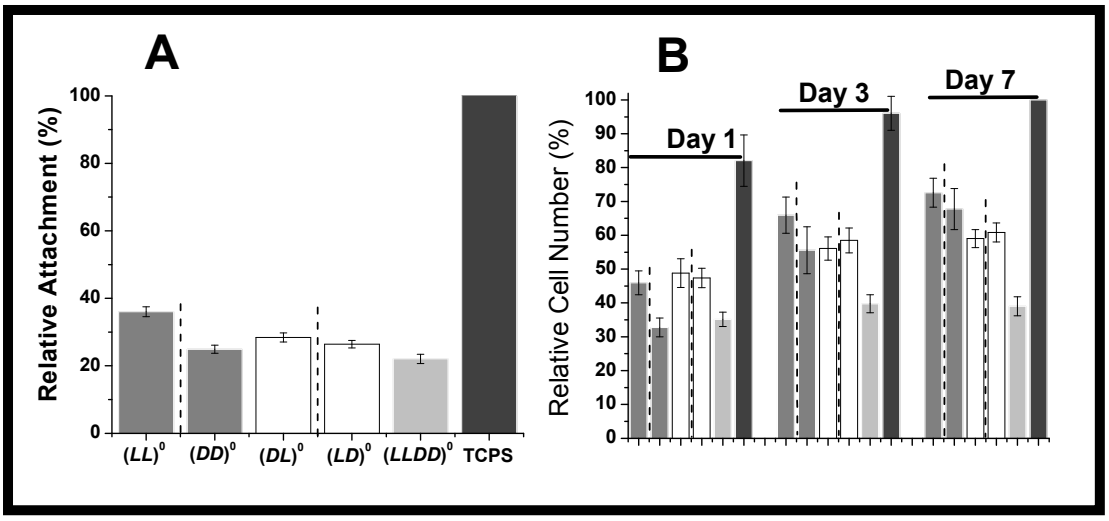

Figure 5.3. (A) Relative hMSC attachment to neutral homochiral and heterochiral gels at 1 day after cell seeding. (B) hMSC cell number percentage on neutral homochiral and heterochiral gels at 1, 3 and 7 days after seeding. Bar order and colors in (B) correspond to the same order and colors in (A). Adjacent bars separated by dashed lines are a pair of mirror images. For (A), results were normalized to TCPS. For (B), results were normalized to TCPS day 7. For both graphs, errors are expressed as the standard error of the mean (SEM).

Clear differences in hMSC appearance and survival can be seen in Figure 5.4. Here, cells on $(LL)^0$ gels appear blurry. The cells are situated at different focal planes, which suggest that they have penetrated into the gel matrix. None of the other gel images appear blurry, indicating that the cells stay on the surface of these gels. It is interesting that such penetration is unique to the gel whose chirality matches the chirality of the proteins on the cell surface. Such chirality matching is likely the reason that the $(LL)^0$ gel has better cell attachment and proliferation than the other gels. The question is whether chirality mismatch can be compensated by other factors, such as charge.

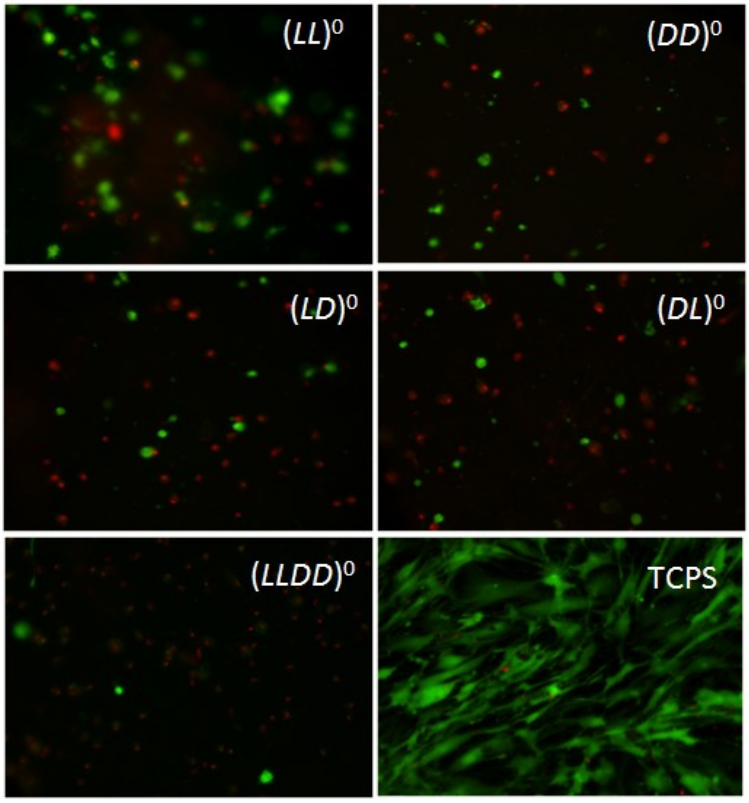

Figure 5.4. Representative live/dead images for neutral gels and TCPS control at 1 day after cell seeding. Live hMSCs are green and dead hMSCs are red. Cell size is much larger and image clarity is much cloudier for $(LL)^0$ images when compared with $(DD)^0$ and heterochiral images. These images indicate cell sinking into *LL* gels, but not into gels containing *D*-oligopeptide.

After initial attachment, hMSC proliferation was assessed on days 1, 3 and 7. All five gels supported hMSC proliferation during the seven-day period. However, the two homochiral gels, $(LL)^0$ and $(DD)^0$, had the largest increase in proliferation. On day 1, $(LL)^0$, $(DL)^0$ and $(LD)^0$ gels supported statistically the same amount of hMSC proliferation, while $(DD)^0$ and $(LLDD)^0$ gels supported significantly less hMSC proliferation. By day 7, $(LL)^0$ and $(DD)^0$ gels had the highest level of hMSC proliferation while $(LLDD)^0$ supported the lowest amount of hMSC proliferation. This result suggests that homochiral oligopeptide gels, both *L* and *D*, have higher potential

for hMSC proliferation than heterochiral oligopeptide gels, which in turn have higher potential than racemic oligopeptide gels for hMSC proliferation.

Considering that $(DD)^0$ has the "wrong" homochirality, it is not surprising that it does not support cell attachment and proliferation as well as $(LL)^0$. However, in spite of its initial much lower level of hMSC attachment and proliferation, hMSC proliferation on $(DD)^0$ eventually almost catches up with hMSC proliferation on $(LL)^0$. Among the five gels, $(DD)^0$ would be the most protease resistant. $(DD)^0$ also has the same mechanical and structural properties as $(LL)^0$ (*49*). Hence $(DD)^0$ is the most promising replacement of $(LL)^0$. With this in mind, we decided to investigate whether charge could make up the chiral disadvantage of the *D*-homochiral gel in hMSC attachment and proliferation.

5.4.4 Combined Charge and Chirality Effects on hMSC Attachment and Proliferation

Charged homochiral hydrogels were made by mixing the positively and negatively charged modules with one module in excess. Specifically, $(LL)^+$ has 1 mM excess of $\boldsymbol{L}^+$ while $(LL)^-$ has 1 mM excess of $\boldsymbol{L}^-$. $(DD)^+$ has 1 mM excess of $\boldsymbol{D}^+$ while $(DD)^-$ has 1 mM excess of $\boldsymbol{D}^-$. Please note that the total oligopeptide concentration in charged gels is still 5 mM, the same as neutral gels. It is important to verify that the excess oligopeptide is indeed incorporated into the hydrogel rather than freely floating inside the matrix. This was accomplished using NMR spectroscopy.

NMR 1D ^{1}H measurements were performed on $(LL)^+$, $(LL)^0$ and $(LL)^-$ gels to determine whether there was a significant difference in the amount of free oligopeptides after 24 hours of gelation. The ^{1}H peak heights of the three gels were

compared (Figure 5.5). Peak heights of the three gels were comparable to each other. This result indicates that the excess oligopeptide in a charged gel was incorporated into the hydrogel matrix to the same extent as the neutral gel, with hardly any free oligopeptide left. Hence any observed effects of the charged hydrogels on the hMSCs are indeed caused by charged hydrogels, not by charged free oligopeptides.

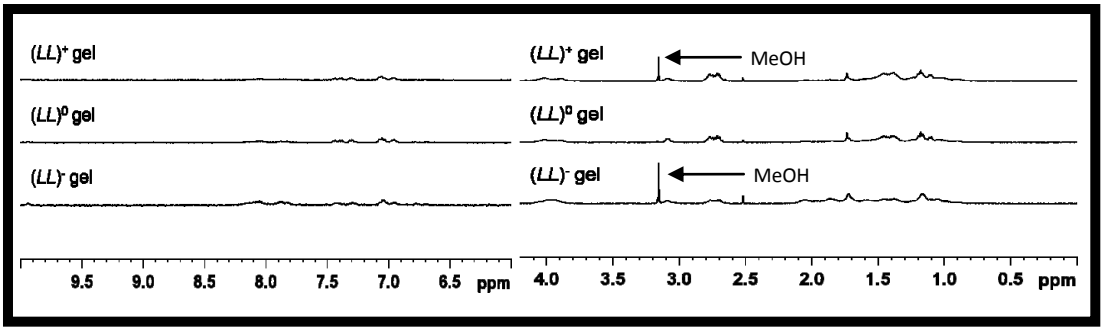

Figure 5.5. 1D ^{1}H NMR spectra for $(LL)^+$ gel, $(LL)^0$ gel and $(LL)^-$ gel plotted on the same scale. The figure is divided into two parts to exclude the unsuppressed portion of the H_2O peak around 4.75 ppm. The left panel is the aromatic region and the right panel is the aliphatic region. Here, the peak heights for all three gels very similar and small, indicating a lack of free oligopeptide present in the gels after 24 hours. Peak heights were calibrated using the proton signal from TSP (9mM proton concentration).

When homochiral gels of different charge statuses are compared (Figure 5.6), there is no statistically significant difference among the *LL*-gels in terms of hMSC attachment and proliferation. The only exception is that $(LL)^0$ had statistically significant higher cell attachment than $(LL)^+$ (Table S1) However, among $(DD)^+$, $(DD)^0$ and $(DD)^-$, the following trend of hMSC attachment and proliferation is observed:

$$(DD)^- > (DD)^0 > (DD)^+$$

The above order was statistically significant for both attachment and proliferation on day 1 but became less significant for proliferation on days 3 and 7 (Appendix Table A2). Nonetheless, the trend is very clear (Figure 5.6B).

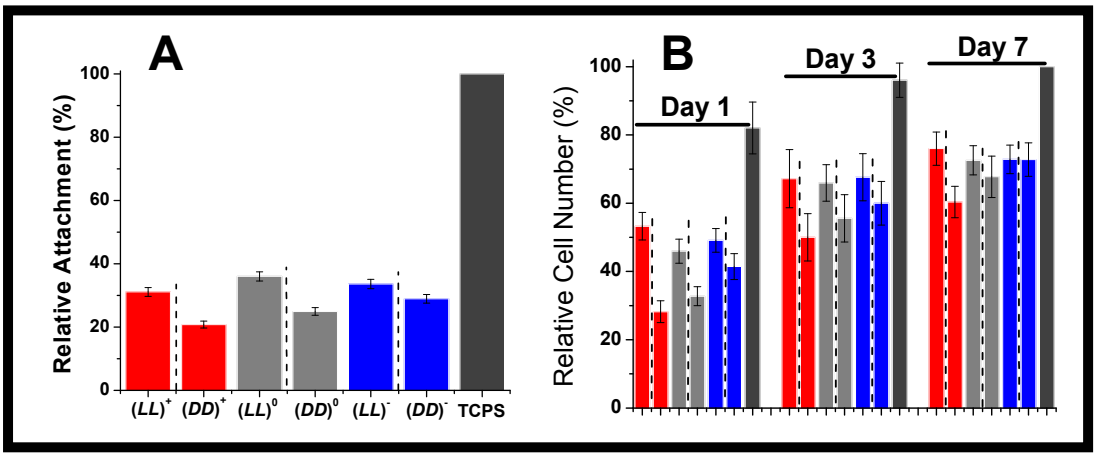

Figure 5.6. (A) Relative hMSC attachment to charged and neutral homochiral gels at 1 day after cell seeding. (B) hMSC cell number percentage on charged and neutral homochiral gels at 1, 3 and 7 days after seeding. Bar order and colors in (B) correspond to the same order and colors in (A). Adjacent bars separated by dashed lines are a pair of mirror images. For (A), results were normalized to TCPS. For (B), results were normalized to TCPS day 7. For both graphs, errors are expressed as the standard error of the mean (SEM).

In Figure 5.7, the difference between the number of live cells on $(DD)^-$ vs. $(DD)^+$ is also apparent. Figure 5.8 compares *L*-homochiral with *D*-homochiral gels of different charge statuses. Negative charges reduce the difference between *L*- and *D*-homochiral gels while positive charges amplify such difference. On day 7, there is no difference at all between $(LL)^-$ and $(DD)^-$ in cell proliferation. Hence, in terms of hMSC attachment and proliferation, the chirality mismatch between matrix and cells can be compensated to various extents by negative charges. However, negative charge did not have an effect on cell penetration into the *D*-gels. In Figure 5.7, it is

evident that images of cells on *L*-gels are blurry because they are situated on different focal planes, while images of cells on *D*-gels, regardless of charge status, remain clear.

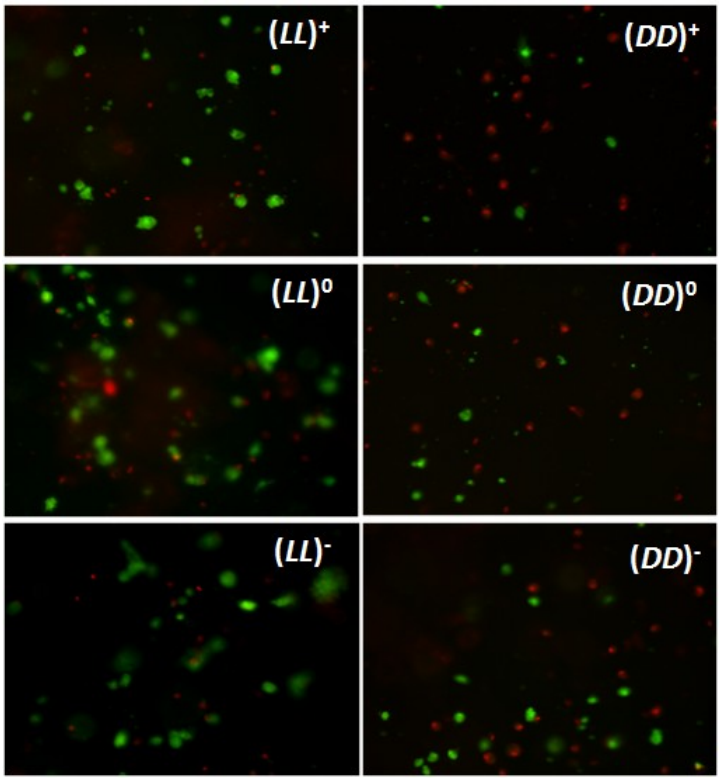

Figure 5.7. Representative live/dead images for charged and neutral homochiral gels at 1 day after cell seeding. Live hMSCs are green and dead hMSCs are red. Cell size is much larger and image clarity is much cloudier for *LL* images when compared with *DD* images. These images indicate cell penetrating into *LL* gels, but not into *DD* gels.

The reason why negative charges enhance the biocompatibility of the *D*-homochiral gel awaits further study. However, it is clear that such interplay between charge and chirality is unique to the *D*-homochiral gel since the *L*-homochiral gel shows no such trend at all (Figure 5.6 and appendix Table A2). Also clear is that this effect is not caused by negatively charged free peptides because hardly any is left in the hydrogel as shown by NMR studies (Figure 5.5).

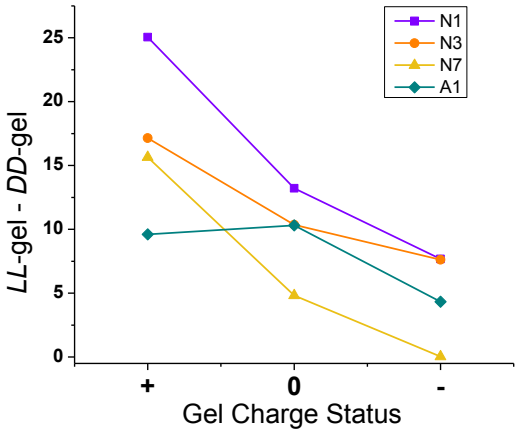

Figure 5.8. Calculated differences (*LL* – *DD*) in cell behavior on positive, neutral and negative gel pairs. In the figure legend, N1 is cell number day 1, N3 is cell number day 3, N7 is cell number day 7 and A1 is attachment day 1. Differences between positive pairs are larger than differences between negative pairs in both experiments and at all time points.

5.5 Conclusion

This work shows that, among oligopeptide hydrogels of various chiral compositions, the *L*-homochiral gel is the most biocompatible, leading to highest hMSC attachment and proliferation, while the racemic gel is the least biocompatible, leading to lowest hMSC attachment and proliferation. Most importantly, the disadvantage of the *D*-homochiral gel can be compensated by negative charges. This result points to the possibility of using charge and other factors to engineer biomaterials whose chirality is distinct from that of natural biomaterials but whose performance is close to that of natural biomaterials. Aside from practical applications, such materials offer new tools and opportunities to investigate biohomochirality, an important and unresolved question in biology.

Chapter 6: Conclusions

In this dissertation work, combinations of different types of biopolymers were investigated in order to create materials with the desired structural and mechanical properties in an effort to mimic natural vertebrate extracellular matrix. The constitutive biopolymers investigated include natural polysaccharides and engineered oligopeptides.

Creating the strongest materials possible requires an understanding of how individual network components and various conditions affect bulk material properties. In chapter 2, we examined how the addition of chondroitin affected the properties of chitosan-alginate networks. Samples containing chondroitin were stiffer and had greater tensile strengths than samples without chondroitin. However, the effectiveness of chondroitin addition was dependent on the order in which it was added. Effects of total polysaccharide concentration were also studied. Higher concentrations were associated with greater mechanical strengths. Structural analysis of the networks complemented the findings in this chapter, illustrating that chondroitin addition increased fiber thickness while Ca^{2+} addition caused fiber contraction thereby increasing fiber stiffness. Together, the two modifiers improved network density, resulting in greater stiffness and tensile strength.

In chapter 3, we prepared composite hydrogels in which the fibrous peptide networks were combined with the fibers assembled from long, charged polysaccharide structures. In this way, our materials would mimic the chemical and/or structural composition of extracellular matrix. The pure polysaccharide networks were very weak materials with low elastic moduli, but with significant

resistance to deformation. Incorporation of the polysaccharides into the oligopeptide hydrogel also resulted in materials (**CAP** and **CADP**) with very high resistance to deformation (strain values from 20 % to 100 %), far less brittle compared to the pure peptide hydrogel **P**. However, the propensity of the oligopeptides to form complexes with the polysaccharides may be responsible for the significant loss of stiffness of the composite material as compared to the pure peptide hydrogel. Structural analysis illustrated the aforementioned interaction between the oligopeptides and sugars. These results suggest a novel approach for creating highly deformation-resistant biomaterials.

In chapter 4, we studied the mechanical and structural properties of *L/L* and *D/D* oligopeptide hydrogels doped with four unique *D*-saccharide types. In all cases, at varying concentrations, *L/L* gels gelled faster and/or were stiffer than *D/D* gels in the presence of all saccharide types. This result suggests stronger interactions between *L*-oligopeptides and *D*-saccharides, regardless of saccharide size, shape or charge. Structural analysis corroborated these findings using a combination of techniques to examine the gels at the level of the fiber and the level of the network. This approach can provide insight on using chirality as another tool for tuning the properties of biopolymer-based biomaterials. In addition, it may give insight from a mechanical standpoint for why proteins and saccharides have opposite chirality in nature.

In chapter 5, the effects of chirality *and* charge on human mesenchymal stem cell (hMSC) behavior were studied using hydrogels assembled from oppositely charged oligopeptides. It was found that negative charges significantly improved

hMSC attachment and proliferation in *D*-oligopeptide gels but had little effect on their interactions with *L*-oligopeptide gels. This means that the disadvantage of the *D*-homochiral gel can be compensated by negative charges. From this result, we see the possibility of using charge and other factors to engineer oligopeptide-based biomaterials whose chirality is distinct from that of natural biomaterials but whose performance is close to that of natural biomaterials. These biomaterials also offer new tools and opportunities to investigate biohomochirality, an important and unresolved question in biology.

Taken together, this dissertation work provides a better understanding about how biopolymer interactions affect mechanical and structural properties of biomaterials, and how those properties can affect stem cell behavior. Further studies will continue to characterize and define the biological potential of these new materials and how they can possibly influence the behavior of many different cell types.

Appendices

Table A1. Young's modulus obtained by compression of dry type **5C** networks. Ultimate tensile strength obtained by applying tension to dry type **5C** networks. Test results for 5 type **5C** networks, their averages and standard deviations. Separate samples were used for compression and tensile testing.

Test Number	Elastic modulus (MPa)	Ultimate tensile strength (kPa)
1	4.09	74.96
2	4.21	77.12
3	5.14	67.61
4	4.75	69.27
5	3.88	66.82
Average	**4.41**	**71.16**
Stdev	**0.52**	**4.61**

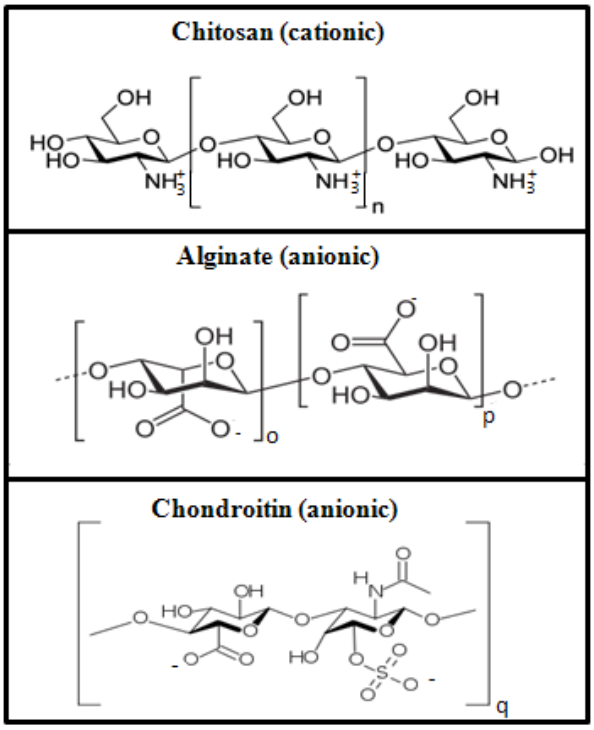

Figure A1. Positively charged chitosan negatively charged alginate and negatively charged chondroitin interact electrostatically to form fibrous networks.

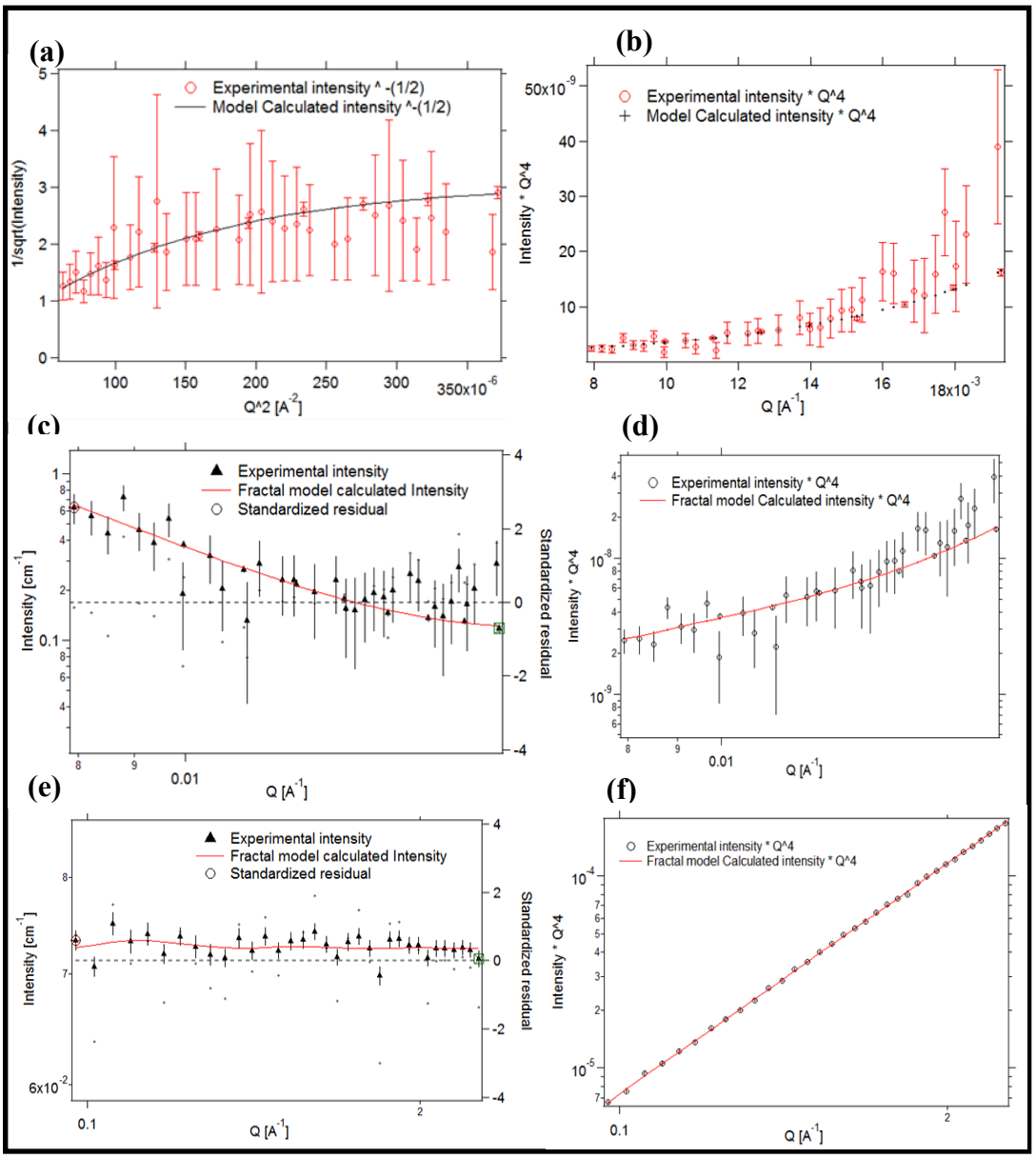

Figure A2. Analysis of SANS data for alginate. (a) Debye-Bueche estimation for correlation length. (b) $I(Q)*Q^4$ vs. Q fit for Debye-Bueche analysis. (c) Mass fractal estimation. (d) $I(Q)*Q^4$ vs. Q fit for mass fractal estimation. (e) Surface fractal estimation. (f) $I(Q)*Q^4$ vs. Q fit for surface fractal estimation.

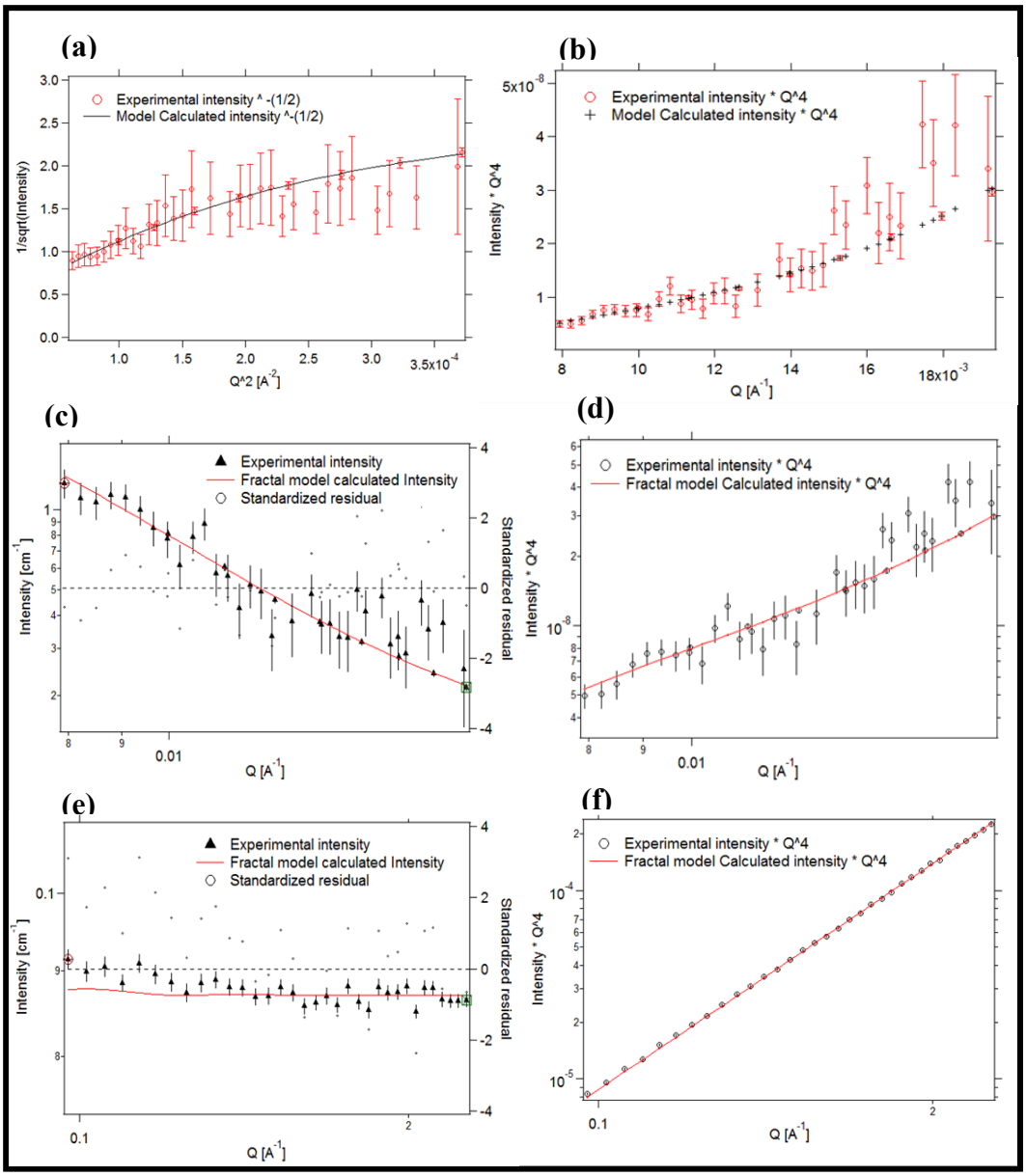

Figure A3. Analysis of SANS data for chitosan. (a) Debye-Bueche estimation for correlation length. (b) $I(Q)*Q^4$ vs. Q fit for Debye-Bueche analysis. (c) Mass fractal estimation. (d) $I(Q)*Q^4$ vs. Q fit for mass fractal estimation. (e) Surface fractal estimation. (f) $I(Q)*Q^4$ vs. Q fit for surface fractal estimation.

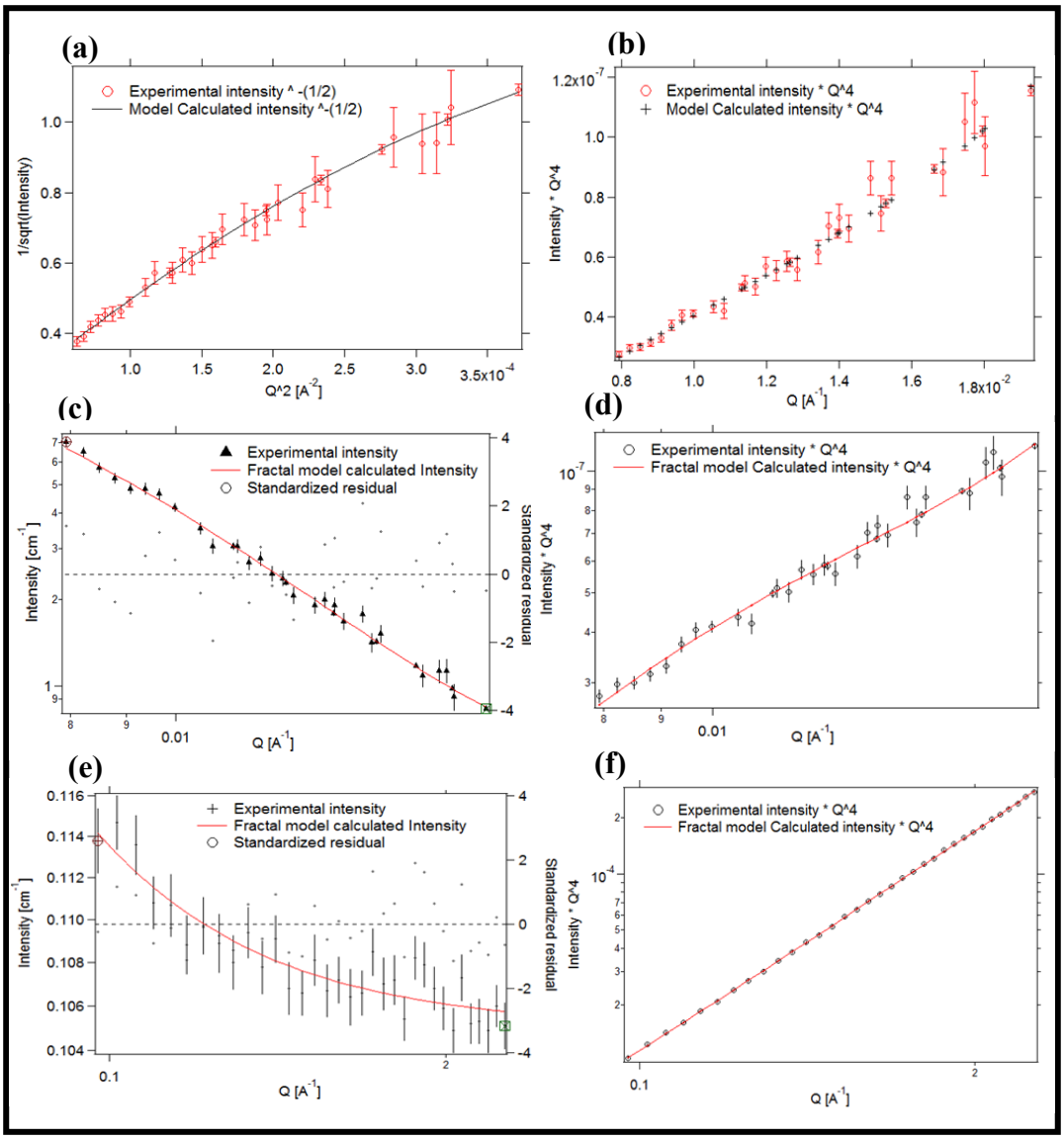

Figure A4. Analysis of SANS data for chitosan+alginate. (a) Debye-Bueche estimation for correlation length. (b) $I(Q)*Q^4$ vs. Q fit for Debye-Bueche analysis. (c) Mass fractal estimation. (d) $I(Q)*Q^4$ vs. Q fit for mass fractal estimation. (e) Surface fractal estimation. (f) $I(Q)*Q^4$ vs. Q fit for surface fractal estimation.

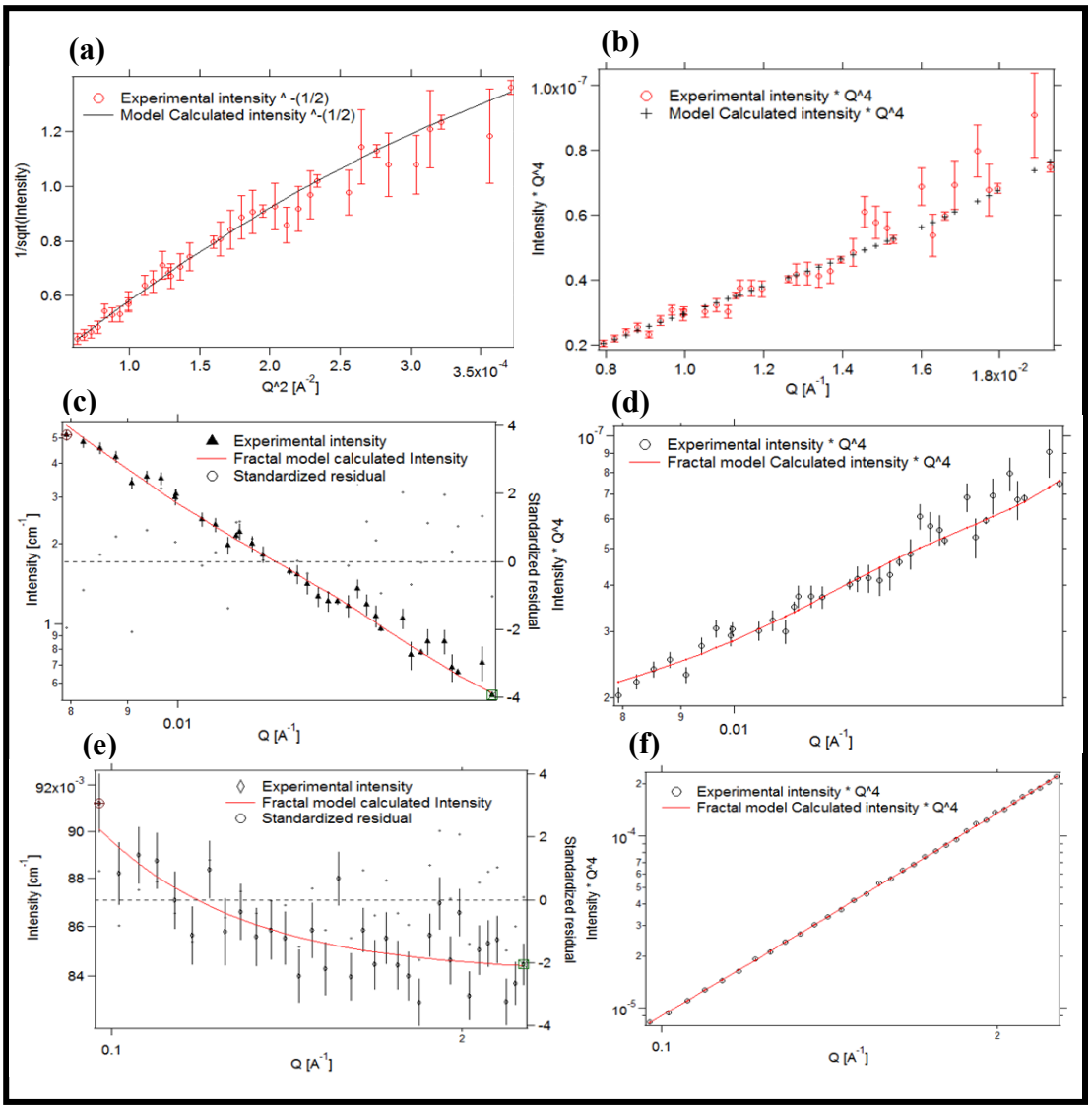

Figure A5. Analysis of SANS data for chitosan+alginate+chondroitin. (a) Debye-Bueche estimation for correlation length. (b) $I(Q)*Q^4$ vs. Q fit for Debye-Bueche analysis. (c) Mass fractal estimation. (d) $I(Q)*Q^4$ vs. Q fit for mass fractal estimation. (e) Surface fractal estimation. (f) $I(Q)*Q^4$ vs. Q fit for surface fractal estimation.

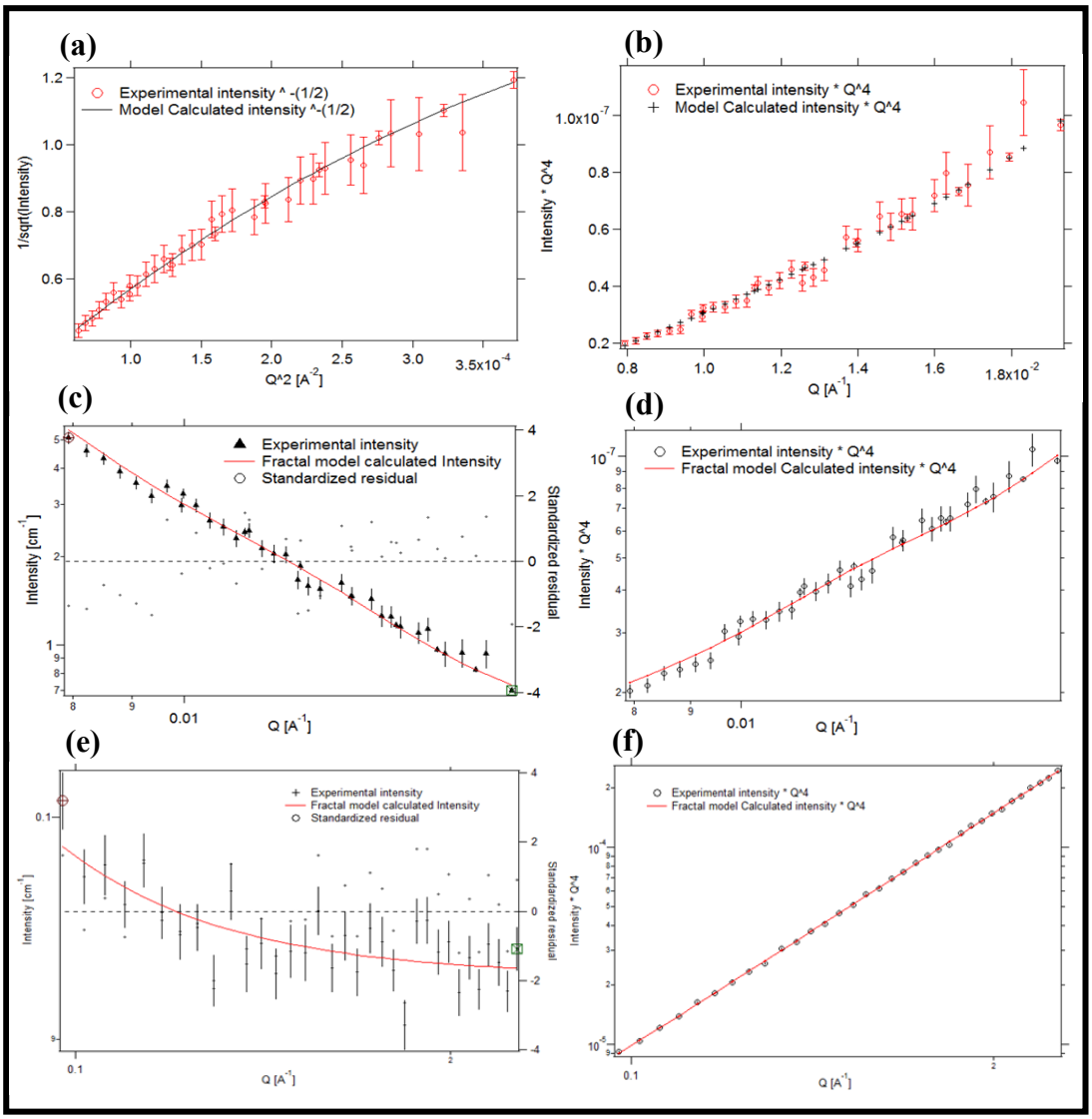

Figure A6. Analysis of SANS data for chitosan+alginate+calcium. (a) Debye-Bueche estimation for correlation length. (b) $I(Q)*Q^4$ vs. Q fit for Debye-Bueche analysis. (c) Mass fractal estimation. (d) $I(Q)*Q^4$ vs. Q fit for mass fractal estimation. (e) Surface fractal estimation. (f) $I(Q)*Q^4$ vs. Q fit for surface fractal estimation.

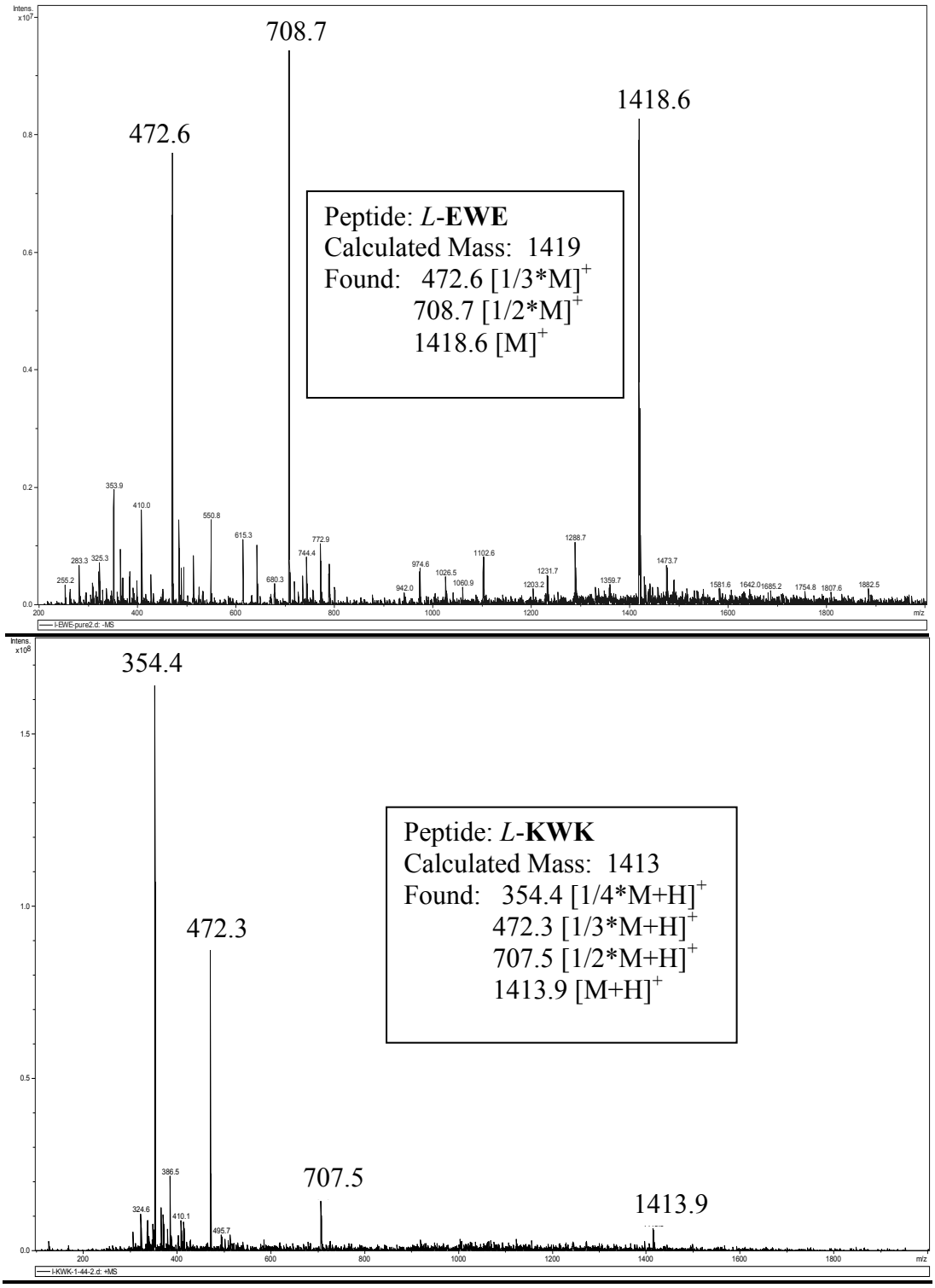

Figure A7. Electrospray Ionization mass spectrometry (ESI-MS) was performed with a Bruker. ESI-MS experiments were performed by diluting each peptide solution with a 50:50 mix of ethanol and water. For EWE, detection was in negative mode. For KWK, detection was in positive mode.

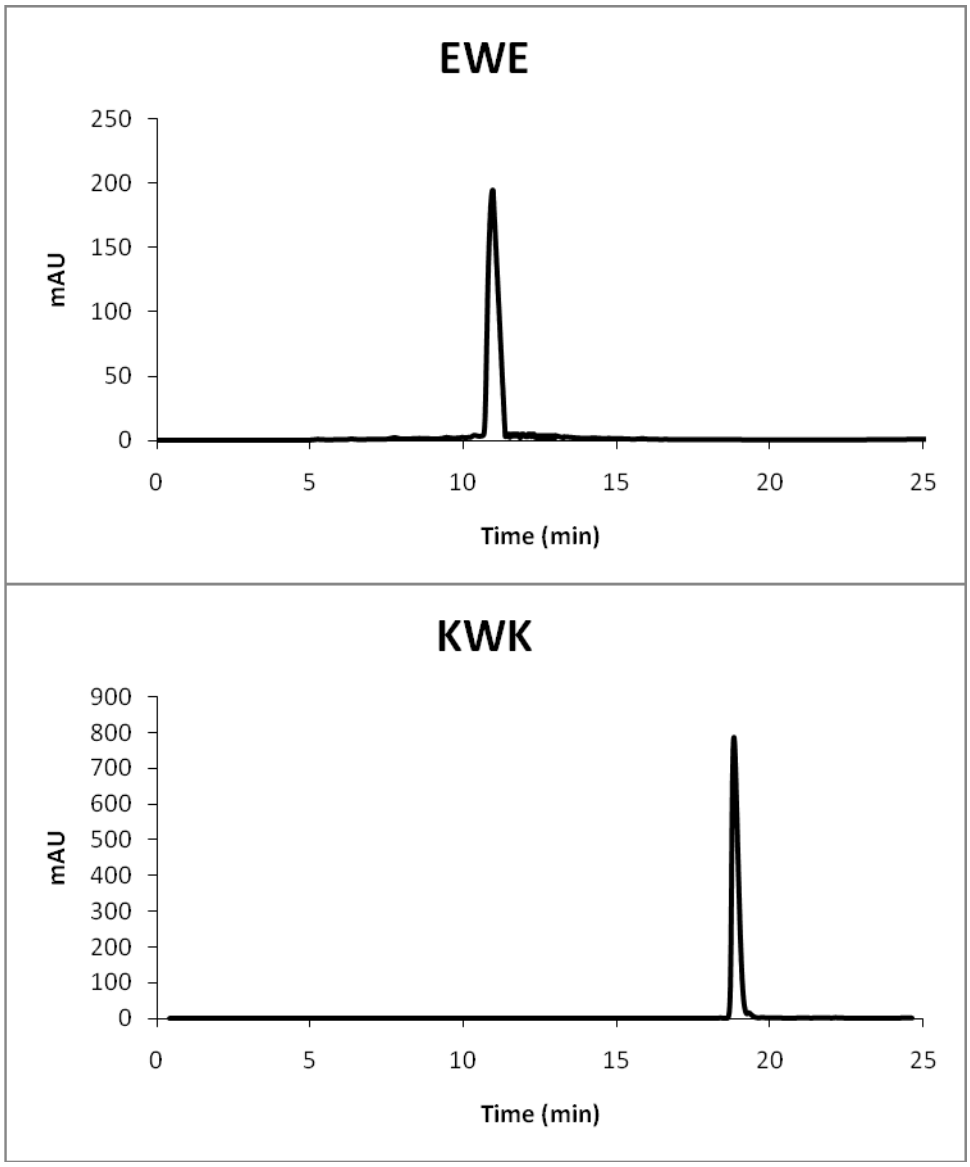

Figure A8. Analytical reversed-phase HPLC chromatogram of peptides acquired with HP1100 chromatograph system (Agilent Technologies). Column: Zorbax 300SB-C18 (4.6 × 250 mm i.d.). Elution profiles were monitored at 280nm. Eluents for **EWE**: solvent A: 20 mM NH_4HCO_3 in water, pH 7.0; solvent B: 20 mM NH_4HCO_3 in water (40%) + methanol (60%) mixture, pH 7.0. Eluents for **KWK**: solvent A: 0.1% trifluoroacetic acid (TFA) in water, pH 2.0; solvent B: 0.1% TFA in methanol, pH 2.0. Chromatograph run conditions for all the peptides: flow rate: 1ml/min; gradient: 2% B/min; temperature: ambient.

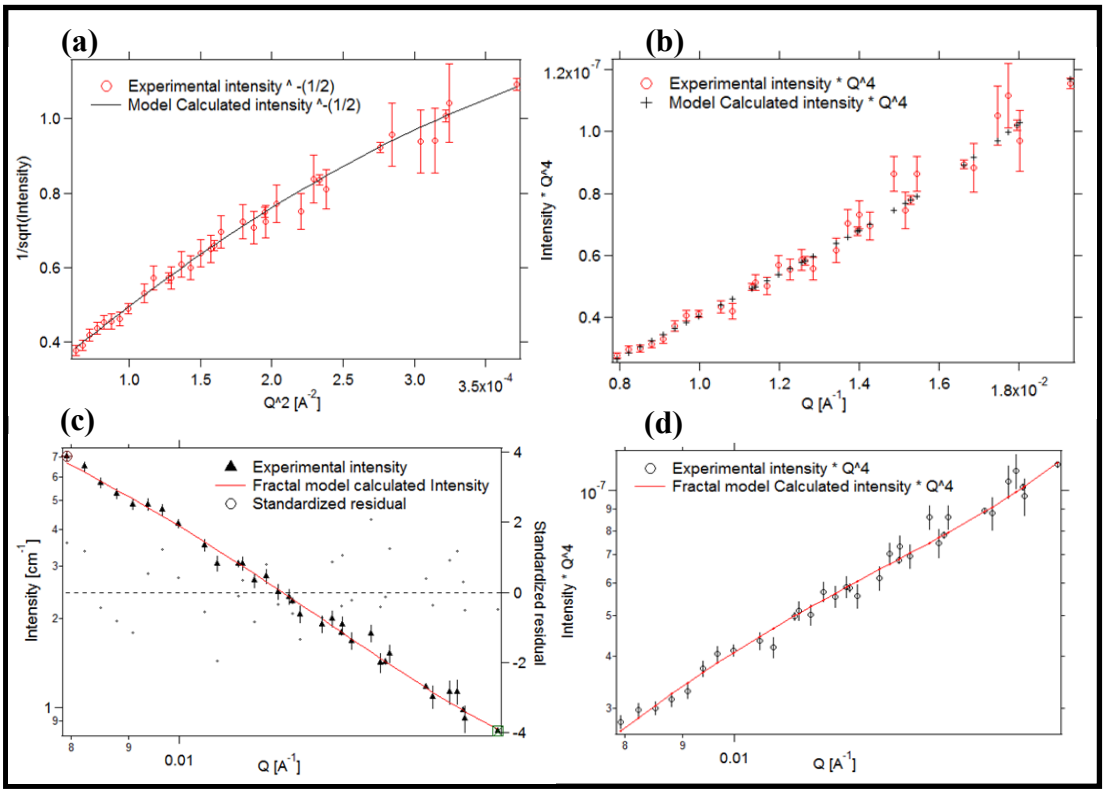

Figure A9. Analysis of SANS data for Chitosan+Alginate. (a) Debye-Bueche estimation for correlation length. (b) $I(Q)*Q^4$ vs. Q fit for Debye-Bueche analysis. (c) Mass fractal estimation. (d) $I(Q)*Q^4$ vs. Q fit for mass fractal estimation. Error bars represent statistical uncertainties corresponding to one standard deviation.

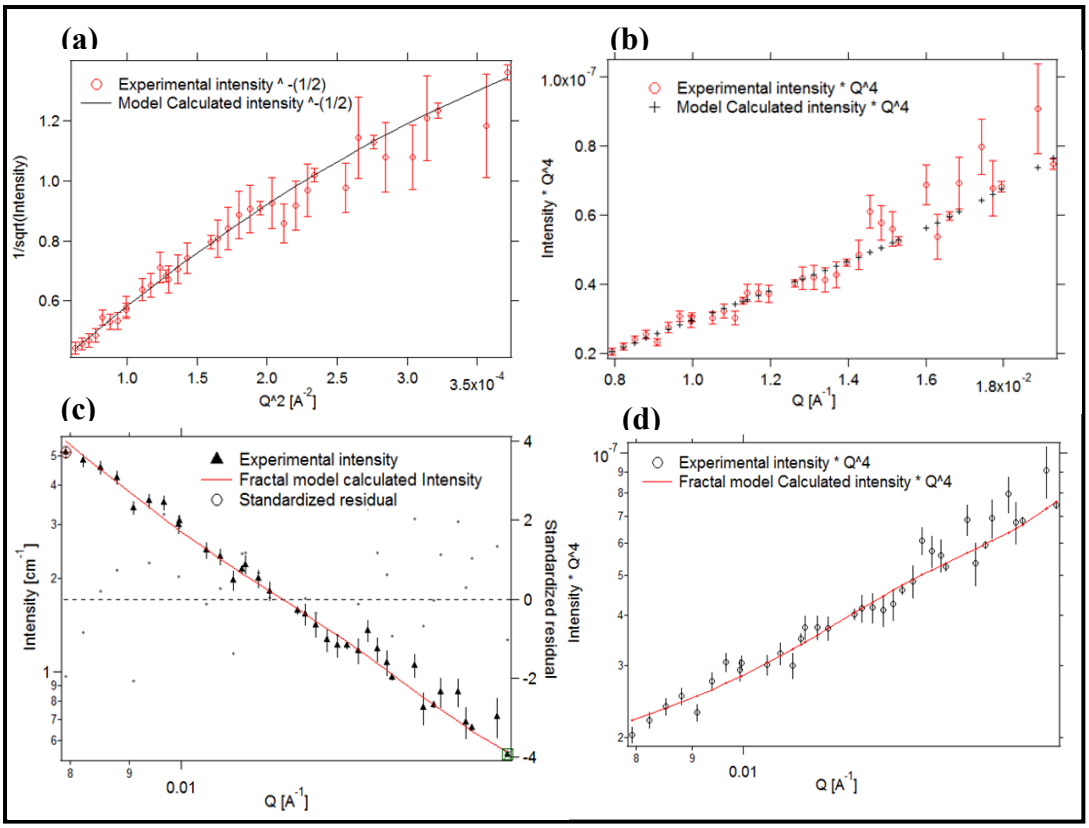

Figure A10. Analysis of SANS data for Chitosan+Alginate+Chondroitin. (a) Debye-Bueche estimation for correlation length. (b) $I(Q)*Q^4$ vs. Q fit for Debye-Bueche analysis. (c) Mass fractal estimation. (d) $I(Q)*Q^4$ vs. Q fit for mass fractal estimation. Error bars represent statistical uncertainties corresponding to one standard deviation.

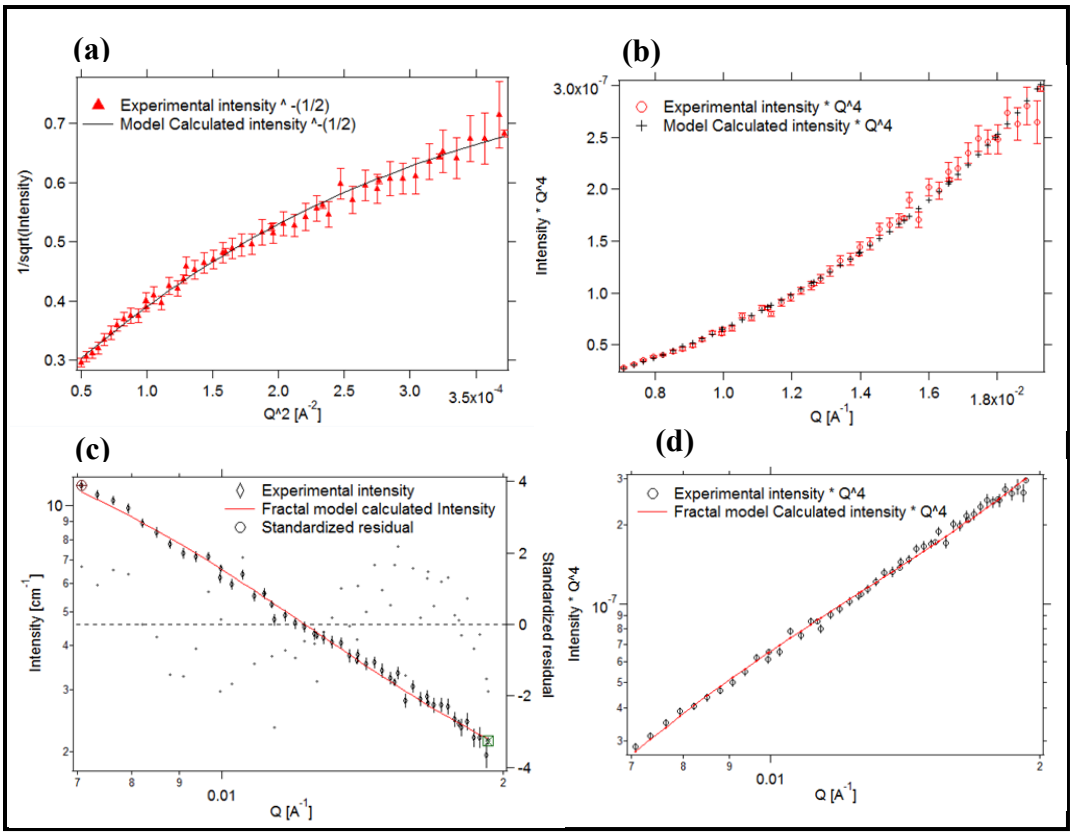

Figure A11. Analysis of SANS data for Chitosan+Alginate+Peptides. (a) Debye-Bueche estimation for correlation length. (b) $I(Q)*Q^4$ vs. Q fit for Debye-Bueche analysis. (c) Mass fractal estimation. (d) $I(Q)*Q^4$ vs. Q fit for mass fractal estimation. Error bars represent statistical uncertainties corresponding to one standard deviation.

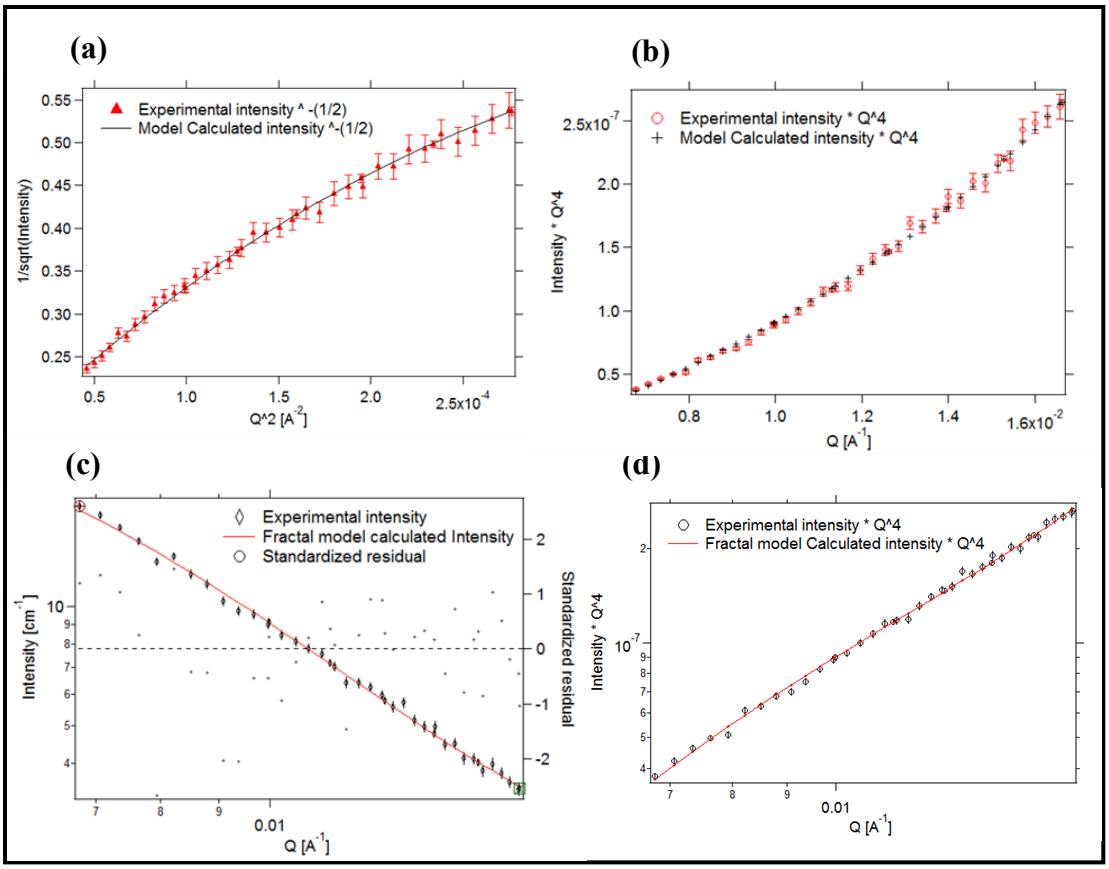

Figure A12. Analysis of SANS data for Chitosan+Alginate+Chondroitin+Peptides. (a) Debye-Bueche estimation for correlation length. (b) $I(Q)*Q^4$ vs. Q fit for Debye-Bueche analysis. (c) Mass fractal estimation. (d) $I(Q)*Q^4$ vs. Q fit for mass fractal estimation. Error bars represent statistical uncertainties corresponding to one standard deviation.

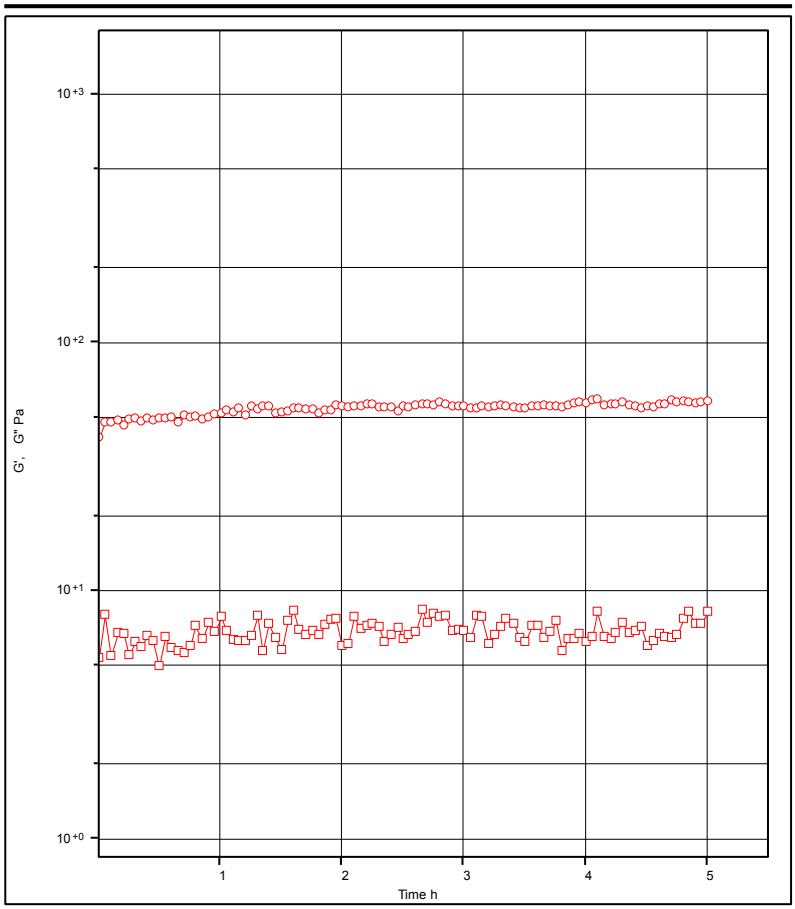

Figure A13. Time-sweep measurements of viscoelastic properties of Chitosan+Alginate performed after frequency-sweep confirming the stability of the gel.

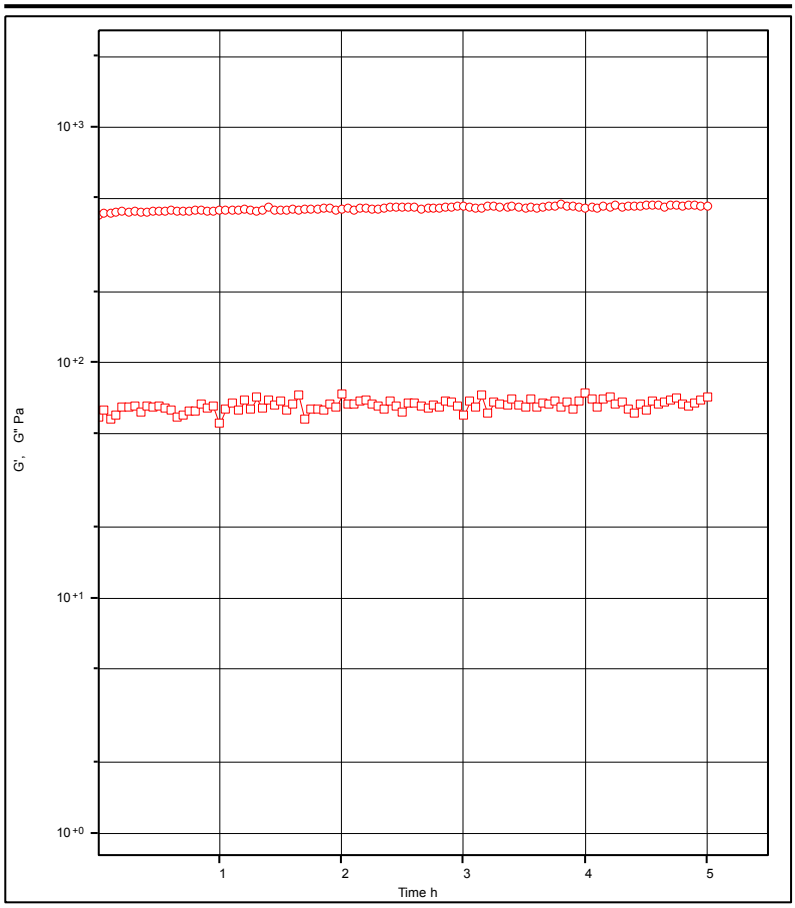

Figure A14. Time-sweep measurements of viscoelastic properties of Chitosan+Alginate+Chondroitin performed after frequency-sweep confirming the stability of the gel.

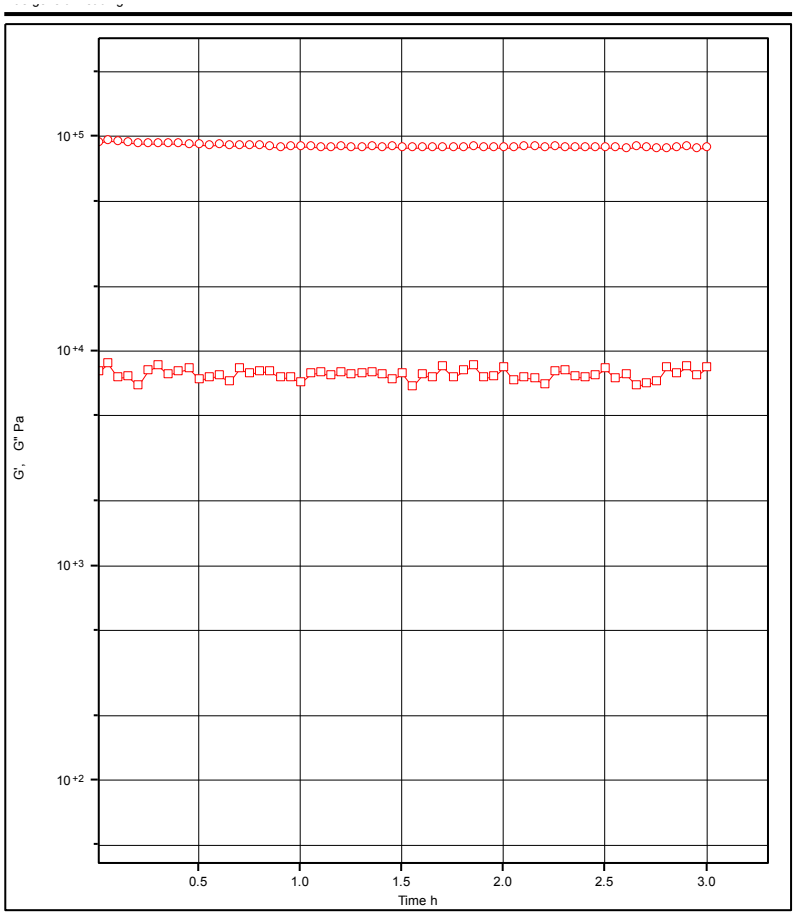

Figure A15. Time-sweep measurements of viscoelastic properties of peptide hydrogel KWK+EWE performed after frequency-sweep confirming the stability of the gel.

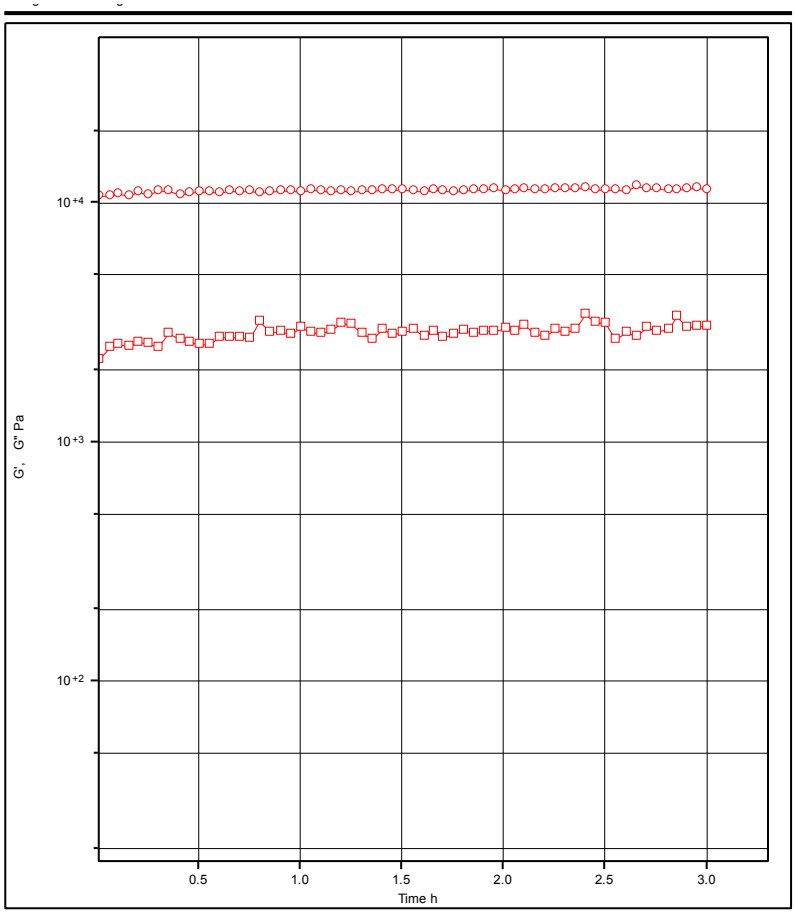

Figure A16. Time-sweep measurements of viscoelastic properties of mixed peptide Chitosan+Alginate hydrogel performed after frequency-sweep confirming the stability of the gel.

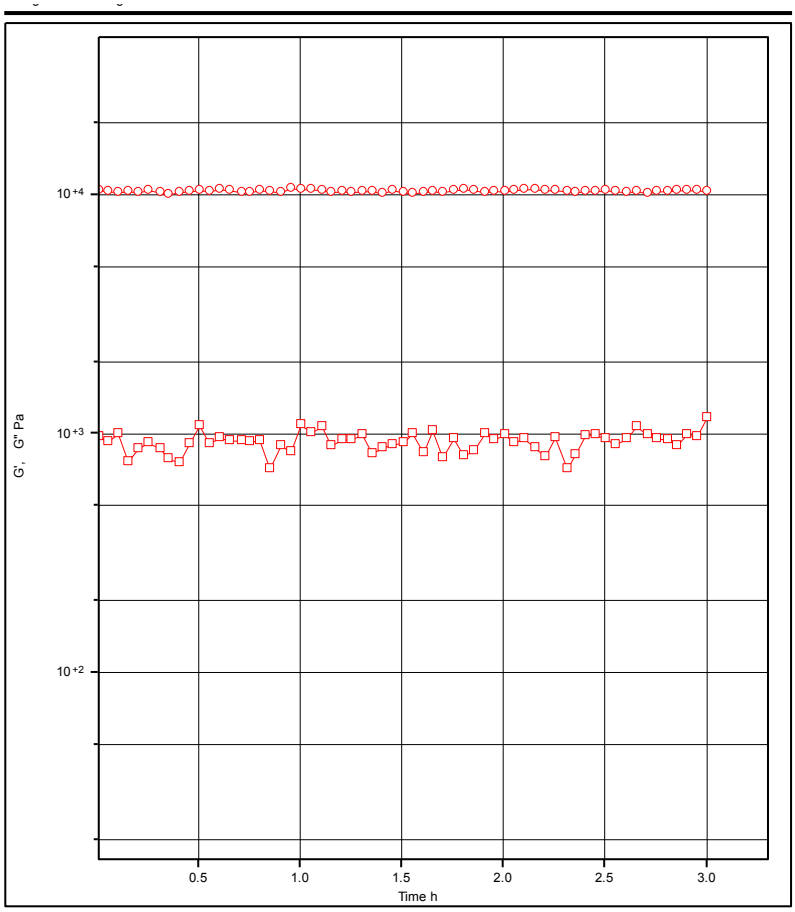

Figure A17. Time-sweep measurements of viscoelastic properties of mixed peptide Chitosan+Alginate+Chondroitin hydrogel performed after frequency-sweep confirming the stability of the gel.

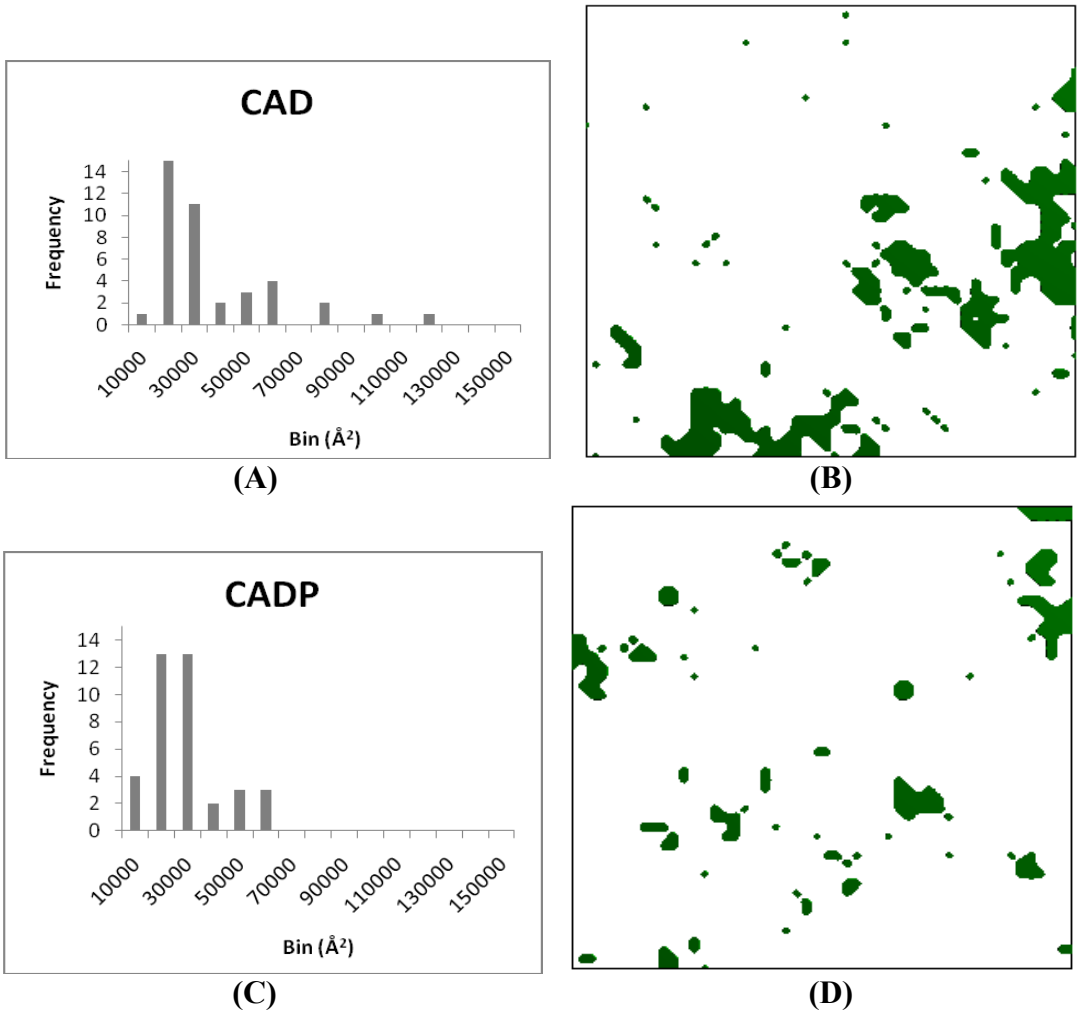

Figure A18. Histograms (A&C) and representative slices (B&D) from **CAD** (chitosan+alginate+chondroitin) and **CADP** (chitosan+alginate+chondroitin and peptide hydrogel from **KWK** and **EWE**) samples.

To obtain the above slices we have processed the SANS data of the **CAD** and **CADP** networks (Figure S12) using SAXSMorph program (Ingham, B.; Li, H.; Allen, E. L.; Toney, M. F. J. Appl. Cryst. 2011, 44, 221–224) and areas within each slice were found using NIH ImageJ routine (Abramoff, M. D.; Magelhaes, P. J.; Ram, S. J. Biophotonics International 2004, 11, 36–42). The areas found within each slice were combined into histograms (A&C) which gave notably different distributions. It is apparent in both the qualitative slices and the corresponding quantitative histograms that the addition of peptides into the system decreases the size of the fibers and the aggregations. The histogram for **CAD** shows multiple areas larger than 70,000 $Å^2$ whereas the histogram for **CADP** does not have any areas larger than 70,000 $Å^2$. From the qualitative slices, a difference in the size of areas in **CAD** and **CADP** is also visually noticeable. These findings are consistent with the shape analysis which shows that peptide addition greatly influences the resulting material, disrupting the network formed by pure polysaccharides.

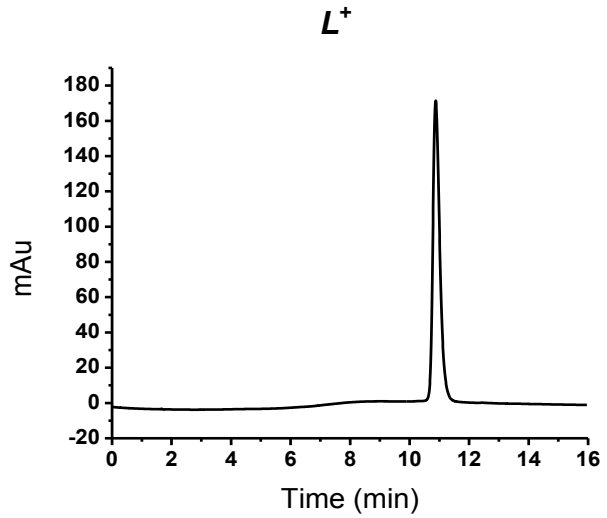

Figure A19. Analytical reversed-phase HPLC chromatogram of L^+ acquired with HP1100 chromatograph system (Agilent Technologies). Column: Zorbax 300SB-C18 (4.6 × 250 mm i.d.). Elution profiles were monitored at 280nm. Eluents: solvent A: 0.1% trifluoroacetic acid (TFA) in water, pH 2.0; solvent B: 0.1% TFA in methanol, pH 2.0. Chromatograph run conditions for all the peptides: flow rate: 1ml/min; gradient: 2% B/min; temperature: ambient.

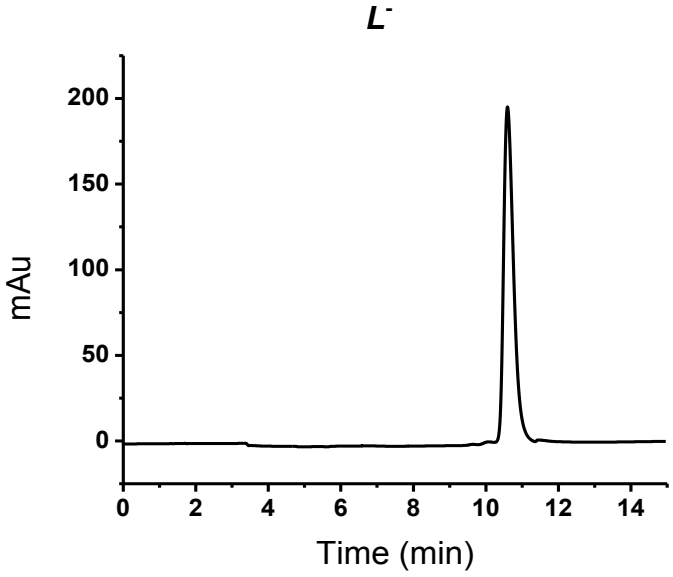

Figure A20. Analytical reversed-phase HPLC chromatogram of L^- acquired with HP1100 chromatograph system (Agilent Technologies). Column: Zorbax 300SB-C18 (4.6 × 250 mm i.d.). Elution profiles were monitored at 280nm. Eluents: solvent A: 20 mM NH4HCO3 in water, pH 7.0; solvent B: 20 mM NH4HCO3 in water (40%) + methanol (60%) mixture, pH 7.0. Chromatograph run conditions for all the peptides: flow rate: 1ml/min; gradient: 2% B/min; temperature: ambient.

D^+

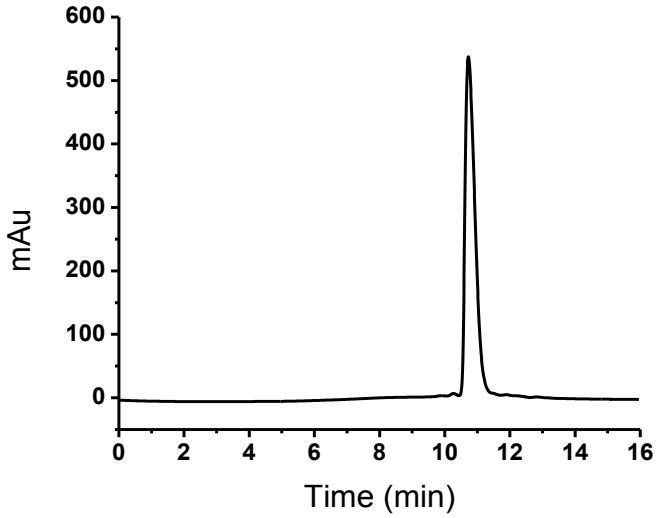

Figure A21. Analytical reversed-phase HPLC chromatogram of $\boldsymbol{D}^{+}$ acquired with HP1100 chromatograph system (Agilent Technologies). Column: Zorbax 300SB-C18 (4.6 × 250 mm i.d.). Elution profiles were monitored at 280nm. Eluents: solvent A: 0.1% trifluoroacetic acid (TFA) in water, pH 2.0; solvent B: 0.1% TFA in methanol, pH 2.0. Chromatograph run conditions for all the peptides: flow rate: 1ml/min; gradient: 2% B/min; temperature: ambient.

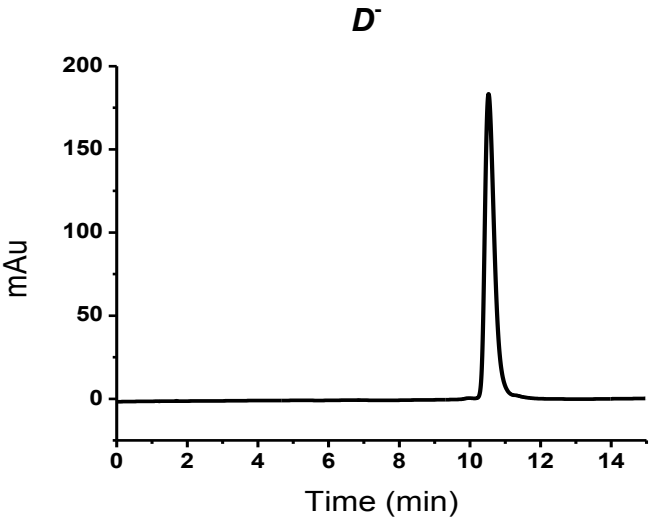

Figure A22. Analytical reversed-phase HPLC chromatogram of $\boldsymbol{D}^{-}$ acquired with HP1100 chromatograph system (Agilent Technologies). Column: Zorbax 300SB-C18 (4.6 × 250 mm i.d.). Elution profiles were monitored at 280nm. Eluents: solvent A: 20 mM NH4HCO3 in water, pH 7.0; solvent B: 20 mM NH4HCO3 in water (40%) + methanol (60%) mixture, pH 7.0. Chromatograph run conditions for all the peptides: flow rate: 1ml/min; gradient: 2% B/min; temperature: ambient.

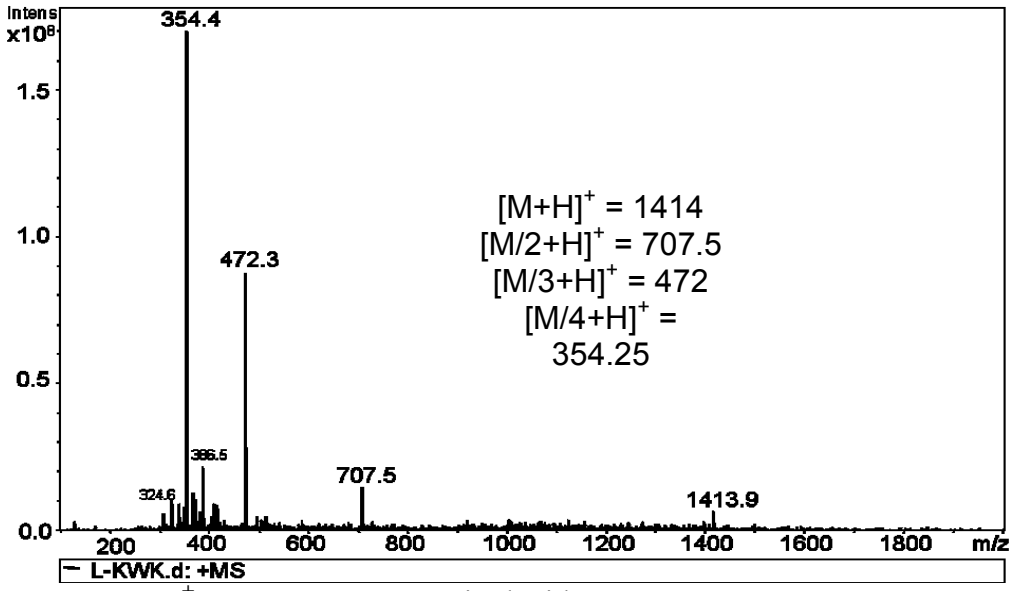

Figure A23. L^+ Mass spectrum acquired with an Amazon X Ion Trap Mass Spectrometer (Bruker) in positive ion mode. Flow rate of 3 μL/min, 10 psi nebulizer pressure, 4 L/min dry gas flow and 250˚C gas temperature.

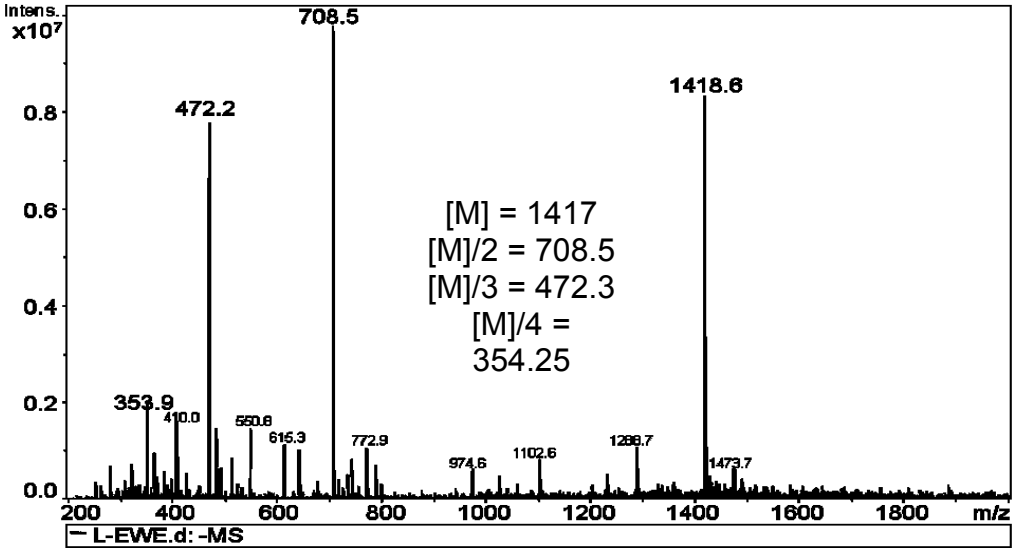

Figure A24. L^- mass spectrum acquired with an Amazon X Ion Trap Mass Spectrometer (Bruker) in negative ion mode. Flow rate of 3 μL/min, 10 psi nebulizer pressure, 4 L/min dry gas flow and 250˚C gas temperature.

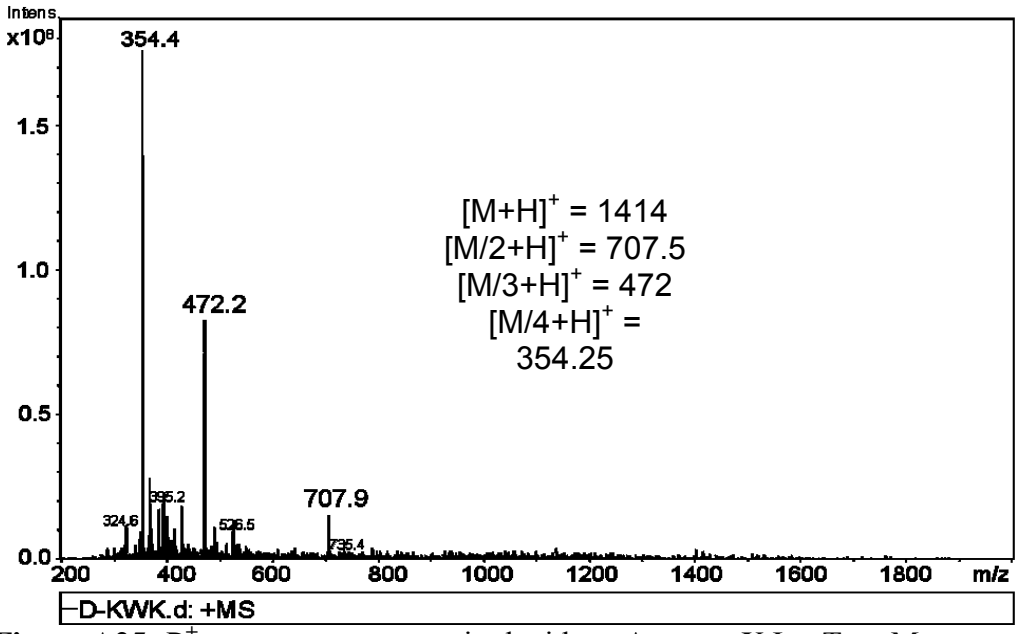

Figure A25. D^+ mass spectrum acquired with an Amazon X Ion Trap Mass Spectrometer (Bruker) in positive ion mode. Flow rate of 3 µL/min, 10 psi nebulizer pressure, 4 L/min dry gas flow and 250˚C gas temperature.

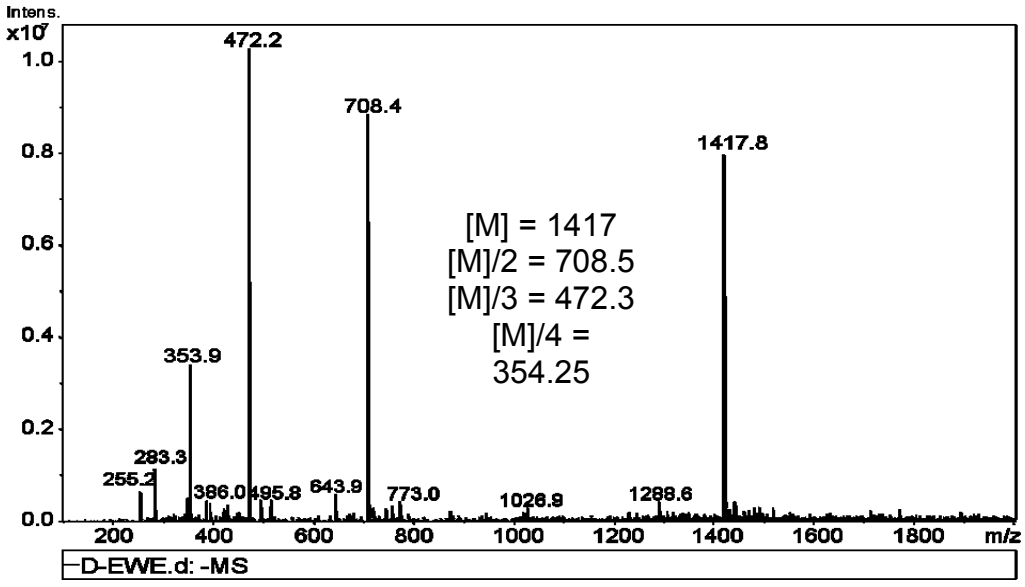

Figure A26. D^- mass spectrum acquired with an Amazon X Ion Trap Mass Spectrometer (Bruker) in negative ion mode. Flow rate of 3 µL/min, 10 psi nebulizer pressure, 4 L/min dry gas flow and 250˚C gas temperature.

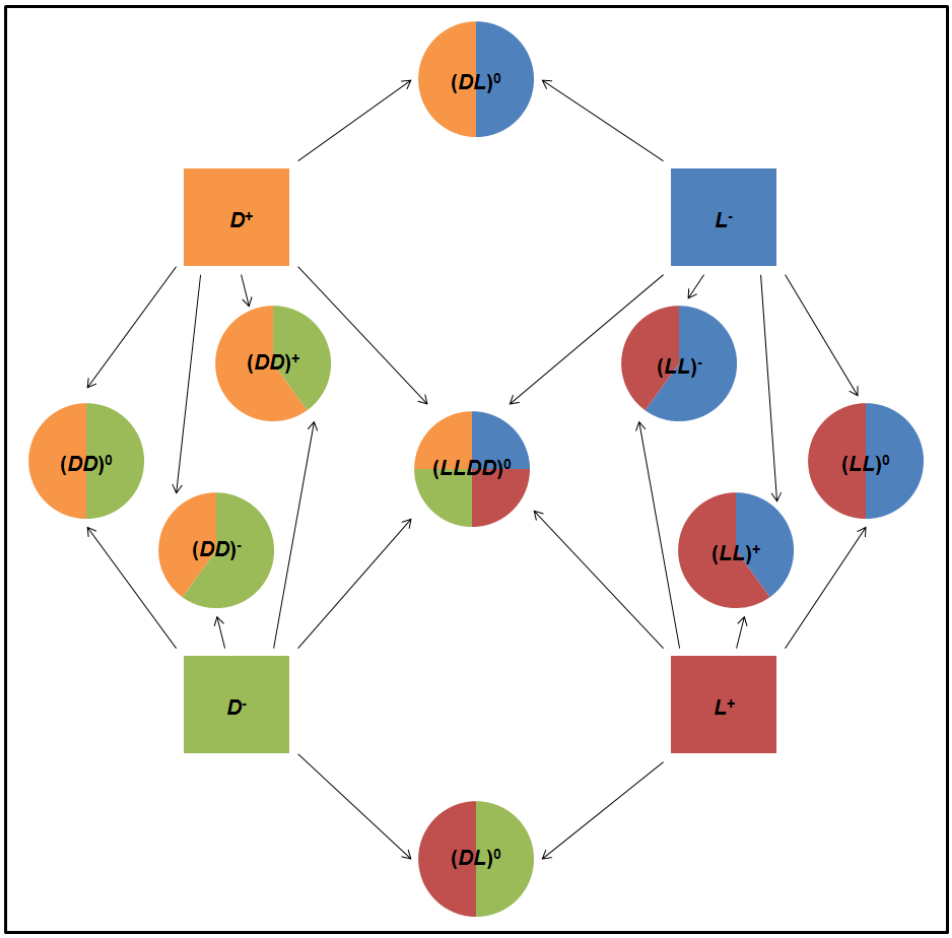

Figure A27. Pictorial description of how each gel was made using different amounts of four parent oligopeptides. The final oligopeptide concentration for all gels was 5 mM. Neutral gels were made with 2.5 mM $\boldsymbol{D}^+$ or $\boldsymbol{L}^+$ and 2.5 mM $\boldsymbol{D}^-$ or $\boldsymbol{L}^-$, positively charged gels were made with 3 mM $\boldsymbol{D}^+$ or $\boldsymbol{L}^+$ and 2 mM $\boldsymbol{D}^-$ or $\boldsymbol{L}^-$ and negatively charged gels were made with 2 mM $\boldsymbol{D}^+$ or $\boldsymbol{L}^+$ and 3 mM $\boldsymbol{D}^-$ or $\boldsymbol{L}^-$.

Table A2. Results from a series of paired t-tests to determine significant differences in cell behavior on different hydrogel types. Table (A) shows attachment and table (B) shows proliferation. For acceptance, $p < 0.01$.

A. Attachment (n = 54)

Hypothesis	p value	Result
Single Peptides		
$L^- > L^+$	0.4	rejected
$L^+ > D^+$	0.2	rejected
$L^- > D^-$	0.2	rejected
$D^- > D^+$	0.2	rejected
$D^- > L^+$	0.4	rejected
$L^- > D^+$	0.05	rejected
Neutral Gels		
$(LL)^0 > (LD)^0$	5.0E-05	accepted
$(LL)^0 > (DL)^0$	0.0001	accepted
$(DL)^0 > (LD)^0$	0.1	rejected
$(LD)^0 > (DD)^0$	0.2	rejected
$(DL)^0 > (DD)^0$	0.04	rejected
$(LL)^0 > (DD)^0$	1.0E-06	accepted
$(DD)^0 > (LLDD)^0$	0.011	rejected
$(LD)^0 > (LLDD)^0$	0.001	accepted
$(DL)^0 > (LLDD)^0$	8.00E-04	accepted
Charged Gels		
$(DD)^0 > (DD)^+$	0.004	accepted
$(DD)^- > (DD)^0$	0.009	accepted
$(LL)^+ > (DD)^+$	1.0E-06	accepted
$(LL)^- > (DD)^-$	0.004	accepted
$(LL)^0 > (LL)^+$	0.001	accepted
$(LL)^0 > (LL)^-$	0.1	rejected
$(LL)^- > (LL)^+$	0.04	rejected

B. Proliferation (n = 9)

Hypothesis	Day	p value	Result
Single Peptides			
$L^- > L^+$	1	0.2	rejected
$L^+ > D^+$	1	0.1	rejected

$L^- > D^-$	1	0.1	rejected
$D^- > D^+$	1	0.06	rejected
$D^- > L^+$	1	0.2	rejected
$L^- > D^+$	1	0.02	rejected
$L^- > L^+$	3	0.2	rejected
$L^+ > D^+$	3	0.5	rejected
$L^- > D^-$	3	0.5	rejected
$D^- > D^+$	3	0.3	rejected
$D^- > L^+$	3	0.3	rejected
$L^- > D^+$	3	0.2	rejected
$L^- > L^+$	7	0.4	rejected
$L^+ > D^+$	7	0.4	rejected
$L^- > D^-$	7	0.4	rejected
$D^- > D^+$	7	0.4	rejected
$D^- > L^+$	7	0.5	rejected
$L^- > D^+$	7	0.2	rejected
Neutral Gels			
$(LL)^0 > (LD)^0$	1	0.3	rejected
$(LL)^0 > (DL)^0$	1	0.3	rejected
$(DL)^0 > (LD)^0$	1	0.3	rejected
$(LD)^0 > (DD)^0$	1	3.0E-05	accepted
$(DL)^0 > (DD)^0$	1	3.0E-05	accepted
$(LL)^0 > (DD)^0$	1	7.0E-04	accepted
$(LL)^0 > (LLDD)^0$	1	0.004	accepted
$(LD)^0 > (LLDD)^0$	1	7.0E-04	accepted
$(DL)^0 > (LLDD)^0$	1	0.002	accepted
$(LLDD)^0 > (DD)^0$	1	0.2	rejected
$(LL)^0 > (LD)^0$	3	0.2	rejected
$(LL)^0 > (DL)^0$	3	0.2	rejected
$(DL)^0 > (LD)^0$	3	0.3	rejected
$(LD)^0 > (DD)^0$	3	0.4	rejected
$(DL)^0 > (DD)^0$	3	0.3	rejected
$(LL)^0 > (DD)^0$	3	0.03	rejected
$(LL)^0 > (LLDD)^0$	3	2.0E-04	accepted
$(LD)^0 > (LLDD)^0$	3	4.0E-04	accepted
$(DL)^0 > (LLDD)^0$	3	0.002	accepted
$(DD)^0 > (LLDD)^0$	3	0.012	rejected

$(LL)^0 > (LD)^0$	7	0.003	accepted
$(LL)^0 > (DL)^0$	7	6.0E-04	accepted
$(DL)^0 > (LD)^0$	7	0.3	rejected
$(DD)^0 > (LD)^0$	7	0.1	rejected
$(DD)^0 > (DL)^0$	7	0.09	rejected
$(LL)^0 > (DD)^0$	7	0.2	rejected
$(LD)^0 > (LLDD)^0$	7	3.0E-05	accepted
$(DL)^0 > (LLDD)^0$	7	3.0E-05	accepted
$(DD)^0 > (LLDD)^0$	7	5.0E-05	accepted
Charged Gels			
$(DD)^0 > (DD)^+$	1	0.004	accepted
$(DD)^- > (DD)^0$	1	5.0E-04	accepted
$(DD)^- > (DD)^+$	1	0.002	accepted
$(LL)^+ > (DD)^+$	1	5.0E-06	accepted
$(LL)^- > (DD)^-$	1	0.0004	accepted
$(LL)^0 > (LL)^+$	1	0.014	rejected
$(LL)^- > (LL)^0$	1	0.09	rejected
$(LL)^- > (LL)^+$	1	0.03	rejected
$(DD)^0 > (DD)^+$	3	0.014	rejected
$(DD)^- > (DD)^0$	3	0.1	rejected
$(DD)^- > (DD)^+$	3	0.004	accepted
$(LL)^+ > (DD)^+$	3	0.005	accepted
$(LL)^- > (DD)^-$	3	0.09	rejected
$(LL)^0 > (LL)^+$	3	0.4	rejected
$(LL)^- > (LL)^0$	3	0.4	rejected
$(LL)^- > (LL)^+$	3	0.5	rejected
$(DD)^0 > (DD)^+$	7	0.1	rejected
$(DD)^- > (DD)^0$	7	0.2	rejected
$(DD)^- > (DD)^+$	7	0.002	accepted
$(LL)^+ > (DD)^+$	7	0.006	accepted
$(LL)^- > (DD)^-$	7	0.5	rejected
$(LL)^0 > (LL)^+$	7	0.2	rejected
$(LL)^- > (LL)^0$	7	0.5	rejected
$(LL)^- > (LL)^+$	7	0.3	rejected

Bibliography

1. Vacanti J. P.; Langer, R. *The Lancet* **1999**, *354*, 32–34.
2. Kim, B. S.; Mooney, D. J. *Trends Biotechnol*. **1998**, *16*, 224–230.
3. Yoshimoto, H.; Shin, Y. M.; Terai, H.; Vacanti, J. P. *Biomaterials* **2003**, *24*, 2077–2082.
4. Heath, C. A. *Trends Biotechnol.* **2000**, *18*, 17-19.
5. Gunatillake, P.; Mayadunne, R.; Adhikari, R. *Biotechnol. Annu. Rev*. **2006**, *12*, 301-347.
6. Boontheekul, T.; Mooney, D. J. *Curr. Opin. Biotechnol*. **2003**, *14*, 559–565.
7. Stevens, M. M.; Qanadilo, H. F.; Langer, R.; Shastri, V. P. *Biomaterials* **2004**, *25*, 887–894.
8. George, M.; Abraham, T. E. *J. Control. Release* **2006**, *114*, 1–14.
9. Drury, J. L.; Dennis, R. G.; Mooney, D. J. *Biomaterials* **2004**, *25*, 3187–3199.
10. Brown, R. M. *J. Polym. Sci. A, Polym. Chem.* **2004**, *42*, 487–495.
11. Nishinari, K.; Takahashi, R. *Curr. Opin. Colloid Interface Sci.* **2003**, *8*, 396–400.
12. Saxena, I. M.; Brown, R. M. *Ann. Bot.* **2005**, *96*, 9–21.
13. Brown, R. M.; Saxena, I. M.; Kudlicka, K. *Trends Plant Sci.* **1996**, *1*, 149–156.
14. Kadajji, V. G.; Betageri, G. V. Water soluble polymers for pharmaceutical applications. *Polymers* **2011**, *3*, 1972-2009.
15. Clasen, C.; Kulicke, W.M. *Prog. Polym. Sci*. **2001**, *26*, 1839-1919.
16. Zhang, H.; Neau, S. H. *Biomaterials* **2001**, *22*, 1653-1658.
17. Malafaya, P. B.; Silva, G. A.; Reis, R. L. *Adv. Drug Deliv. Rev.* **2007**, *59*, 207-233.
18. Wang, J. Y.; Roehrl, M. H. *Proc. Natl. Acad. Sci. USA* **2002**, *99*, 14362-14367.
19. Pieper, J. S.; Oosterhof, A.; Dijkstra, P. J.; Veerkamp, J. H.; van Kuppevelt, T. H. *Biomaterials* **1999**, *20*, 847–858.
20. Lee, C. T.; Kung, P. H.; Lee, Y. D. *Carbohydr. Polym.* **2005**, *61*, 348–354.
21. Lippiello, L. *Osteoarthr. Cartil.* **2003**, *11*, 335–342.
22. Berg, J. M.; Tymoczko, J. L.; Stryer, L. Glycogen Metabolism. In *Biochemistry,* 7th ed.; W. H. Freeman and Company: New York, 2012; p 338.
23. Hers, H. G.; Hue, L. *Annu. Rev. Biochem.* **1983**, *52*, 617.
24. Kopecek, J.; Yang, J. *Acta Biomater*. **2009**, *5*, 805-816.
25. Semino, C. E. *J. Dent. Res*. **2008**, *87*, 606-616.
26. Yamada, Y.; Hozumi, K.; Aso, A.; Hotta, A.; Toma, K.; Katagiri, F.; Kikkawa, Y.; Nomizu, M. *Biomaterials*. **2012**, *33*, 4118-4125.
27. Yamada, Y.; Hozumi, K.; Katagiri, F.; Kikkawa, Y.; Nomizu, M. *Biopolymers.* **2010**, *94*, 711-720.
28. Chinen, N.; Tanihara, M.; Nakagawa, M.; Shinozaki, K.; Yamamoto, E.; Mizushima, Y.; Suzuki, Y. *J Biomed Mater Res A* **2003**, *67*, 61–68.
29. Fujita, M.; Ishihara, M.; Simizu, M.; Obara, K.; Ishizuka, T.; Saito, Y.; Yura, H.; Morimoto, Y.; Takase, B.; Matsui, T.; Kikuchi, M.; Maehara, T. *Biomaterials* **2004**, *25*, 699–706.

30. Nakamura, S.; Ishihara, M.; Obara, K.; Masuoka, K.; Ishizuka, T.; Kanatani, Y.; Takase, B.; Matsui, T.; Hattori, H.; Sato, T.; Kariya, Y.; Maehara, T. *J Biomed Mater Res A* **2006**, *78*, 364–371.
31. Sakiyama-Elbert, S. E.; Hubbell, J. A. *J Control Release* **2000**, *65*, 389–402.
32. Tanihara, M.; Suzuki, Y.; Yamamoto, E.; Noguchi, A.; Mizushima, Y. *J Biomed Mater Res* **2001**, *56*, 216–221.
33. Svergun, D.; Koch, M. H. J. *Rep. Prog. Phys.* **2003**, *66*, 1735-1782.
34. Gamani, A.; Paoletti, S.; Toffanin, R.; Micali, F.; Michielin, L.; Bevilacqua, C. *Biomaterials* **2002**, *23*, 1161-1167.
35. Stokke, B.; Draget, K.; Smidsrod, O.; Yuguchi, Y.; Urakawa, H.; Kajiwara, K. *Macromolecules* **2000**, *33*, 1853-1863.
36. Shinohara, Y.; Kayashima, K.; Okumura, Y.; Zhao, C.; Ito, K.; Amemiya, Y. *Macromolecules* **2006**, *39*, 7386-7391.
37. Tada, T.; Matsumoto, T.; Masuda, T. *Carb. Pol.* **1999**, *39*, 53-59.
38. Hiller, J. C.; Thompson, T. J. U.; Evison, M. P.; Chamberlain, A. T.; Wess, T. J. *Biomaterials* **2003**, *24*, 5091-5097.
39. Markarian, M.; Hariri, H.; Reisch, A.; Urban, V.; Schlenoff, J. *Macromolecules* **2012**, *45*, 1016-1024.
40. Wilson, K.; Allen, A.; Washburn, N.; Antonucci, J. *J. Biomed. Mat. Res.* **2007**, *81A*, 113-123.
41. Luk, A.; Murthy, N.; Wang, W.; Rojas, R.; Kohn, J. *Acta Biomat.* **2012**, *8*, 1459-1468.
42. Feuz, L.; Stunz, P.; Geue, T.; Textor, M.; Borisov, O. *Eur. Phys. J.* **2007**, *23*, 237-245.
43. Weigandt, K. M.; Porcar, L.; Pozzo, D.C. *Soft Matter* **2011**, *7*, 9992-10000.
44. Barron, L. D. *Space Sci. Rev.* **2008**, *135*, 187-201.
45. Luo, Z.; Zhao, X; Zhang, S. *PloS ONE* **2008**, *8*, e2364.
46. Luo, Z.; Zhao, X; Zhang, S. *Macromol. Biosci.* **2008**, *8*, 785-791.
47. Nagy, K. J.; Giano, M. C.; Jin, A.; Pochan, D. J.; Schneider, J. P. *J. Am. Chem. Soc.* **2011**, *133*, 14975-14977.
48. Dzwolak, W.; Ravindra, R.; Nicolini, C.; Jansen, R.; Winter, R. *J. Am. Chem. Soc.* **2004**, *126*, 3762-3768.
49. Taraban, M.; Feng, Y.; Hammouda, B.; Hyland, L. L.; Yu, Y. B. *Chem. Mater.* **2012**, *24*, 2299-310.
50. Yi, Q.; Wena, X.; Li, L.; He, B.; Nie, Y.; Wu, Y.; Zhang, Z.; Gu, Z. *Eur. Poly. J.* **2009**, *45*, 1970-1978.
51. Sun, T.; Han, D.; Rhemann, K.; Chi, L. and Fuchs, H. *J. Am. Chem. Soc.* **2007**, *129*, 1496-1497.
52. Baruch, L.; Machluf, M. *Biopolymers* **2006**, *82*, 570-579.
53. Suh, J. K.; Matthew, H. W. *Biomaterials* **2000**, *21*, 2589-2598.
54. Howling, G. I.; Dettmar, P. W.; Goddard, P. A.; Hampson, F. C.; Dornish, M.; Wood, E. J. *Biomaterials* **2001**, *22*, 2959-2966.
55. Freier, T.; Koh, H. S.; Kazazian, K.; Shoichet, M. S. *Biomaterials* **2005**, *26*, 5872-5878.
56. Hu, Q.; Li, B.; Wang, M.; Shen, J. *Biomaterials* **2004**, *25*, 779-785.

57. Shanmugasundaram, N.; Ravichandran, P.; Reddy, P. N.; Ramamurty, N.; Pal, S.; Rao, K. P. *Biomaterials* **2001**, *22*, 1943-1951.
58. Park, D. J.; Choi, B. H.; Zhu, S. J.; Huh, J. Y.; Kim, B. Y.; Lee, S. H. *J. Cranio-Maxfac. Surg.* **2005**, *33*, 50-54.
59. Wang, L.; Shelton, R. M.; Cooper, P. R.; Lawson, M.; Triffitt, J. T.; Barralet, J. E. *Biomaterials* **2003**, *24*, 3475-3481.
60. Vacanti, C. A.; Langer, R.; Schloo, B.; Vacanti, J. P. *Plast. Reconstr. Surg.* **1991**, *88*, 753-758.
61. Rees, D. A. *Pure Appl. Chem.* **1981**, *53*, 1–14.
62. Li, Z.; Ramay, H.; Hauch, K. D.; Xiao, D.; Zhang, M. *Biomaterials* **2005**, *26*, 3919-3928.
63. Chung, T. W.; Yang, J.; Akaike, T.; Cho, K. Y.; Nah, J. W.; Kim, S. I.; Cho, C. S. *Biomaterials* **2002**, *23*, 2827-2834.
64. Lai, H. L.; Abu'Khalil, A.; Craig D. Q. M. *Int. J. Pharm.* **2003**, *251*, 175-181.
65. Sirko, S.; von Holst, A.; Wizenmann, A.; Gotz, M.; Fraissner, A. *Development* **2007**, *134*, 2727-2738.
66. Pieper, J.S.; Oosterhof, A.; Dijkstra, P. J.; Veerkamp, J. H.; van Kuppelvelt, T. H. *Biomaterials* **1999**, *20*, 847-858.
67. Park, Y. J.; Lee, Y. M.; Lee, J. Y.; Seol, Y. J.; Chung, C. P.; Lee, S. J. *J. Contr. Release* **2000**, *67*, 385-394.
68. Mikos, A. G.; Sarakinos, G.; Lyman, M. D.; Ingber, D. E.; Vacanti, J. P.; Langer, R. *Biotech. Bioeng.* **1993**, *42*, 716-723.
69. Mooney, D. J.; Kaufmann, P. M.; Sano, K.; Mcnamara, K. M.; Vacanti J. P.; Langer, R. *Transplant Proc.* **1994**, *26*, 3425-3426.
70. Mooney, D. J.; Park, S.; Kaufmann, P. M.; Sano, K.; Mcnamara, K.; Vacanti, J. P.; Langer, R. *J. Biomed. Mater. Res.* **1995**, *29*, 959-966.
71. Zhang, Y.; Zhang, M. *J. Biomed. Mater. Res.* **2001**, *55*, 304-312.
72. Berger, J.; Reist, M.; Mayer, J.; Felt, O.; Peppas, N.; Gurny, R. *J. Pharm. Biopharm.* **2004**, *57*, 19-34.
73. Abramoff, M. D.; Magelhaes, P. J.; Ram, S. *J. Biophotonics Int.* **2004**, *11*, 36-42.
74. Glinka, C. J.; Barker, J. G.; Hammouda, B.; Krueger, S.; Moyer, J. J.; Orts, W. J. *J. Appl. Crystallogr.* **1998**, *31*, 430-445.
75. Kline, S. R. *J. Appl. Chrystallogr.* **2006**, *39*, 895-900.
76. Whitten, A.; Trewhella, J. Small-Angle Scattering and Neutron Contrast Variation. In Micro and Nano Technologies in Bioanalysis; Humana, 2009, 307-322.
77. Ilavsky, J.; Jemian, P. *J. Appl. Crystallogr.* **2009**, *42*, 347–353.
78. Debye, P.; Bueche, A. M. *J. Appl. Phys.* **1949**, *20*, 518–525.
79. Soni, V. K.; Stein, R. S. *Macromolecules* **1990**, *23*, 5257–5265.
80. de Gennes, P. G. Scaling Concepts in Polymer Physics; Cornell University Press, 1979.
81. Glatter, O.; Kratky, O. (eds.) Small Angle X-Ray Scattering; Academic Press: London, 1982.
82. Svergun, D. I. *J. Appl. Crystallogr.* **1992**, *25*, 495-503.
83. Kuo, C. K.; Ma, P. X. *J. Biomed. Mater. Res.* **2007**, *84A*, 899-907.

84. Ho, M. H.; Kuo, P. Y.; Hsieh, H. J.; Hsien, T. Y.; Hou, L. T.; Lai, J. Y.; Wang, D. M. *Biomaterials* **2004**, *25*, 129-138.
85. Jayawarna, V.; Richardson, S. M.; Hirst, A. R.; Hodson, N. W.; Saiani, A.; Gough, J. E.; Ulijn, R. V. *Acta Biomat.* **2009**, *5*, 934-943.
86. Jung, J. P.; Gasiorowski, J. Z.; Collier, J. H. *Peptide Science* **2010**, *94*, 49-59.
87. Branco, M. C.; Pochan, D. J.; Wagner, N. J.; Schneider, J. P. *Biomaterials* **200**9, *30*, 1339-1347.
88. Silva, G. A.; Czeisler, C.; Niece, K. L.; Beniash, E.; Harrington, D. A.; Kessler, J. A.; Stupp, S. I. *Science* **2004**, *303*, 1352-1355.
89. Kisiday, J. D.; Kopesky, P. W.; Evans, C. H.; Grodzinsky, A. J.; McIlwraith, C. W.; Frisbie, D. D. *J. Orthopaedic Res.* **2008**, *26*, 322-331.
90. Bakota, E. L.; Aulisa, L.; Galler, K. M.; Hartgerink, J. D. *Biomacromolecules* **2011**, *12*, 82-87.
91. Taraban, M. B.; Ramachandran, S.; Gryczynski, I.; Gryczynski, Z.; Trewhella, J.; Yu, Y. B. *Soft Matter* **2011**, *7*, 2624–2631.
92. Dong, H.; Paramonov, S. E.; Aulisa, L.; Bakota, E. L.; Hartgerink, J. D. *J. Am. Chem. Soc.* **2007**, *129*, 12468-12472.
93. Aulisa, L.; Dong, H.; Hartgerink, J. D. Biomacromolecules 2009, 10, 2694-2698.
94. Hosseinkhani, H.; Hosseinkhani, M.; Tian, F.; Kobayashi, H.; Tabata, Y. *Tissue Eng.* **2007**, *13*, 11-19.
95. Hyland, L. L.; Taraban, M. B.; Hammouda, B.; Yu, Y. B. *Biopolymers* **2011**, *95*, 840-851.
96. Zhang, S.; Holmes, T.; Lockshin, C.; Rich, A. *Proc. Natl. Acad. Sci. U. S. A.* **1993**, *90*, 3334-3338.
97. Ramachandran, S.; Tseng, Y.; Yu, Y. B. *Biomacromolecules* **2005**, *6*, 1316-1321.
98. Ramachandran, S.; Flynn, P. F.; Tseng, Y.; Yu, Y. B. *Chem. Mater.* **2005**, *17*, 6583-6588.
99. Ramachandran, S.; Trewhella, J.; Tseng, Y.; Yu, Y. B. *Chem. Mater.* **2006**, *18*, 6157-6162.
100. Chan, W. C.; White, P. D. Fmoc Solid Phase Peptide Synthesis: A Practical Approach; Oxford University Press: New York, 2000; pp. 1–75.
101. Gill, S. C.; von Hippel, P. H. *Anal. Biochem.* **1989**, *182*, 319–326.
102. Svergun, D. I. *Biophys. J.* **1999**, *76*, 2879-2886.
103. Whitten, A. E.; Jeffries, C. M.; Harris, S. P.; Trewhella, *J. Proc. Natl. Acad. Sci. U.S.A.* **2008**, *105*, 18360-18365.
104. Ingham, B.; Li, H.; Allen, E. L.; Toney, M. F. *J. Appl. Cryst.* **2011**, *44*, 221–224.
105. Bysrický, S.; Malovíková, A.; Sticzay, T. *Carbohydr. Polym.* **1991**, *15*, 299-308.
106. Paradossi, G.; Chiessi, E.; Malovíková, A. *Biopolymers* **1999**, *50*, 201-209.
107. Nilsson, K. P. R.; Olsson, J. D. M.; Stabo-Eeg, F.; Lindgren, M.; Konradsson, P.; Inganas, O. *Macromolecules* **2005**, *38*, 6813-6821.
108. Gerber, D.; Shai, Y. *J. Mol. Biol.* **2002**, *322*, 491-495.
109. Patching, S. G.; Henderson, P. J.; Herbert, R. B.; Middleton, D. A. *J. Am. Chem. Soc.* **2008**, *130*, 1236-44.

110. Mason, P. E.; Lerbret, A.; Saboungi, M. L.; Neilson, G. W.; Dempsey, C. E.; Brady, J. W. *Proteins* **2011**, *79*, 2224-32.
111. Vazquez-Ibar, J. L.; Guan, L.; Svrakic, M.; Kaback, H. R. *PNAS* **2003**, *100*, 12706-11.
112. Loftsson, T.; Brewster, M. E. *J. Pharm. Sci.* **1996**, *85*, 1017-25.
113. Hyland, L. L.; Taraban, M. B.; Feng, Y.; Hammouda, B.; Yu, Y. B. *Biopolymers* **2012**, *97*, 177-188.
114. Chen, W.-R.; Butler, P. D.; J. Magid, L. J. Langmuir **2006**, 22, 6539-6548.
115. Kumar, A.; Ramakrishnan, V.; Ranbhor, R.; Patel, K.; Durani, S. *J. Phys. Chem. B* **2009**, *113*, 16435−16442.
116. Saghatelian, A.; Yokobayashi, Y.; Soltani, K.; Ghadiri, M. R. *Nature* **2001**, *409*, 797−801.
117. Milton, R. C.; deL.; Milton, S. C. F.; Kent, S. B. H. *Science* **1992**, *256*, 1445−1448.
118. Reich, Z.; Schramm, O.; Brumfeld, V.; Minsky, A. *J. Am. Chem. Soc.* **1996**, *118*, 6345−6349.
119. Gospodarowicz, D.; Delgado, D.; Vlodavsky, I. *Proc. Nat Acad. Sci. USA* **1980**, *77*, 4094-4098.
120. Reilly, G. C.; Engler, A. J. *J. Biomech.* **2010**, *43*, 55-62.
121. Bet, M. R.; Goissis, G.; Vargas, S.; Selistre-de-Araujo, H. S. *Biomaterials* **2003**, *24*, 131-37.
122. Dadsetan, M.; Pumberger, M.; Casper, M. E.; Shogren, K.; Giuliani, M.; Ruesink, T.; Hefferan, T. E.; Currier, B. L.; Yaszemski, M. J. *Acta Biomaterialia* **2011**, *7*, 2080-90.
123. Kim, S.; English, A. E.; Kihm, K. D. *Acta Biomaterialia* **2009**, *5*, 144-51.
124. Ishikawa, J.; Tsuji, H.; Sato, H.; Gotoh, Y. *Surf. Coat. Technol.* **2007**, *201*, 8083-90.
125. Lee, J. H.; Jung, H. W.; Kang, I. K.; Lee, H. B. *Biomaterials* **1994**, *15*, 705-711.
126. Keselowsky, B. G.; Collard, D. M.; García, A. J. *J. Biomed. Mat. Res. A*, **2003**, *66*, 247-59.
127. Keselowsky, B. G.; Collard, D. M.; García, A. J. *Proc. Natl. Acad. Sci.* **2005**, *102*, 5953-57.
128. Yi, Q.; Wena, X.; Li, L.; He, B.; Nie, Y.; Wu, Y.; Zhang, Z.; Gu, Z. *Eur. Poly. J.* **2009**, *45*, 1970-78.
129. Sun, T.; Han, D.; Rhemann, K.; Chi, L. and Fuchs, H. *J. Am. Chem. Soc.* **2007**, *129*, 1496-97.
130. Pittenger, M. F.; Martin, B. *J. Circ. Res.* **2004**, *95*, 9-20.
131. McIntosh, K. R.; Bartholomew, A. *Graft* **2000**, *3*, 324.
132. Berridge, M. V.; Tan, A. S.; McCoy, K. D.; Wang, R. *Biochemica*. **1996**, *4*, 15–20.
133. Feng, Y.; Taraban, M.; Yu, Y. B. *Soft Matter* **2011**, *7*, 9890-93.